

Study on the Measurement of High-Speed Impulsive Force Using Piezoelectric Film

(圧電フィルムを用いた高速衝撃力の計測に関する研究)

BY

Chen Liu

Department of Transportation and Environmental Systems
Graduate School of Engineering
Hiroshima University

March 2016

Contents

CHAPTER 1 INTRODUCTION	5
1.1. Research Background	5
1.2. Content Overview	8
CHAPTER 2 PROPERTIES OF POLYMER PIEZOELECTRIC MATERIAL	13
2.1 The General Nature of the Piezoelectric Material.....	14
2.2 The Properties of the PVDF	15
2.3 Output Voltage Due to the Piezoelectric Effect.....	17
2.4 Measurement Principle of Piezoelectric Sensor	20
CHAPTER 3 THREE TYPES OF PIEZOELECTRIC SENSOR DEVELOPED AS LOAD SENSING ELEMENT	23
3.1 Basic Structure of Three Types of Piezoelectric Sensor	24
3.1.1 Sheet-Type Sensor	24
3.1.2 Pad Sensor	27
3.1.3 Fluctuating Load Detection Plate.....	30
3.2 Some Application Examples Using Piezoelectric Sensor Developed in This Study	34
3.2.1 The Falling Experiment of the Lead Ball and Steel Ball.....	34
3.2.2 Drop Test of Longitudinally Turning Bar and Used Sensors	43
3.3 Conclusions	50
CHAPTER 4 APPLICATIONS OF PAD SENSOR INSTALLED ONTO THE BASEBALL BAT	52
4.1 Experiments Conditions and the Design of the Experiment Devices.....	53
4.2 Installation of the Sensor to the Surface of the Pipe	54
4.3 Baseball Falling test on the Column Sensor	55
4.4 Hitting Experiment of Baseball Bat with Pad Sensor	58

4.5	Conclusions	60
CHAPTER 5	FLEXIBLE SENSOR FOR THE IMPACT FORCE MEASUREMENT IN FLEXIBLE INTERFACE	62
5.1	Measurement of Force on Soft Material Surface by Using a Sheet-Type Sensor	63
5.1.1	Spherical Surface Pressing on the Flexible Material Surface.....	63
5.1.2	Fist Pressing, Palm Pressing and Fist Punching on the Surface of Flexible Material	66
5.2	Mechanical Issues in Impact Force Measurement on Flexible Material Surface	68
5.2.1	Influence of Out-of-Plane Bending Deformation of the Sensor Element.....	68
5.2.2	Influence of Rubbing Force on the Sensor Surface (Shear Force Caused by Rubbing)	69
5.2.3	Influence of Contact Friction on the Sensor Surface (Shear Force Caused by the Poisson's Effect).....	70
5.2.4	Influence of Lateral Compression Caused by the Overhanging Deformation of Flexible Material	71
5.3	Flexible Sensor Made from Plural Sensor Elements Arranged in a Matrix.....	73
5.3.1	Prototype of sensor element.....	73
5.3.2	Prototype of flexible impact force sensor.....	75
5.4	Experiment.....	78
5.4.1	Comparison of Sensor Output and Load Cell Output	78
5.4.2	Punching Test of the Sensor Installed on Concrete Wall.....	81
5.4.3	Punching Test of the Sensor Installed on Sandbag.....	82
5.5	Improvement of the Sensor Flexibility	83
5.6	Conclusions	85
CHAPTER 6	THORN SHAPE AND DOUBLE-STRIKE PHENOMENON SEEN IN THE IMPACT FORCE WAVEFORM OF SOFT MATERIALS.....	87
6.1	Thorn Shape and Double-Strike Phenomenon Seen in the Impact Force Waveform of Soft Materials	88
6.2	Condition of Flat Frontal Impact and Compact Drop Test Equipment	90

6.3	Experimental results	92
6.3.1	Impact Force of Agar Jelly under Flat Frontal Impact (<i>Type I</i> waveform)	92
6.3.2	Impact Force of Konjac under Flat Frontal Impact (<i>Type III</i> Waveform)	93
6.3.3	Impact Force of Gel Sheet under Flat Frontal Impact (<i>Type II</i> waveform)	94
6.3.4	Impact Force of Nitrile Rubber (NBR) Plate under Flat Frontal Impact (<i>Type II</i> waveform)	95
6.3.5	Impact Force of Oil Clay Plate under Flat Frontal Impact (<i>Type II</i> waveform)	95
6.3.6	Impact Force of Low-Rebound Urethane Foam under Flat Frontal Impact (<i>Type II</i> waveform)	96
6.3.7	Impact Force of Ham and Edible Meat under Flat Frontal Impact (<i>Type II</i> waveform)	96
6.4	Measurement of Triple-Strike Waveform	97
6.5	Mechanism of Thorn-Shape Waveform and Double-Strike Phenomenon	99
6.5.1	Contact Time of Thorn-Shape Waveform	99
6.5.2	Thickness Effect of Soft Material	100
6.5.3	Mechanism of Thorn-Shape Waveform	100
6.6	Conclusions	103

CHAPTER 7 VISCOSITY TRANSIENT PHENOMENON DURING DROP IMPACT TESTING AND ITS SIMPLE DYNAMICS MODEL 105

7.1	Impact Force Waveform of Soft Materials under Flat Frontal Impact	106
7.2	Simulation of Impact Force Waveform by the SLS Model	107
7.3	Comparison of Experimental and Simulation Results	108
7.3.1	Influence of Impact Velocity on the Thorn-Shaped Waveform	108
7.3.2	Influence of Impact Area on the Thorn-Shaped Waveform	110
7.3.3	Case of An Oil Clay Plate under A Flat Frontal Impact	113
7.4	Discussion	114

7.5 Impact Force of Human Skin under a Flat Frontal Impact	116
7.6 Impact Force of Free-Falling Hollow Balls	117
7.7 Conclusions	118
CHAPTER 8 CONCLUSIONS AND FUTURE SCOPES	120
8.1 Conclusions	120
8.2 Future scopes	124
ACKNOWLEDGMENTS	125

Chapter 1 Introduction

1.1. Research Background

In a series of practical problems of various fields of engineering science and technology, even in our daily life, people will encounter a variety of impact loading problems. And it can be observed that mechanical response of objects under impact loads and static loads often have significantly difference [1]. Understanding the mechanical response of an object under impact loading conditions will greatly contribute to the project application and engineering design of these materials.

The main purpose of the new designs and evaluations of a physical/mechanical sensor for the measurement of dynamic load is focused to be smaller, more versatile and more accurate. From now on, developments of tactile sensors have been considered with consideration of miniaturization and high sensitivity [2-4]. The driving force toward smaller, cheaper component and more flexible sensor is one of the major trends in sensor development. At the same time, flexibility in its dimension generates new applications in the sensor market. Therefore many sensor designers and sensor companies have spent their energy to achieve those goals.

Nowadays, measurements of physical force in various aspects from fluid pressure, weight, acceleration, displacement, torque etc, can be carried out by many ways with varied types of sensors. The sensors are manufactured on many different operating principles; resistive, inductive, capacitive, piezoelectric, etc, [5].

In the field of the sensors to measure dynamic loads, several sensors using strain gage

as the sensing element have been developed. The force plate using strain gage was developed to measure the vertical and horizontal ground reaction forces of the athlete in long jump experiment [6]. The same impact force sensor (a force platform) was used to measure the impact force of the jumping experiment [7]. Piezoelectric material has been used for the same purposes in similar way as conventional strain gauges, as long as the signal is dynamic.

The output stability and output proportionality of the sensor using PVDF film as the sensing element with respect to the measured dynamic load is the special attention in sensor design. To achieve such conditions, some composition of the PVDF sensor design has been conducted. The pressure sensor using PVDF film which sandwiched between two LTCC (low temperature cofired ceramic) has been introduced [8]. The PVDF sensor for the measurement of impact force also has been introduced by Sensor Product Division of Measurement Specialist [9]. In this design a piezo film sensor was attached to the underside of a thin fabric sheet (cleaning cloth).

Piezoelectricity, Greek for “pressure” electricity, was discovered by the Curie brothers more than 100 years ago. They found that quartz changed its dimension when subjected to an electrical field, and conversely, generated electrical charge when mechanically deformed. One of the first practical applications of the piezoelectric technology was made in the 1920’s by Frenchman, Langevin who developed a quartz transmitter and receiver for underwater sound. Before World War II, researchers discovered that certain ceramic materials could be made piezoelectric when subjected to a high polarizing voltage, a process analogous to magnetizing a ferrous material. By 1960’s, researcher has discovered a weak piezoelectric effect in whale bone and tendon. In 1969, Kawai found very high piezo-activity in the polarized fluoropolymer, Polyvinylidene fluoride (PVDF). While other materials, like nylon and PVC exhibit the effect, none are as highly piezoelectric as PVDF and its copolymers [10].

In our laboratory, in recent years the researches of piezoelectric materials are proceeding constantly. Previous studies of Gang Liu is “Stress and Stress Intensity Factor Measurement of Structures Using Piezoelectric Material”. The aim of this research is to develop some new experimental techniques for stress measurement of a structural member as well as stress intensity factor (SIF) measurement of a two-dimensional crack in a real structure using piezoelectric material. Structural health monitoring has been accepted as an important and justified effort for safety assessment of structures. The structural response to the loading obtained from the monitoring may lead to modification or strengthening of existing structures, or other modification of future design and construction. Engineering structures may contain crack-like flaws, or they may develop cracks during their service life. The existence of such cracks and their subsequent growth can cause a loss of strength and a reduction in the service life of a structure. The SIF evaluation is one of important ways for damage detection in real structures [11].

And the previous studies of Taufiq Arif Setyanto is “Development of Dynamic Load Sensor and Large Deformation Sensor by the Use of Piezoelectric Film”. His studies aid to design and evaluate a new sensor for dynamic loads measurement by using piezoelectric material. A new kind of elastic band sensor for large deformation measurement and shoes insole sensor are proposed in his dissertation. The purpose of the elastic band sensor is to achieve the deformation measurement more than $\pm 50\%$. The elastic band sensor basically composed of a strain sensing element, an elastic rubber band, a protecting member and fixing members. A PVDF film is set up at the middle part of the rubber band and used for the strain sensing element of the rubber band. The shoes insole sensor is thin and flexible, and it can be used as an insole of the shoes. Dynamic pressure load working at the foot sole can be measured at the designed points [12].

However, in previous studies, the dynamic is not discussing in the impact occasions. Through increasing the impact extent and speed, the dynamic response is different. In the

field of impulsive force measurement, load cell is the most widely used tool, however, load cell is limited to the test environment and affected by vibration deeply [13]. Furthermore, strain gauge load cells require continuous electric energy for the production and display of signals. Subsequently on the high-speed occasion, the high-speed impulsive force waveform whose shock time from contact to separation is below 1 millisecond usually will produce residual vibration because of the overlap and resonance of subtle shock waves. Therefore, it is required to develop a portable light and high-precise impulsive force detection plate.

1.2. Content Overview

This study is conducted to develop a thin sensor which is capable of measuring a high-speed impact using a polymeric piezoelectric material. Firstly, the three kinds of prototype sensor which are sheet-type impact force sensor, pad-type sensor and fluctuating load detection plate are developed, and these three types sensor have been experimentally revealed that exhibit excellent response characteristics for high-speed impact load. In addition, their applicability already is clarified through measuring the striking force of the baseball bat and the sand bag hit test of boxing. Subsequently, a falling impact force measuring device has been developed, on which impact force sensor are installed on both the load side and the receiving side. By using this device, the impulsive force waveforms of some kinds of soft materials are measured. It is shown that the most of soft material show the thorn-shape waveforms resulting from the strain rate dependence occurring in the initial stage of impact force. Furthermore, by performing an impact simulation using the dynamic model, it is revealed that the occurrence reason of the thorn-shape waveform is caused by the viscosity transient phenomenon.

Chapter 1 presents the background of this research, and the outline of other chapters.

In chapter 2, it shows the properties of polymer piezoelectric material and the principle of measuring impact force using a polymer piezoelectric material.

In chapter 3, three kinds of prototype sensors which are sheet-type impact force sensor, pad-type sensor and fluctuating load detection plate are developed. And the performance of these three types has been clarified in a variety of impact tests. Sheet-type sensor has a structure in which silicone rubber sheets are pasted on both surfaces of the piezoelectric film. By strain amplification effect of silicon rubber, even small impact force is still possible to accurately measure. The pad sensor consists of a piezoelectric film sandwiched between two pieces of metal sheet, and the whole body is laminated by the resin film. The pad sensor features light-weighting and high-rigidity in thickness direction, therefore, it is verified that the thin pad sensor can be used to measure the greater extent high-speed impact compared to the conventional load cell. The fluctuating load detection plate owns the structure that two metal plates grip a pad sensor and tightened with bolts. Since the fluctuating load detection plate possesses the metal plates, it can only be used in the plane, but it still can accept impact from hard object. The accuracy of these sensors are demonstrated based on the measurements of the waveform impulse and the momentum theory.

In chapter 4, as an example of application to high-speed impact force of the pad sensor, a sensor that can be used in wrapped on a cylindrical curved surface is developed. The sensor is placed on the baseball bat, aiming the impact force of hitting. Firstly, a friction removal mechanism in contact interface, a bendable sensor configuration and a method of sensor installation on the surface of the pipe are discussed. Then, prototype sensors that can be installed on a pipe with diameter of about 70mm are made. The performance of sensor is investigated by the pipe punch test and the ball drop test. Then,

the impulsive force is measured by the test that a batter hits the ball which the pitcher threw. A metal bat and a hard ball are used for the experiment of hit and bunt.

In chapter 5, targeting an impact force sensor that can be used in a flexible surface, a flexible impulsive force sensor has been developed in which multiple miniature sheet-type impact force sensor are formed by matrix arrangement. Firstly, several mechanical phenomena, which are the cause of the error signal of the sensor, are discussed. These are the influences of out-of-plane bending deformation, shear force caused by rubbing, shear force caused by the Poisson's effect of contact material, and the lateral compressive force caused by the overhanging deformation of flexible material. Then, a prototype sensor that can eliminate the error factors of these is developed. The sensor is a distribution type impact sensor in which sixteen sensor elements are arranged in a 4×4 matrix. Punching experiments using a boxing glove are carried out by installing the sensor on the load cell, on the concrete wall and on the sandbag. From the experiment, it is found that the impact force can be measured with good accuracy by using the sensor.

In chapter 6, at first, we assembled a prototype falling type impact load device using a pad sensor and fluctuating load detection plate as detection units. Synchronized impact forces are measured using two sensors installed on both the drop hammer side and the floor side. Subsequently, using this device, the falling impact onto some soft materials which includes agar, rubber, gels, clay, sponge rubber and meat are measured. A flat frontal impact is the condition where a drop hammer with a flat bottom surface strikes a plate-like soft material in the normal direction. Then, under the condition of flat frontal impact, it is verified that a thorn-shape waveform occurs in the initial stage of impact with most of the soft materials

In chapter 7, in order to elucidate the physical reason of the thorn-shape waveform, using a dynamic model (standard linear solid model) that takes into account the viscosity

transient phenomenon, simulation of the impact force waveform is performed. The viscosity transient can be stated that, the moment when the impact force is loaded, in the vicinity of the apex of the thorn, the viscosity resistance of soft material is rapidly decreased and the material becomes soften. Although physical reason for viscosity transient phenomenon occurrence have not been elucidated yet, by assuming a viscous resistance transition occurs, the overall impact waveform containing the thorn is shown to be able to simulate to a value close to the experimental value.

Chapter 8 describes the conclusions of the research and recommendations for future work.

References

- [1] Goldsmith, W. (2001) *Impact the Theory and Physical Behaviour of Colliding Solids*.
- [2] E.S. Hwang, J.H. Seo, Y.J. Kim, (2007) A polymer-based Flexible Tactile Sensor for Both Normal and Shear Load Detections and Its Application for Robotics, *J. Microelectromech. Syst.* 16, 556–563.
- [3] D.J. Beebe, D.D. Denton, R.G. Radwin, J.G. Wenster, (1998) A Silicon-based Tactile sensor for Finger-Mounted Applications, *IEEE Trans. Biomed. Eng.* 45, 151–159.
- [4] Y.M. Huang, N.C. Tsai, J.Y. Lai, (2010) Development of Tactile Sensors for Simultaneous Detection of Normal and Shear Stresses, *Sens. Actuators A* 159 189–195.
- [5] *Strain Gage Based Transducers: Their Design and Construction*, Vishay, Measurement Group, Inc, 1988.
- [6] Seyfarth, A., Friedrich, A., Wank, V. and Blickan, R. (1999) Dynamics of the Long Jump, *Journal of Biomechanics* 32, 1259-1267.
- [7] Ashby, B.M. and Heegaard, J.H. (2002) Role of Arm Motion in Standing Long Jump, *Journal of Biomechanics* 35, 1631-1637.
- [8] Khanna, P.K., Hornbostel, B., Grimme, R., Schafer, W. and Dorner J. (2004) Miniature Pressure Sensor and Micromachined Actuator Structure Based on Low-Temperature-Cofired Ceramics and Piezoelectric Material, *Materials Chemistry and Physics* 87, 173-178.
- [9] Sensor Product Division (Europe) RB 03/00. Measurement Specialist. Available from the internet at www.msiousa.com.
- [10] Kawai, H. (1969) The Piezoelectricity of Poly (vinylidene Fluoride), *J. Appl. Phys.* 8, Japan, 975-976.
- [11] Liu, G. (2004) Study on Stress and Stress Intensity Factor Measurement of Structures Using Piezoelectric Material, Doctoral Dissertation, Hiroshima University.
- [12] Taufiq Arif Setyanto (2006) Design and Evaluation of Dynamic Loads Sensor Using Piezoelectric Material, Doctoral Dissertation, Hiroshima University.
- [13] Bourgeois, F.S. and Banini, G.A. (2002) A Portable Load Cell for In-situ Ore Impact Breakage Testing, *International Journal of Mineral Processing*, 65, 1, 31–54.

Chapter 2 Properties of Polymer Piezoelectric Material

Polyvinylidene fluoride (PVDF) is a synthetic semicrystalline polymer with piezoelectric properties. Since the discovery of piezoelectric effects in PVDF by Kawai [1], the properties of this material have been widely used in a variety of applications, particularly as sensors and transducers [2, 3]. Some experimental studies have also been performed focusing on various electro-mechanical properties of PVDF [4-6]. Recently, piezoelectric film (PVDF film) and conductive rubber are the focus of attention as the attractive sensor materials to measure loads, stresses, strains, or deformations. For example, ideas of using PVDF film to the vehicle weight measurement, measurements of human's heartbeat or animal's shivering, etc, are proposed [7, 8]. Authors applied the PVDF film to the stress and stress intensity factor measurements of metal structures [9, 10]. The conductive rubber can measure pressure based on the change of electric resistance caused by strain. The application of the conductive rubber has been often discussed in the field of tactile sensors [11-13].

The piezoelectric properties of PVDF are obtained by stretching and poling of extruded thin sheets of the polymer producing an alignment of molecular chain in the stretch direction. Polarization of PVDF is achieved by subjecting the polymer to an elevated, typically, 130°C temperature and electric field of up to 100 kV/mm.

In this work, thin PVDF films were utilized for the stress measurement of collision objects. PVDF film is a flexible, lightweight, tough engineering plastic available in a wide variety of thickness and large areas. It can be directly attached to a structure without disturbing its mechanical motion. Therefore, PVDF film is well suited to strain sensing

applications requiring very wide bandwidth and high sensitivity. Then we intend to improve the structure of the load sensor and improve the result of the output of the signal processing circuit by the use of PVDF polymer piezoelectric material. In this chapter, we will describe the basic properties of the polymer piezoelectric material.

2.1 The General Nature of the Piezoelectric Material

Since the discovery of piezoelectricity, many researchers have explored the existence of piezoelectric activity in other materials. The two common types of piezoelectric materials are lead zirconate titanate ceramics and PVDF (PolyVinylidene DiFluoride) polymers. Piezoelectric ceramics and piezoelectric polymers are usually produced in thin sheets with films of metal deposited on opposite surfaces to form electrodes. Piezoelectric ceramics are brittle and stiff, while piezoelectric polymers are tough and flexible.

The properties of piezoelectric material are commonly defined by the constitutive equation of linear piezoelectricity. The equations describe the interaction between the mechanical and electrical responses of the material in terms of stress, strain, electric flux density, electric field, and dielectric tensors. The functional relations between these characteristics are linear, implying, in particular, direct proportionality between mechanical loads and deflections, and no energy dissipation when the material is subjected to loading unloading cycles.

The direct piezoelectric effect is present when a mechanical deformation of the piezoelectric material produces a proportional change in the electric polarization of that material. The converse piezoelectric effect means that mechanical stress proportional to an acting external electric field is induced in the piezoelectric material. The coupled

mechanical and electrical properties of piezoelectric materials make them well suited for use as sensors (which use the direct piezoelectric effect) and actuators (which use the converse piezoelectric effect).

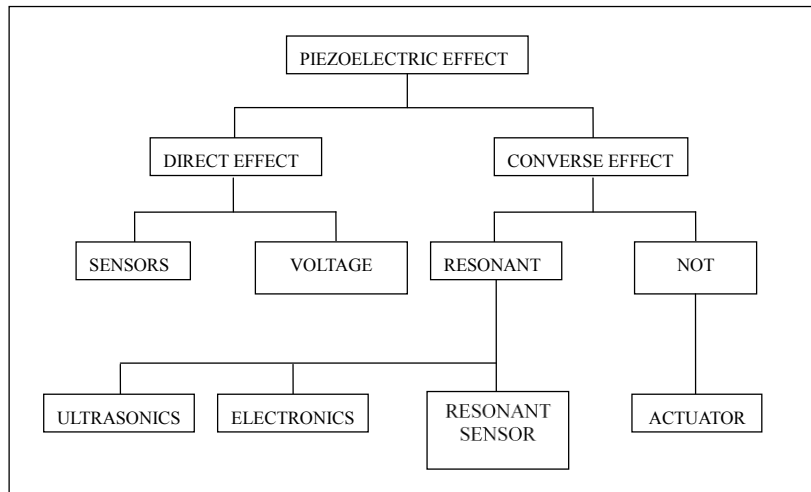


Fig. 2.1 Piezoelectric effect and its application

2.2 The Properties of the PVDF

PVDF has the following characteristics as compared to piezoelectric ceramics.

- (1) Electromechanical conversion efficiency is low, and piezoelectric voltage sensitivity is high.
- (2) Lightweight and flexible, also can withstand impact and bending.
- (3) Acoustic impedance is low.
- (4) Q value is responsive to a wide range of low-frequencies.
- (5) Dielectric constant and the specific heat are low, but contain high pyroelectric voltage sensitivity.
- (6) Thermal diffusion motion is low-level and with excellent spatial resolution.

In this study, the piezoelectric material we are using is a piezoelectric film made by Kureha KF, its electrical properties are shown in the following performance specifications.

Table 2.1 Performance specifications of Kureha KF piezoelectric film (Source: Kureha Chemical Industry Co., Ltd.)

	Symbol	Numerical value	Unit and remarks
Thickness		40	μm
Electrode resistance			Ω
Piezoelectric strain coefficient	d	Drawing direction 30×10^{-12}	C/N (at 10Hz)
		Lateral direction 5×10^{-12}	
Voltage output coefficient	g	0.17~0.26	V·m/N (at 10Hz)
Electromechanical coupling coefficient	k	15	% (at 10Hz)
Pyroelectric coefficient	P	4×10^{-9}	C/cm ² ·deg
Curie temperature	T_C	120	°C
Specific heat at constant volume	C_V	2.5	J/cm ³ ·deg
Thermal conductivity	K	1.3×10^{-3}	W/cm·deg
Thermal diffusion coefficient	α	0.53×10^{-13}	cm ² /sec
Pyroelectric coefficient of performance	$P/C_V \cdot \varepsilon_y$	1.2×10^{-10}	
Modulus of elasticity	c	Drawing direction $3.0 \sim 3.2 \times 10^9$	Pa
		Lateral direction $2.8 \sim 3.0 \times 10^9$	
Maximum tensile stress		Drawing direction $50 \sim 60 \times 10^7$	Pa
		Lateral direction $4.5 \sim 5.5 \times 10^7$	
Degree of elongation		Break 20~30	%
		Yield 5~7	
thermal shrinkage		70°C 1~2	%(Heated for 30 minutes)
Density	ρ	100°C 7~8	g/cm ³
Volume resistivity		1.78~1.79	Ω·cm
Breakdown voltage		$8 \sim 10 \times 10^{14}$	V/mm
Relative permittivity	ε_y	12~13	(at 1kHz)
Dielectric loss tangent		0.015~0.02	(at 1kHz)

2.3 Output Voltage Due to the Piezoelectric Effect

The piezoelectric constitutive law is expressed by the following equations [14, 15]:

$$\boldsymbol{\varepsilon} = \mathbf{s}^E \boldsymbol{\sigma} + \mathbf{d}^T \mathbf{E} \quad (2.1)$$

$$\mathbf{D} = \mathbf{d} \boldsymbol{\sigma} + \boldsymbol{\eta}^T \mathbf{E} \quad (2.2)$$

where $\boldsymbol{\sigma}$ is the stress applied to the dielectrics; \mathbf{d} is the piezoelectric strain constant; \mathbf{E} is the intensity of the electric field; $\boldsymbol{\varepsilon}$ is the strain of the dielectrics; \mathbf{D} is the electric flux density; \mathbf{s}^E is the compliance of the piezoelectric material at fixed \mathbf{E} and $\boldsymbol{\eta}^T$ is the permittivity of the dielectrics at fixed $\boldsymbol{\sigma}$.

Fig. 2.2 shows a coordinate system of the piezoelectric material. Considering only normal strains of the dielectrics, Eq. (2.1) can be written as

$$\begin{Bmatrix} \varepsilon_x \\ \varepsilon_y \\ \varepsilon_z \end{Bmatrix} = \begin{bmatrix} s_{11}^E & s_{12}^E & s_{13}^E \\ s_{21}^E & s_{22}^E & s_{23}^E \\ s_{31}^E & s_{32}^E & s_{33}^E \end{bmatrix} \begin{Bmatrix} \sigma_x \\ \sigma_y \\ \sigma_z \end{Bmatrix} + \begin{bmatrix} 0 & 0 & d_{31} \\ 0 & 0 & d_{32} \\ 0 & 0 & d_{33} \end{bmatrix} \begin{Bmatrix} E_x \\ E_y \\ E_z \end{Bmatrix} \quad (2.3)$$

Solving Eq. (2.3), the normal stresses are

$$\begin{Bmatrix} \sigma_x \\ \sigma_y \\ \sigma_z \end{Bmatrix} = \begin{bmatrix} C_{11}^E & C_{12}^E & C_{13}^E \\ C_{21}^E & C_{22}^E & C_{23}^E \\ C_{31}^E & C_{32}^E & C_{33}^E \end{bmatrix} \begin{Bmatrix} \varepsilon_x \\ \varepsilon_y \\ \varepsilon_z \end{Bmatrix} - \begin{bmatrix} 0 & 0 & e_{31} \\ 0 & 0 & e_{32} \\ 0 & 0 & e_{33} \end{bmatrix} \begin{Bmatrix} E_x \\ E_y \\ E_z \end{Bmatrix} \quad (2.4)$$

where \mathbf{C}^E is a symmetric stiffness matrix, i.e.

$$\mathbf{C}^E = (\mathbf{s}^E)^{-1} \quad (2.5)$$

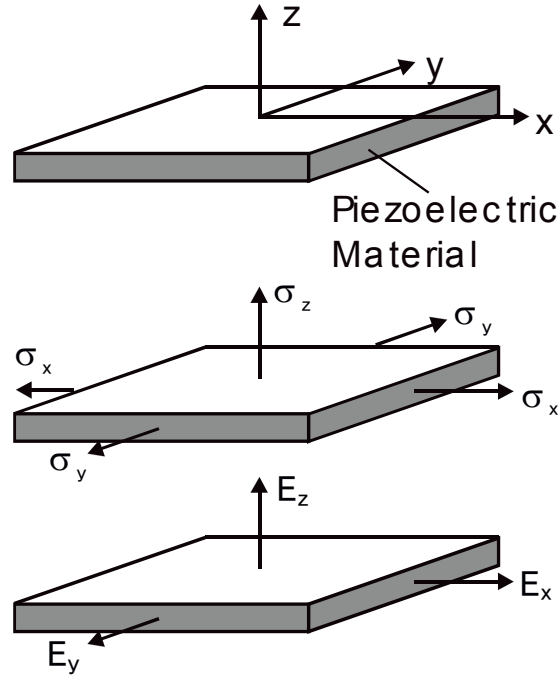


Fig. 2.2 Coordinate system of the piezoelectric material

and

$$\begin{aligned}
 e_{31} &= d_{31}C_{11}^E + d_{32}C_{12}^E + d_{33}C_{13}^E \\
 e_{32} &= d_{31}C_{21}^E + d_{32}C_{22}^E + d_{33}C_{23}^E \\
 e_{33} &= d_{31}C_{31}^E + d_{32}C_{32}^E + d_{33}C_{33}^E
 \end{aligned} \tag{2.6}$$

Eq. (2.4) is also simply expressed as

$$\boldsymbol{\sigma} = \mathbf{C}^E \boldsymbol{\varepsilon} - \mathbf{C}^E \mathbf{d}^T \mathbf{E} = \mathbf{C}^E \boldsymbol{\varepsilon} - \mathbf{e}^T \mathbf{E} \tag{2.7}$$

where

$$\mathbf{e} = (\mathbf{C}^E \mathbf{d}^T)^T = \mathbf{d} \mathbf{C}^E \tag{2.8}$$

\mathbf{e} , the piezoelectric stress constant, is the ratio of the stress change to the change of the electric field when strains of the dielectric are constant.

Substituting Eq. (2.7) into Eq. (2.2), we have

$$\begin{aligned}
\mathbf{D} &= \mathbf{d}\boldsymbol{\sigma} + \boldsymbol{\eta}^T \mathbf{E} \\
&= \mathbf{d}(\mathbf{C}^E \boldsymbol{\varepsilon} - \mathbf{e}^T \mathbf{E}) + \boldsymbol{\eta}^T \mathbf{E} \\
&= \mathbf{dC}^E \boldsymbol{\varepsilon} + (\boldsymbol{\eta}^T - \mathbf{d}\mathbf{e}^T) \mathbf{E} \\
&= \mathbf{e}\boldsymbol{\varepsilon} + \boldsymbol{\eta}^S \mathbf{E}
\end{aligned} \tag{2.9}$$

where

$$\boldsymbol{\eta}^S = \boldsymbol{\eta}^T - \mathbf{d}\mathbf{e}^T \tag{2.10}$$

and $\boldsymbol{\eta}^S$ is the clamped permittivity. Usually, Eq. (2.7) and (2.9) are called as the piezoelectric equations of “e” type, i.e.

$$\boldsymbol{\sigma} = \mathbf{C}^E \boldsymbol{\varepsilon} - \mathbf{e}^T \mathbf{E} \tag{2.11}$$

$$\mathbf{D} = \mathbf{e}\boldsymbol{\varepsilon} + \boldsymbol{\eta}^S \mathbf{E} \tag{2.12}$$

Considering that a piezoelectric element is polarized in the thickness direction, it can be assumed that all matrix elements of the permittivity $\boldsymbol{\eta}^T$ equal zero except η_{33}^T .

Using Eq. (2.10), Eq. (2.9) can be written as:

$$\begin{Bmatrix} D_x \\ D_y \\ D_z \end{Bmatrix} = \begin{bmatrix} 0 & 0 & 0 \\ 0 & 0 & 0 \\ e_{31} & e_{32} & e_{33} \end{bmatrix} \begin{Bmatrix} \varepsilon_x \\ \varepsilon_y \\ \varepsilon_z \end{Bmatrix} + \begin{bmatrix} 0 & 0 & 0 \\ 0 & 0 & 0 \\ 0 & 0 & \eta_{33}^S \end{bmatrix} \begin{Bmatrix} E_x \\ E_y \\ E_z \end{Bmatrix} \tag{2.13}$$

in which

$$\eta_{33}^S = \eta_{33}^T - (d_{31}e_{31} + d_{32}e_{32} + d_{33}e_{33}) \tag{2.14}$$

2.4 Measurement Principle of Piezoelectric Sensor

The output signal of the piezoelectric sensor was measured by connecting a voltmeter to sensor with electrical wires. A recorder NEC OMNIACE RA-1300 was used for this purpose. To the PVDF, under normal circumstances, because of the high insulating properties of the PVDF itself, it can be assumed that no current flows through. After that taking into account the insulating properties of the piezoelectric body itself, PVDF with electrodes also have characteristics of capacitance. Therefore, when considering the electrical circuit for signal processing, PVDF is regard as one capacitor with a current source to calculate the output voltage.

Fig. 2.3 shows an equivalent electrical circuit of the piezoelectric sensor. In the figure, S_1 is the area on which dynamic load is applied, and S_2 is the area on which load is not applied. C_1 and C_2 are the capacitances of the load sensing element corresponding to the areas S_1 and S_2 , respectively. R is the internal resistance of the recorder.

When sinusoidal external load ($P \cdot \sin \omega t$) is applied to the area S_1 , the output voltage V_{out} and phase angle ϕ of the pad sensor can be expressed by the following equations.

$$|V_{out}| = \frac{\omega R \times (kP)}{\sqrt{1 + \{R\omega(C_1 + C_2)\}^2}} \quad (2.15)$$

$$\phi = \tan^{-1} \{1 / R\omega(C_1 + C_2)\} \quad (2.16)$$

in which k is a coefficient.

In the above equations, the magnitude of V_{out} depends on the sum of the capacitance

$(C_1 + C_2)$ and is independent on the value of C_1 . This means that V_{out} is only influenced by the total area of the sensing element (S_1+S_2), but not influenced by the load applied area S_1 .

Two conditions will occur regarding to the capacitance. If $(C_1 + C_2)$ is small, V_{out} becomes proportional to the load speed ω as V_{out} approaches to $|V_{out}| = \omega R \times (kP)$. However, if $(C_1 + C_2)$ is large, V_{out} becomes proportional to the external load itself as $|V_{out}| = kP / (C_1 + C_2)$.

With regard to the value of R and ω , if both values are large, V_{out} becomes proportional to the external load as V_{out} approaches to $|V_{out}| = kP / (C_1 + C_2)$.

From the Eq. (2.16), the phase angle between V_{out} and the external load becomes zero when the value of R , ω or $(C_1 + C_2)$ is large.

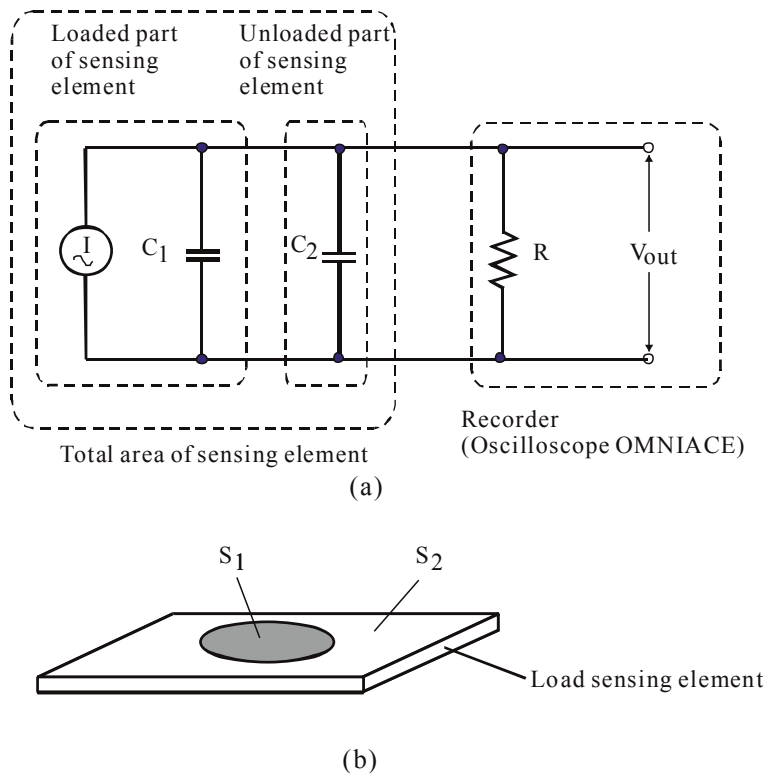


Fig. 2.3 Equivalent electrical circuit of the sensor

References

- [1] Kawai, H., (1969) The Piezoelectricity of Poly (Vinylidene Fluoride). *Japanese J Appl. Phys*, 8(7), 975-976.
- [2] Rao, S.S. and Sunar, M. (1994) Piezoelectricity and Its Use in Disturbance Sensing and Control of Flexible Structures: A survey, *Appl. Mech. Rev.*, 47, 4, 113-123.
- [3] Crawly, E.F. (1994) Intelligent Structures for Aerospace: A Technology Overview and Assessment, *AIAA Journal*, 32, 8, 1689-1699.
- [4] Auld, B.A., Gagnepain, J.J. (1979) Shear Properties of Polarized PVF2 Film Studied by Piezoelectric Resonance Method. *J Appl Phys*, 50(8), 5511-5512.
- [5] Wang, T.T., (1982) Stress Relaxation and Its Influence on Piezoelectric Retention Characteristics of Uniaxially Stretched Polyvinylidene Fluoride Films, *J Appl Phys*, 53(3), 1828-1829.
- [6] Katsumi, K., Biwa, S., Matsumoto, E. and Shibata, T. (1999) Measurement of Static Strain Distribution Using Piezoelectric Polymer Film (Principle and Application to a Hinged Plate), *Solid Mechanics and Material Engineering, Series A, JSME International Journal*, 42, 1, 11-16.
- [7] Mazurek, B., Janiczek, T. and Chmielowiec, J. (2001) Assessment of Vehicle Weight Measurement Method Using PVDF Transducers, *Journal of Electrostatics* 51-52, 76-81.
- [8] May, E.L. (2003) Application of a Piezoelectric Sensor for Measuring Shivering in a Small Marsupial, *Journal of Thermal Biology* 28, 469-475.
- [9] Liu, G., Fujimoto, Y., Shintaku, E., Wakabayashi, S., Masaguchi, T. and Komatsubara, N. (2002) Application of PVDF Film to Stress Measurement of Structural Member, *Journal of The Society of Naval Architects of Japan*, 192, 591-599.
- [10] Fujimoto, Y. and Liu, G. (2004) Stress Intensity Factor Measurement of Cracks Using Piezoelectric Element, *Experimental Mechanics*, 44, 3, 320-325.
- [11] Volf, J., Holy, S. and Vleck, J. (1997) Using of Tactile Transducer for Pressure-Distribution Measurement on the Sole of the Foot, *Sensors and Actuators, A2*, 556-561
- [12] Shimojo, M., Namiki, A., Ishikawa, M., Makino, R. and Mabuchi, K. (2004) A Tactile Sensor Sheet Using Pressure Conductive Rubber with Electrical-Wires Stitched Method, *IEEE Sensor Journal*, 4, 5, 589-595.
- [13] Onori, G., Koga, Y., Bechtold, J.E., Gustilo, R.B., Nakabe, N., Sasakawa, K., Hara, T. and Takahashi, H.E. (1997) Contact Pressure and Three- Dimensional Tracking of Unresurfaced Patella in Total Knee Arthroplasty, *The Nee*, 4, 15-21.
- [14] Ikeda, T., (1990) *Fundamentals of Piezoelectricity*, Oxford Univ. Press, NY.
- [15] Okazaki, K., (1992) *Engineering of the Ceramics Dielectrics*, Gakkensya.

Chapter 3 Three Types of Piezoelectric Sensor Developed as Load Sensing Element

In this study, some new piezoelectric sensors using PVDF (polyvinylidene fluoride) film was developed to measure a wide range of dynamic pressures caused by several kinds of impact loads. PVDF film is a very thin piezoelectric material and it generates electric charge according to the applied strain. Three kinds of prototype sensors which are sheet-type impact force sensor, pad sensor and fluctuating load detection plate were developed as load sensing element.

And the performance of these three types has been clarified in a variety of impact tests. Sheet-type sensor has a structure in which silicone rubber sheets are pasted on both surfaces of the piezoelectric film. By strain amplification effect of silicon rubber, even small impact force is still possible to accurately measure. The pad sensor consists of a piezoelectric film sandwiched between two pieces of metal sheet, and the whole body is laminated by the resin film. The pad sensor features light-weighting and high-rigidity in thickness direction, therefore, it is verified that the thin pad sensor can be used to measure the greater extent high-speed impact compared to the conventional load cell. The fluctuating load detection plate owns the structure that two metal plates grip a pad sensor and tightened with bolts. Since the fluctuating load detection plate possesses the metal plates, it can only be used in the plane, but it still can accept impact from hard object. The accuracy of these sensors are demonstrated based on the measurements of the waveform impulse and the momentum theory.

3.1 Basic Structure of Three Types of Piezoelectric Sensor

3.1.1 Sheet-Type Sensor

The sheet-type sensor is made up of PVDF film and silicon sheet. A PVDF film (40 μm thickness) with aluminum electrode on both surfaces was cut into square with size of 26cm \times 26cm. To transmit the electric charges from PVDF film to the measurement instrument, the electric terminals were attached on the upper and lower electrodes by using metal tape and conductive adhesive. The electric wires were connected to the electrodes by the soldering.

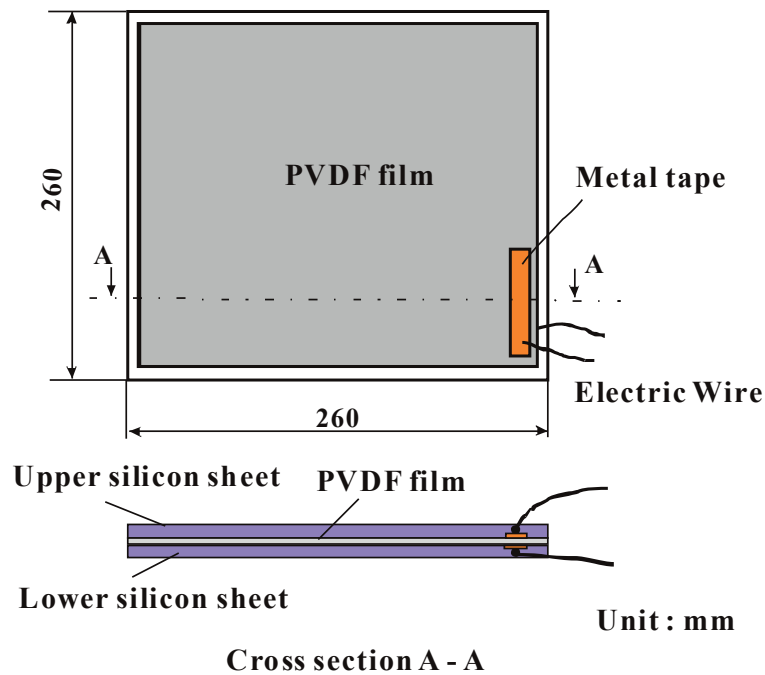


Fig. 3.1 Load sensing element

Then, two pieces of square silicon sheet with area of 28cm \times 28cm and thickness of 1mm were cemented onto the both upper and lower surfaces of aluminum electrode with silicon adhesive. The complete description of the load sensing element is shown in Fig.3.1.

Performance of the sheet-type sensor, such as the sensitivity and the stability of the sensor output, can be improved by adding an absorbing material onto the both surfaces of the load sensing element. In this study, rubber sheets with area of 30cm×30cm square and 10mm thickness were placed on both surfaces of the load sensing element. Due to the characteristic of the rubber sponge, a rough load distribution applied to the pad surface is improved to a smooth distribution and then transmitted to the load sensing element.

In order to make the load sensing element and the load absorbing element into one body, an envelope made from canvas clothe was used for the cover sheet. The canvas clothe can easily deform in the thickness direction and transmit the applied normal load to the absorbing element. On the other hand the canvas clothe has certain rigidity to the surface direction, so the shear load induced between the loading body and the cover sheet can be prevented by the slipping effect. Fig.3.2 shows the construction of the developed piezoelectric sheet-type sensor.

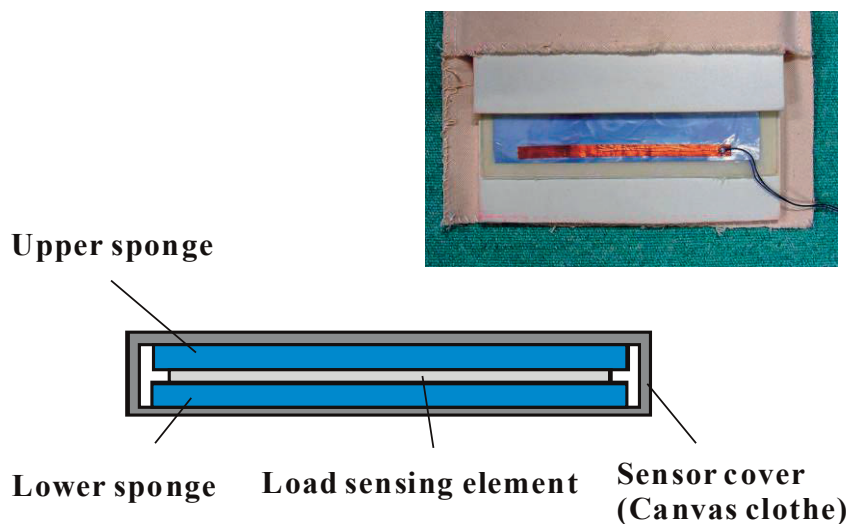


Fig. 3.2 PVDF sheet-type sensor with cover sheet

In order to examine the performance of the piezoelectric sheet-type sensor, such as sensitivity, linearity and repeatability of the sensor, experiments were carried out by

applying several types of dynamic loads to the surface of the pad sensor.

Fig.3.3 and Fig.3.4 show the piezoelectric pad sensor placed on a load cell. The load cell works as the reference of the output measurement. The output signal of the load cell was measured by strain indicator KYOWA YA-504 B and read by the recorder NEC OMNIACE RA-1200.

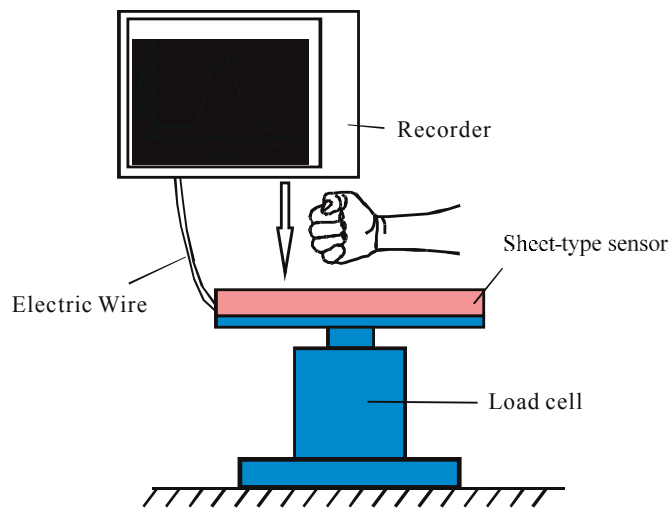


Fig. 3.3 Measurement set-up

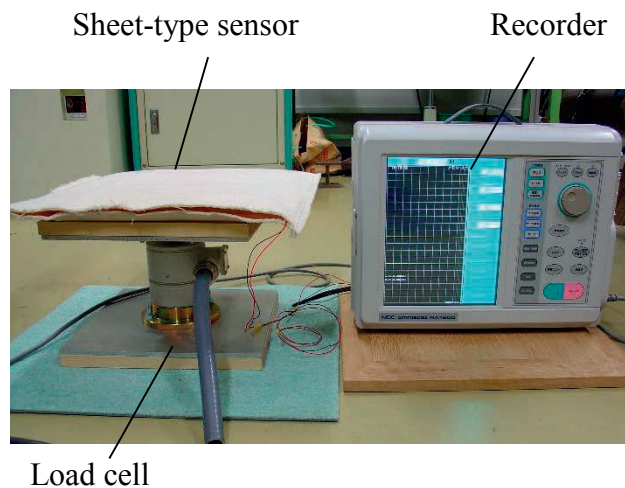


Fig. 3.4 Experimental set-up

Fig.3.5 compares the output waveforms of the sheet-type sensor for the three types

of impact loads with different load speed. Bamboo bar punching is the impact load applied like a whip and it gives the highest speed. Hand punching is the impact load applied by a fist punching, and elbow punching is given by a hand elbow.

From the figure, it is seen that the wave shape of high speed impact load exceeding 1 kHz can be clearly obtained by the use of the proposed sheet-type sensor.

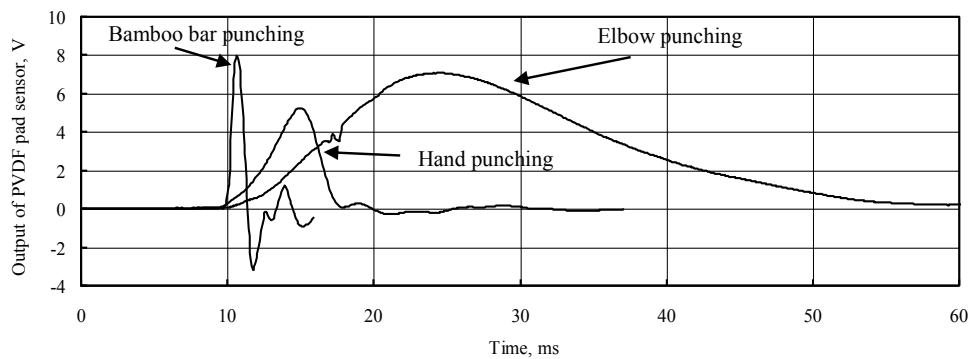


Fig. 3.5 Waveforms of the sheet-type sensor output for high impact loads

3.1.2 Pad Sensor

The high-speed impulsive force waveform whose shock time from contact to separation is below 1 millisecond usually will produce residual vibration because of the overlap and resonance of subtle shock waves.

For the reason that, the main issue of which the impact sensor could measure short shock time wave is that the natural frequency of sensor must be high. In order to ensure a high natural frequency, there should be two major preconditions, the small sensor mass and the high rigidity in detection direction of the sensor (spring constant). However, generally with the improved rigidity, the mass of sensor is also increasing at the same time. On the contrary, if we make a small mass sensor, the rigidity will become lower. Therefore, generally speaking the small mass and high rigidity of the sensor are inconsistent, so the development of the sensor for measuring the impulsive force is of

great difficulty.

In the process of developing the impulsive force sensor which uses the piezoelectric film, we noticed a way to overcome this inconsistency.

Piezoelectric film is a kind of resin film whose elastic modulus is 1/70 of that of steel [1]. Although generally considered its elastic modulus is small, and not suitable for high-speed load and large load measurement, if the thickness is small, we think that the developing of the high-speed and large load sensor is likely to be achieved. Through the comparison with the basic load cell, Fig.3.6 illustrates the reason. By the material mechanics, when the compressive load acts on the load cell, the amount of deformation in the thickness direction

$$\delta = PL/AE \quad (3.1)$$

Where

L : Gauge length of the sensor, A : Load receiving area, E : Young's modulus of detector.

Here, spring constant is

$$k = AE/L \quad (3.2)$$

Then we will obtain

$$P = k\delta. \quad (3.3)$$

Compare to the elastic modulus of load cell's metal bar, the elastic modulus of piezoelectric film is obviously small. For film-like as shown in Fig.3.6 (a), the receiving area could be made large. Further, in the load cell the gauge length L require a few millimeters necessarily as shown in Fig.3.6 (b), but the L of the piezoelectric film can be made far below 0.1mm. The result is that, for example, if compared to load cell, under the situation of that E is 1/70, A is 10 times and L is 1/50, then spring constant k will be k

$=10/70 \times 50 = 7.1$, which is 7 times that of load cell.

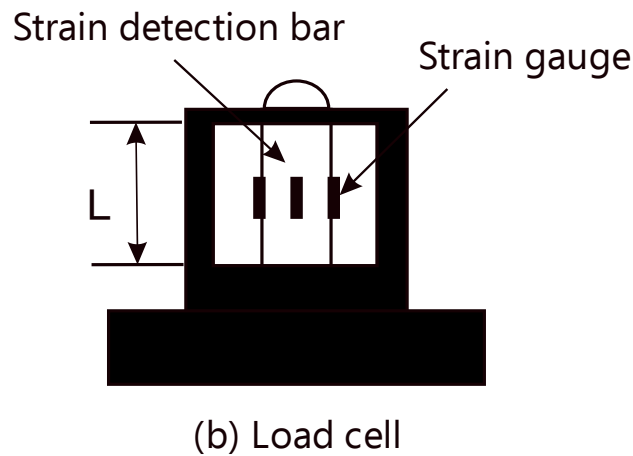
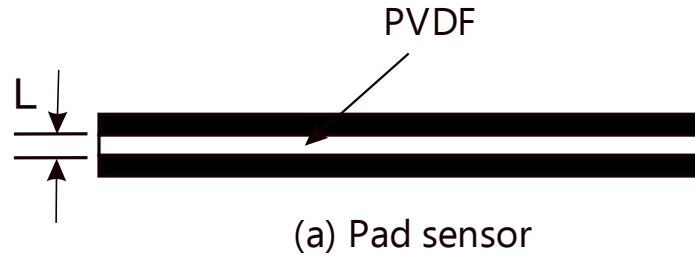


Fig. 3.6 Structure of pad sensor and load cell

Fig.3.7 shows the cross-sectional structure of the pad sensor. As this figure, PVDF placed in the center is sandwiched between two layers of metal sheets whose thickness is from 0.08 to 0.5mm, then they are all laminated by a layer of polyester resin. There are two types of functions about the covering metal sheets, one is that to be used as the electrodes of the PVDF, the other one is that to protect the PVDF. There are two wires installed connecting to the outside of sensor. According to this configuration, the thickness of our sensor can be limited in the 1mm.

Fig.3.8 shows a prototype of pad sensor. The material we used is PVDF (thickness is $80\mu\text{m}$), stainless steel sheet (thickness is 0.1mm) and laminate sheets (thickness is 0.1mm).

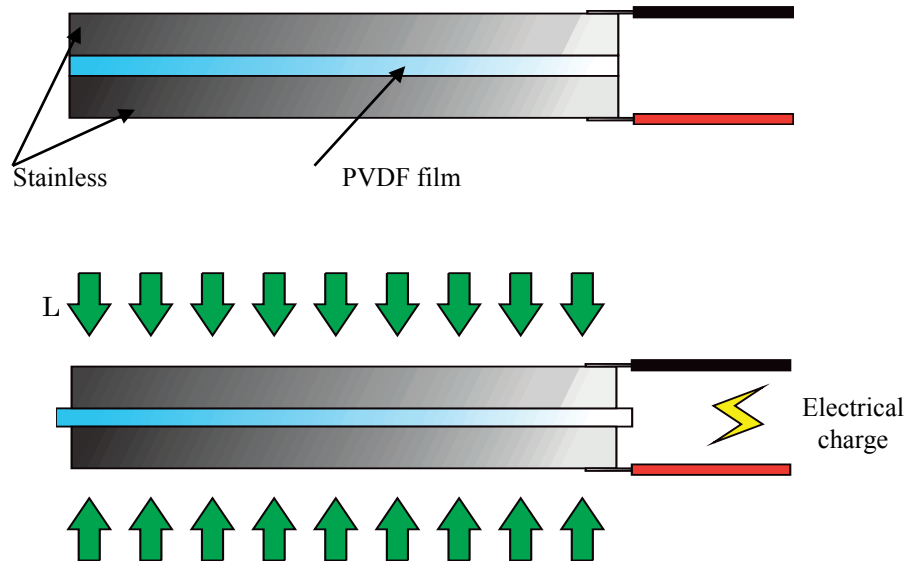


Fig. 3.7 Cross-sectional structure of the pad sensor

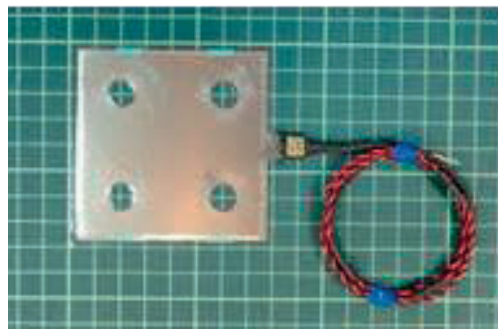


Fig. 3.8 60×60mm prototype pad sensor

3.1.3 Fluctuating Load Detection Plate

In the case of fluctuating load detection plate, for the purpose of preventing the piezoelectric element from damaging by the large and high-speed impulsive force, by the use of screws, we could fix two metal plates to grip the pad sensor above and below. About the materials of metal plates there are several options. We can choose according to requires, such as aluminum and steel. We will mention it in this section. And Fig.3.9 is the photo when the detection plate is accomplished.

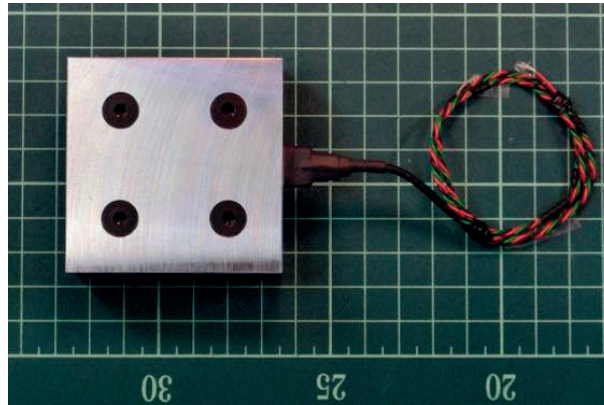


Fig. 3.9 Complete photo of fluctuating load detection plate (covered with metal plate)



Fig. 3.10 200kN servo-hydraulic testing machine

The fluctuating load detection plate we made was carried out a performance evaluation experiments. In the experiment a 200kN servo-hydraulic testing machine is utilized. The content of the experiment is that we put the detection plate on the table of this machine, and we applied a -40kN average load in 9 steps incrementally on the sensor in the frequency of 2Hz. Fig.3.10 shows the experimental set up. Dynamic load is applied to simulate real work conditions, the output signals of load detection plate are recorded by NEC OmniaceII RA1300 (Fig.3.11) and analyzed by computer. Fig.3.12 shows the

output waveform of the experiment.



Fig. 3.11 High-speed voltage recorder

The waveforms shown in Fig.3.12 obtained in the performance evaluation test represent the outputs of sensors and load cell, then we recorded the voltage range between the peak value of the waveform and the bottom in each cycle (as shown in Fig.3.13). Fig.3.14 shows that linear relationship between the loads indicated by the horizontal axis and the voltage output indicated by the vertical axis. The gradient of this line can be used to convert electrical signals into mechanical signals.

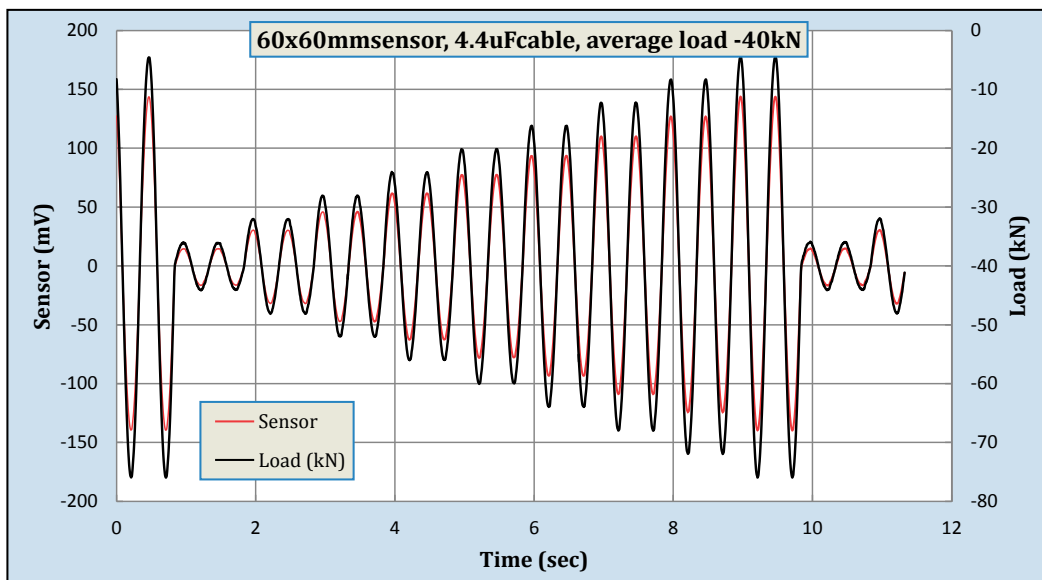


Fig. 3.12 Output of sensor and load in 9 block steps

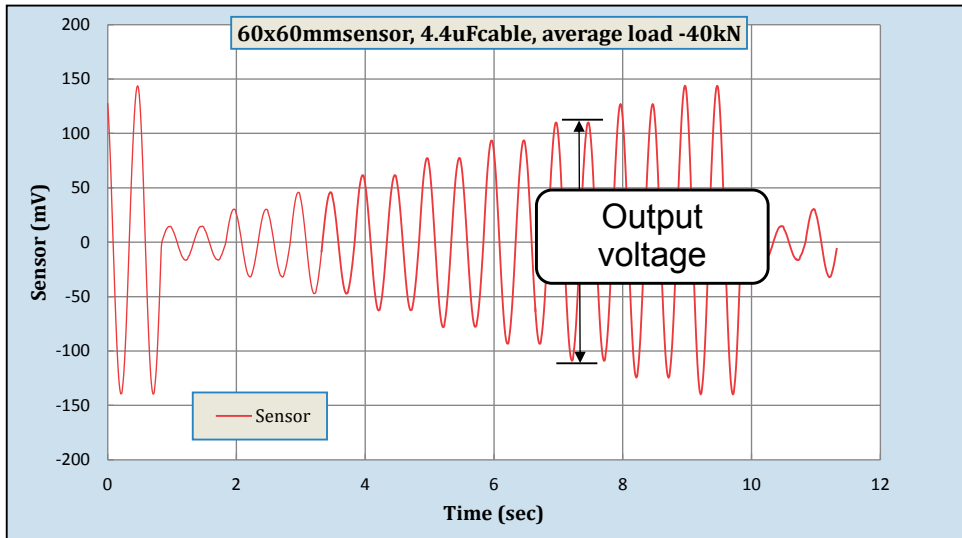


Fig. 3.13 Output of sensor in evaluation experiments

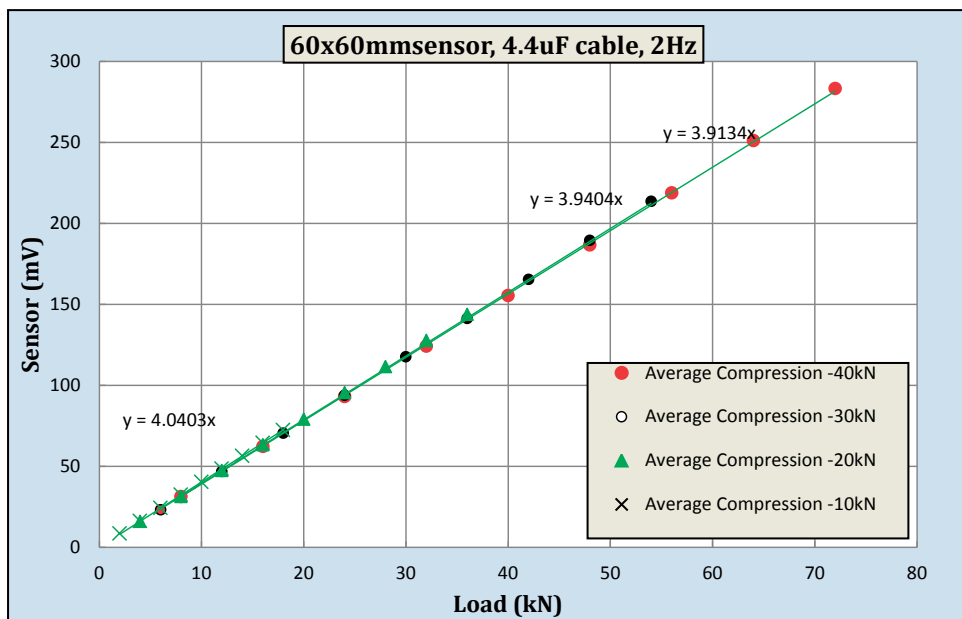


Fig. 3.14 Relationship of load and voltage output

According to Fig.3.14, we can realize even though the average compression is different, the gradient of the relationship maintains a good linearity, it indicates that the load detection plate can fulfill the requirements of the accuracy satisfyingly.

Compared with the pad sensor, fluctuating load detection plate has a disadvantage that mass increases, but appearing the merit that the sensor becomes into a rigid structure

against collision body.

3.2 Some Application Examples Using Piezoelectric Sensor Developed in This Study

3.2.1 The Falling Experiment of the Lead Ball and Steel Ball

Because the natural frequency of the load detection plate is high, the impact force can be measured in the high-speed and high-load conditions. Through verification test the high-speed impact whose contact time is about 0.1 ~ 1msec also can be measured. Also, since the compressive stress can be measured up to about 50MPa, which means it has a load capacity of about 100kN of fluctuating load detection plate with 50mm square dimensions. Then taking advantages of the response performance against the impulsive force, we carried out the drop test of lead ball and steel ball (impact close to the perfectly inelastic collision).

3.2.1.1 Experiments Conditions and the Design of the Experiment Devices

In order to obtain a controllable experiment conditions, we design a device of falling ball system as shown in Fig.3.15.

In this experiment, the materials of falling ball we choose are lead and steel, weight of lead ball is 105g, weight of steel ball is 67g weight, surface of sensor is covered aluminum alloy plate (A5052 surface) and the size of the load detection plate we designed is 60mm×60mm. Through using the different pipe, we could control the drop height of the free falling balls from 0.1m to 2m. The measurement equipment we are using is a

high-speed voltage recorder (NEC Avio, Omni ace RA2300 in Fig.3.16), and is set in 200kHz sampling rate. Fig.3.17 shows the real experimental landscape.

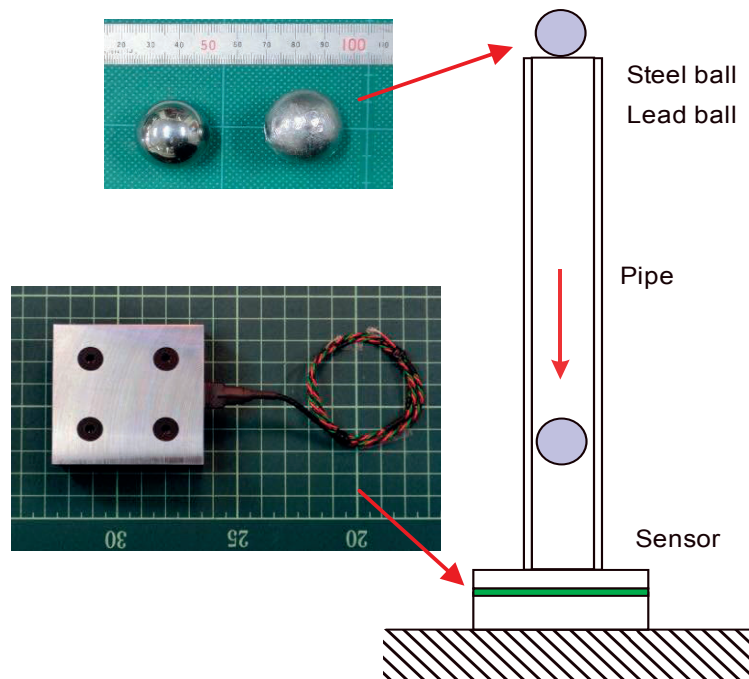


Fig. 3.15 System of ball falling experiment

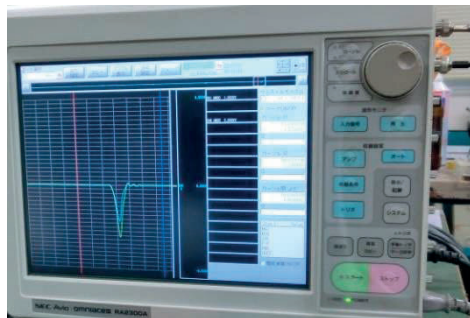


Fig. 3.16 High-speed voltage recorder



Fig. 3.17 Experiment landscape of ball falling experiment

3.2.1.2 Experiment Results and Analysis

After several drop tests, some flat plastic deformations occurred. The left figure of Fig.3.18 shows the plastic deformations of the lead ball, the right figure of Fig.3.18 shows the plastic deformation of the aluminum plate on the sensor. Because of these plastic deformations we consider that the collision is in an approximately non-bounce condition.

Fig.3.19 shows the waveform of the lead ball falling impulsive force. The shock time is short and close to 0.2msec with seldom residual vibration. In an elastic collision, the waveform is usually symmetrical even if the shock time is short [2]. However, in Fig.3.19 we may notice the waveform is asymmetrical, and loading time is longer than the unloading time.



Fig. 3.18 Deformation on the ball and surface of sensor

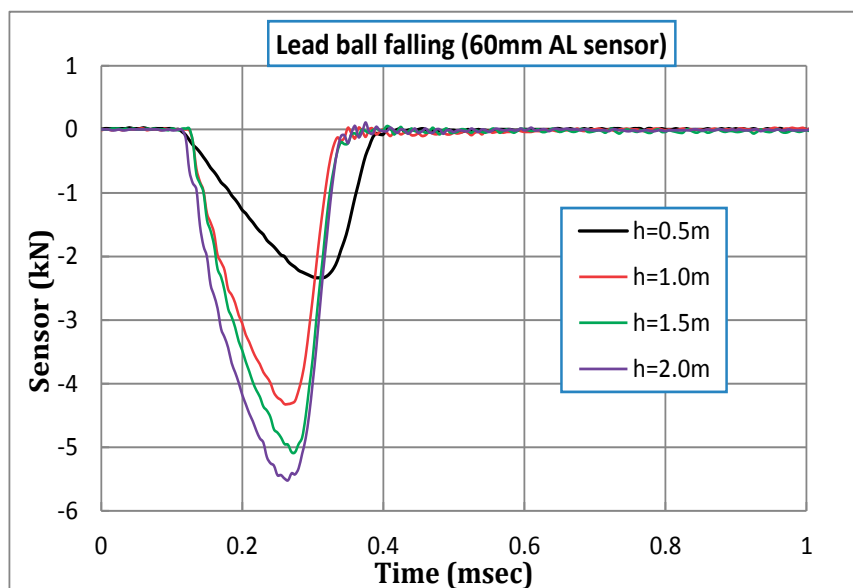


Fig. 3.19 Waveform of lead ball falling experiment

Fig.3.20 shows the waveform of the steel ball falling. The peak impact force in the case of $h = 2.0\text{m}$ fall height is about 8.19kN , which is about 12,300 times the load of the static steel ball. The shock time of the impact force is about 0.1msec . If considering the part of vibration during downloading, the whole time is about 0.2msec . Therefore, the impact is such high-speed. The impact force waveform exhibits an asymmetric waveform; the gradient of downloading waveform is steeper than the gradient of uploading waveform. The reason is considered caused by the plastic deformation of the sensor surface.

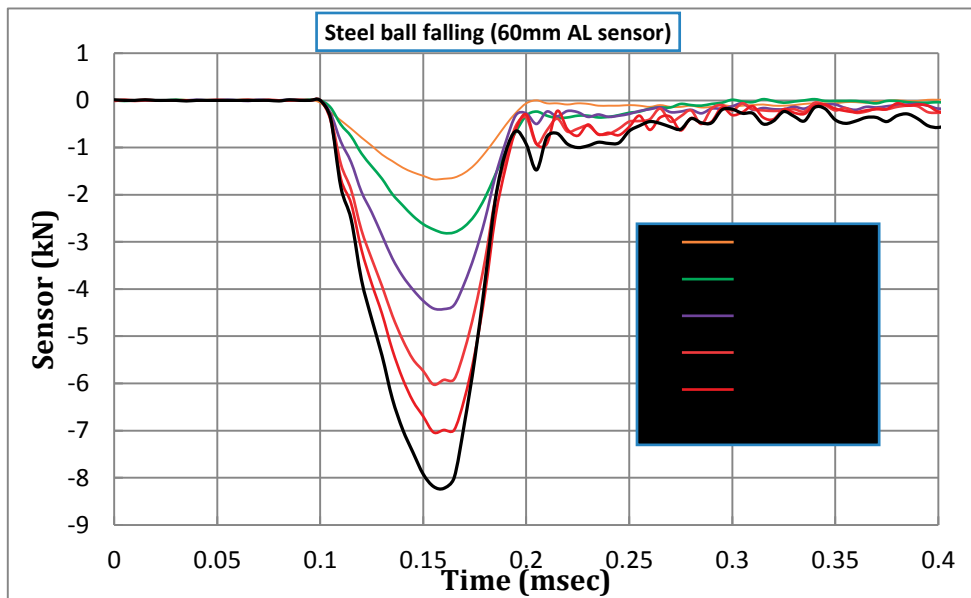


Fig. 3.20 Waveform of the steel ball falling experiment

It's based on the work-energy principle, average impact force times the distance traveled equals the change in kinetic energy. It is indeed a specific application of the law of conservation of energy, which states that the potential energy (PE) before an event must equal the kinetic energy (KE) after an event.

$$PE=KE \quad (3.4)$$

For a simple drop test, the conservation-of-energy equation is:

$$mgh = \frac{1}{2}mV^2 \quad (3.5)$$

Where:

m = mass, h = drop height, g = acceleration of gravity, v = velocity at impact

The impact velocity is independent of mass. Solving the conservation of energy equation above and neglecting drag forces caused by air resistance, velocity is calculated from:

$$v = \sqrt{2gh} \quad (3.6)$$

$$mV = \int_0^T F(t)dt \quad (3.7)$$

Using the law of conservation of momentum, we can calculate the momentum of lead ball, and according to the area integration of the waveform, we can obtain the impulse of impact as the Table 3.1 shown.

Table 3.1 Impulse and momentum calculated from lead ball falling experiment

Mass of lead ball m (kg)	Falling height h (m)	Momentum mV (Nsec)	Impulse calculated from impact force wave (Nsec)	Peak impact force (kN)
0.105	0.5	0.329	0.371	2.22
	1	0.465	0.535	4.25
	1.5	0.569	0.645	5.08
	2	0.657	0.748	5.45

In Table 3.1, we notice that the approximately 15% of the lead ball impulse is larger than the amount of falling momentum. This is considered caused by the little rebound of the lead ball.

In the steel ball falling test, we realize that after collision the ball will rebound into air. In order to calculate the result, we have done some modifications to formula. V_0 indicates the velocity before the collision, after time T the collision finish, the steel ball

will rebound in air at a speed of V_1 . The formula has become

$$mV_0 - mV_1 = \int_0^T F(t)dt \quad (3.8)$$

Since the steel ball is free falling at height of h_0 , and rebound to the height of h_1 , in that way, the coefficient of rebound e can be calculated in this formula,

$$e = \frac{-V_1}{V_0} = \frac{\sqrt{2gh_1}}{\sqrt{2gh_0}} = \frac{\sqrt{h_1}}{\sqrt{h_0}} \quad (3.9)$$

When it is perfectly elastic collision, $e = 1$. When it is inelastic collision, $0 < e < 1$, when there is no rebound, $e = 0$. Bring the e into the previous formula,

$$mV_0(1 + e) = \int_0^T F(t)dt \quad (3.10)$$

After measured, we have confirmed the value of coefficient of rebound e in this situation is 0.316.

Table 3.2 Impulse and momentum calculated from steel ball falling experiment

Mass of steel ball m (kg)	Falling height h (m)	Momentum mV (Nsec)	mV(1+e) (Nsec)	Impulse calculated from impact force wave (Nsec)	Peak impact force (kN)
0.067	0.1	0.094	0.123	0.118	1.65
	0.3	0.148	0.195	0.192	2.88
	0.5	0.210	0.276	0.280	4.41
	1.0	0.297	0.390	0.395	6.03
	1.5	0.363	0.478	0.462	7.04
	2.0	0.419	0.552	0.531	8.19

Coefficient of rebound $e=0.316$

In the Table 3.2 we can observe that the impulse calculated from impact force wave is in good agreement with the theoretical value of the momentum. This is confirmed that our sensor is effective to measure the high-speed impulsive.

3.2.1.3 Steel Ball Falling Experiment by the Use of Steel Plate Covered Sensor

In order to examine the further availability of sensor in different contact surface conditions, we change the size of sensor and the material of the upper metal plates.

We made two different size sensors, 40×40mm and 32×32mm. In the previous two experiments, we noticed the peak impact in the steel ball experiment is much larger than values of the lead ball experiments even though the mass of steel ball is smaller than the lead ball. Therefore we are going to attempt the stiffer contact surface condition and we choose the SS400 mild steel (40 × 40mm size, 10mm thick top plate, 5mm thick bottom plate) and S45C steel (32 × 32mm size, 16mm thick top plate, 10mm thick bottom plate). Fig.3.21 and Fig.3.22 shows the pictures of the actual object. In addition to size and material, the structure of sensor is almost the same with the previous ones'. We carried out several falling test from different heights, $h=0.5\text{m}\sim 2.0\text{m}$. In order to reinforced strength, we placed a 40mm thick metal plate on the bottom of experiment device and adhered to the hard concrete floor as shown in Fig.3.23

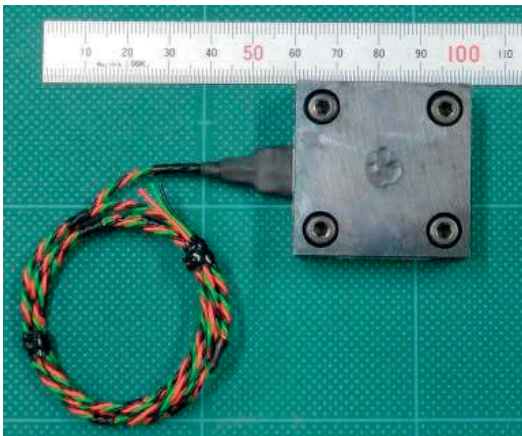


Fig. 3.21 SS400 surface 40×40mm sensor

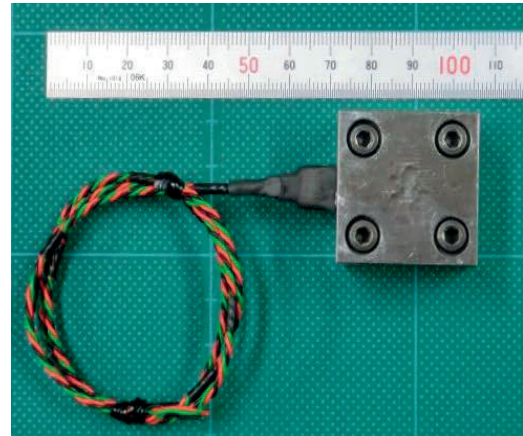


Fig. 3.22 S45C surface 32×32mm sensor

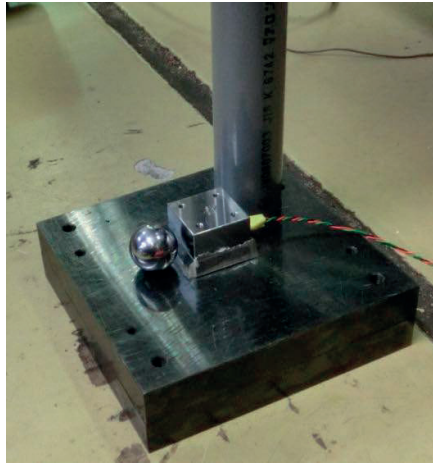


Fig. 3.23 Setup of steel ball falling test

3.2.1.4 Experiment Results and Analysis

In Fig.3.21, we can also observe the surface of the sensor which was carried out to free fall through a pipe from a height $h = 0.5\text{m} \sim 2.0\text{m}$. The measurement was measured at the sampling rate $3\mu\text{sec}$.

SS400 plate's deformation on the surface is some slight concaves, and ball rebounded to about 28% of the falling height. This corresponds to a coefficient of rebound $e = 0.53$.

Fig.3.24 shows the waveform of the impact force, the impact time is high-speed, about 0.07msec in the case of $h=2.0\text{m}$ and 0.08msec in the case of $h = 0.5\text{m}$. After impact there is shaking vibration occurs slightly on tensile side. Peak impact force in the case of $h = 2.0\text{m}$ is about 16.4kN, which is about 24,600 times static load force (0.666N) of steel ball.

Fig.3.22 shows a photograph about the top surface of the sensor after the experiment. There are still some slight concaves on the surface of S45C plate after several tests. According to video recording, steel ball bounced up to about 26% of the drop height.

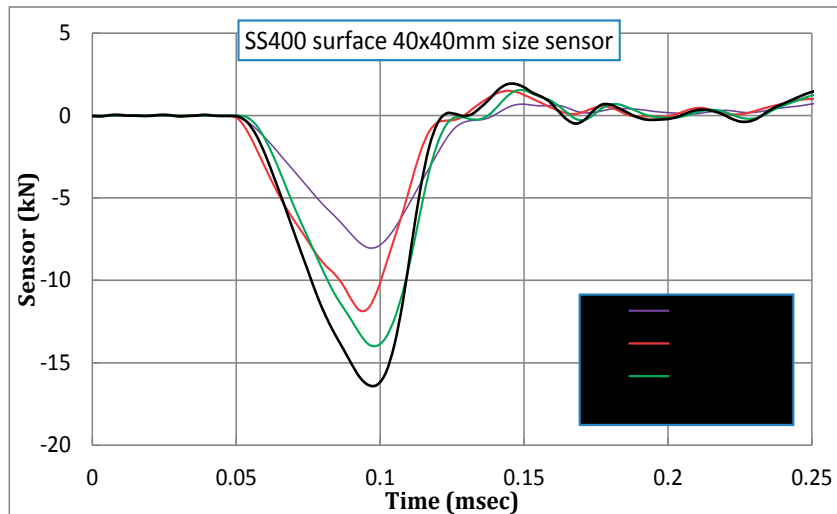


Fig. 3.24 Impact force of steel ball drop onto SS400 sensor

Fig.3.25 shows the waveform of the impact force, the impact time is high-speed, about 0.06msec in the case of $h=2.0\text{m}$ and 0.07msec in the case of $h = 0.5\text{m}$. Peak impact force in the case of $h = 2.0\text{m}$ is about 19.8kN, which is about 29700 times static load force (0.666N) of steel ball.

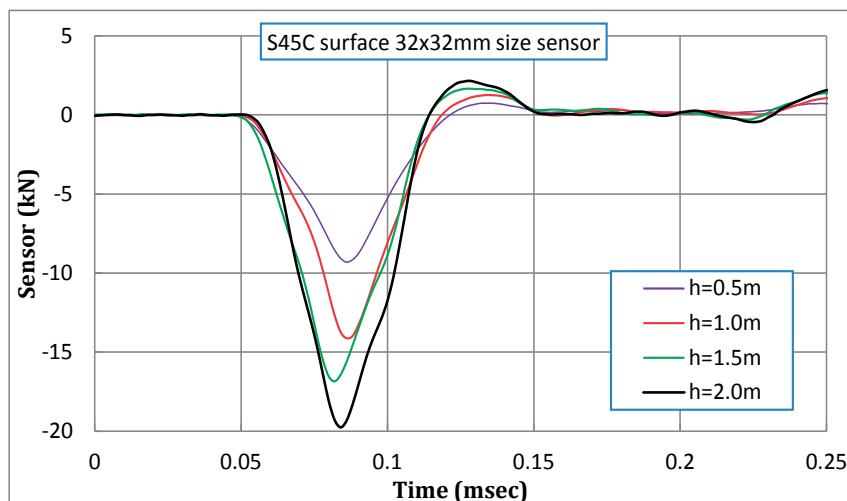


Fig. 3.25 Impact force of steel ball drop onto S45C sensor

Impulsive force waveform shown in Fig.3.25 is not smooth, and undulating slightly while compressive load is acting, but there is still shaking vibration occurs slightly on tensile side.

Table 3.3 Impulse and momentum calculated from steel falling experiment with S45C and SS400 sensor

S45C sensor	Fall height h (m)	Momentum mV (N · sec)	mV(1+e) (N · sec)	Impulse (N · sec)	Shockperiod (μ sec)	Peak load (kN)
<i>Coefficient of restitution e=0.51</i>	0.5	0.213	0.321	0.313	70	9.07
	1	0.301	0.455	0.441	66	14.6
	1.5	0.369	0.557	0.539	64	18.1
	2	0.426	0.643	0.610	62	19.8
SS400 sensor	Fall height h (m)	Momentum mV (N · sec)	mV(1+e) (N · sec)	Impulse (N · sec)	Shockperiod (μ sec)	Peak load (kN)
<i>Coefficient of restitution e=0.53</i>	0.5	0.213	0.326	0.332	83	8.03
	1	0.301	0.460	0.448	76	12.4
	1.5	0.369	0.564	0.535	74	13.9
	2	0.426	0.651	0.618	72	16.4

Comparing Fig.3.24 and Fig.3.25, then in the case of SS400, S45C as surface is obtained the larger peak impact force when the steel ball was dropped from the same height. Further, shock time of S45C case is slightly shorter than in the case of SS400. It is considered that SS400 is stiffer than S45C.

During several ball free falling test, we obtained some high-speed impulsive force to be measured. We have confirmed our sensor could perform normally in different hardness contact surface. However, the problems about the residual vibration still need to solve in the future researches.

3.2.2 Drop Test of Longitudinally Turning Bar and Used Sensors

In this experiment, we developed a longitudinally turning bar system and observed an interesting phenomenon. When the head of shaft fall onto the sensor, the waveform of the collision will emerge a double-strike shape. This double-strike phenomenon can be occurred by twice beating from transient vibration such as in the ball game when collision between the ball and the equipment, or when you hold a hammer hit a bar tip or plate center[3]. It also can be mainly found by deformation seen in the process of impact buckling of member or heel landing of running [4]. The double-strike related to the vibration of the plate and bar [5] can be regarded important in engineering such as

assembly and processing, and the double-strike related to the deformation can be regarded important in medical care and sports fields.

For elucidation of double-strike phenomenon, although some analysis techniques are valid such as vibration studies [6], elastic wave theory, dynamic simulation. On the other hand, since after-impact exercise, vibration, and the deformation involved complicatedly, approaching from phenomena surface with high-speed shooting and various sensors are also important. This test, using fluctuating load detection plate [7] having an excellent high-speed response, is going to investigate this phenomenon experimentally. In order to figure out this phenomenon, we designed some more experiments with a strain gauge installed on the shaft.

3.2.2.1 Experimental Conditions and Used Devices

Fig.3.26 shows the system of this experiment. This steel shaft is fixed by a hinge on an end, and we release the hand in a predetermined inclination angle, the shaft will fall to horizontal position. Aimed to observe the waveform in detail, we add an upper sensor near the topside of shaft, the sensors we are using is shown in Fig.3.27.

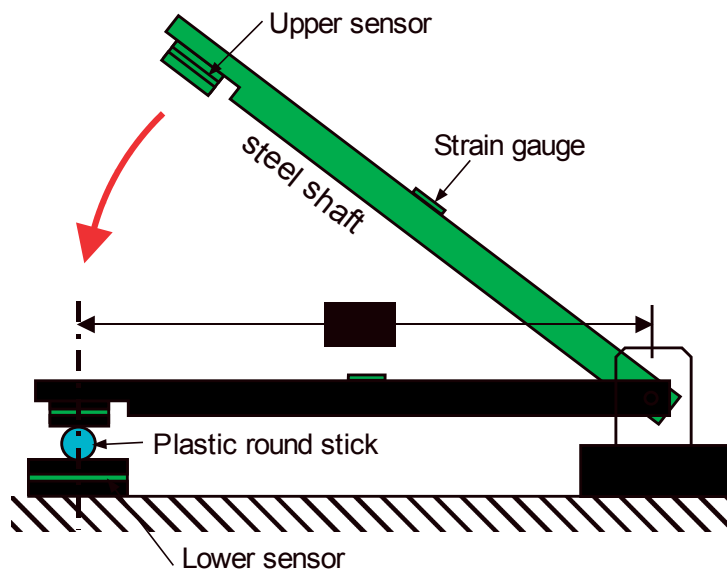


Fig. 3.26 system designed for drop test of longitudinally turning bar

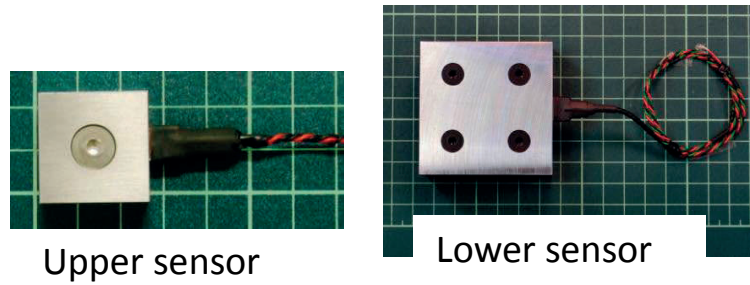


Fig. 3.27 Sensor using in the drop test of longitudinally turning bar

Shaft material is steel with 16mm diameter and 500mm length. Near the tip of the shaft it was carried out a D cut to adjust to install a 25mm squared stainless made sensor which is adhered on the incision by double-sided tape. And we placed a 60mm squared lower sensor on floor with a 10mm resin bar adhered on it by double-sided tape. In addition, the place where we set the resin bar could make the bar exactly hit the center of the upper sensor. From the hinge to the hit point of the resin bar, the distance is $L=480\text{mm}$. Furthermore, a strain gauge is attached to the center of the length of the steel shaft and hence we can measure the bending vibration of the shaft.

3.2.2.2 Experimental results and analysis

In the first experiment, we lift up the tip of the steel shaft to about 30 degree from the horizontal and release. The upper sensor will strike the resin bar firstly and then bounce back. And after 150-200msec (in the case of 30 degree fall angle), it strikes the resin bar secondly. However, the double-strike phenomenon in this chapter is quite different with this; the double-strike phenomenon we will discuss is that only in the first strike there are two strikes observed on the impact waveform.

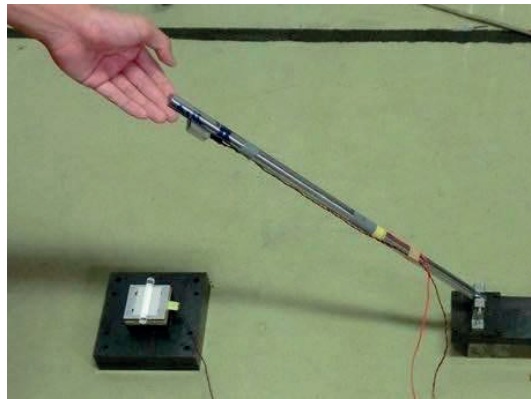


Fig. 3.28 Experiment landscape of 500mm steel shaft

Fig.3.28 shows the photo of the steel shaft just before falling down. Fig.2.28 shows the output waveform of the sensor when the bat hits the resin round bar. Black line indicates upper sensor, the red line indicates lower sensor. In addition, the green line indicates the waveform of strain gauge. In the figure, the upper and the lower sensor's second impact are delayed after the first impact approximately 2.4msec. Peak impact force of lower sensor is greater about 20% lower than the upper sensor's, timing and shape of the shock are in good agreement with each other. Shock time is about 0.4msec at the first time, so is at the second time. In addition, during the first and second impact, the load had made returned back to approximate zero in both the upper and the lower sensor's output.

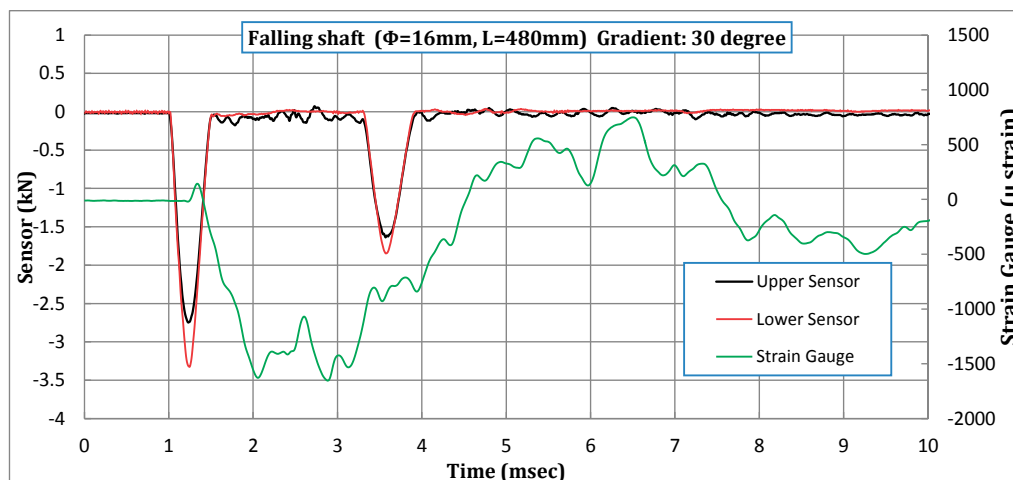


Fig. 3.29 Output waveform in the experiment of 500mm falling shaft

Then focus attention on the strain gauge, the vibration caused by the steel shaft appeared approximately at the beginning of the occurrence of the load peak. This vibration consists of bending vibration of the shaft caused by the rotational inertia of the shaft falling and forced vibration caused tip of steel shaft stricken. Initial stage shows a complex oscillatory waveform, as time went on, gradually become to damped oscillation of bending (oscillation period was approximately 5.2msec although not shown).

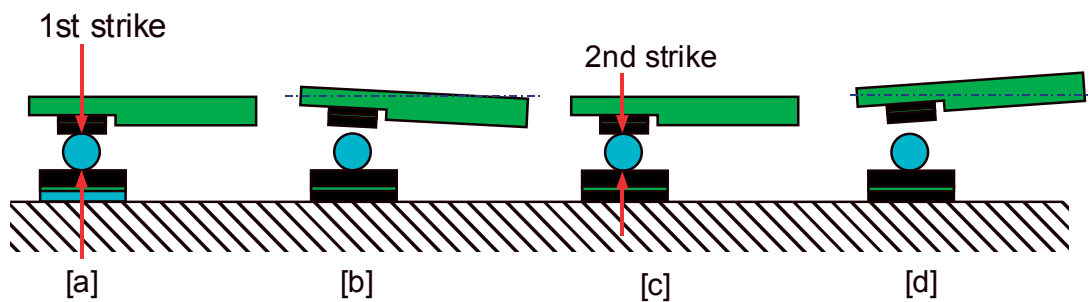


Fig. 3.30 Multi-shock phenomenon between longitudinally turning shaft and fixed plastic stick

Fig.3.30 is a diagram for explaining a phenomenon occurring at the tip of the steel shaft "double-strike". Firstly, there is the first strike of the upper sensor hitting the round resin bar by steel shaft fell down to the horizontal [State a]. The length and quality of steel shaft is predetermined, compared to the speed of the bending vibration is much slower, the vibration appeared approximately at the beginning of the occurrence of the load peak.

At this time, owing to the impulsive force from below the tip of the shaft will bounce up to air [State b]. For this reason, we consider that the upper sensor in state b presents floating position. Afterwards when the first strike finished, the load outputs of upper and lower sensor would both return to zero.

Then steel shaft will return to the initial state from bending state, second strike occurs while returning to the approximately horizontal. In other words, the second strike is that along with the shaft bending back from the upper side to the lower side of the shaft's

central part, the tip of the shaft knocks the resin bar finally [State c]. And we also notice the output of strain gauge is starting to fluctuate from the shaft is bending back the original state. As a result of experiments more than once, in most cases the second strike occurred in the process which the shaft is bending back to the straight state.

Afterwards the tip of shaft can't wait to bend back and will jump significantly [State d]. Passed by 150-200msec, the shaft will fall down again and the tip of shaft will strike the resin round bar. It should be noted that double-strike also occur in the majority of cases that next several strikes happens.

3.2.2.3 400mm Length Steel Bar Drop Test

In order to further confirm our hypothesis, we use a different steel bar whose diameter is 20mm a little thicker than the previous one and length is 400mm a little shorter. Upper sensor, lower sensor and resin bar are used the same as described above. In this experiment, we remove the hinge at the end of the shaft, which is just a simple state placing on the ground (Even so, we still add a rotation stop part to prevent the rolling of the shaft), as shown in Fig3.31.



Fig. 3.31 Rotation stop part of the 400mm shaft

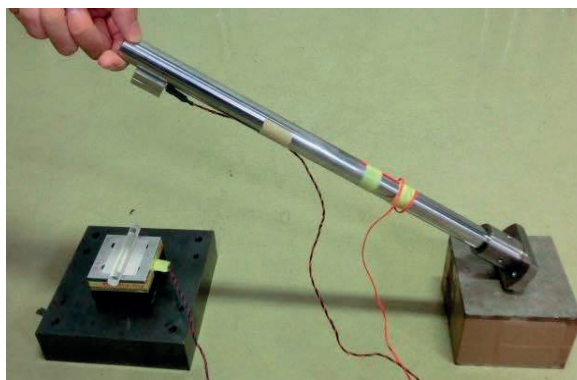


Fig. 3.32 Experiment landscape of 380mm steel shaft

The distance from ground portion of the shaft to the resin bar is 380mm. We lift the tip of the shaft to an angle about 30 degrees from horizon. Fig.3.32 shows the photo of the steel shaft just before falling down. Fig.3.33 shows the output waveform of the sensor when the bat hits the resin round bar.

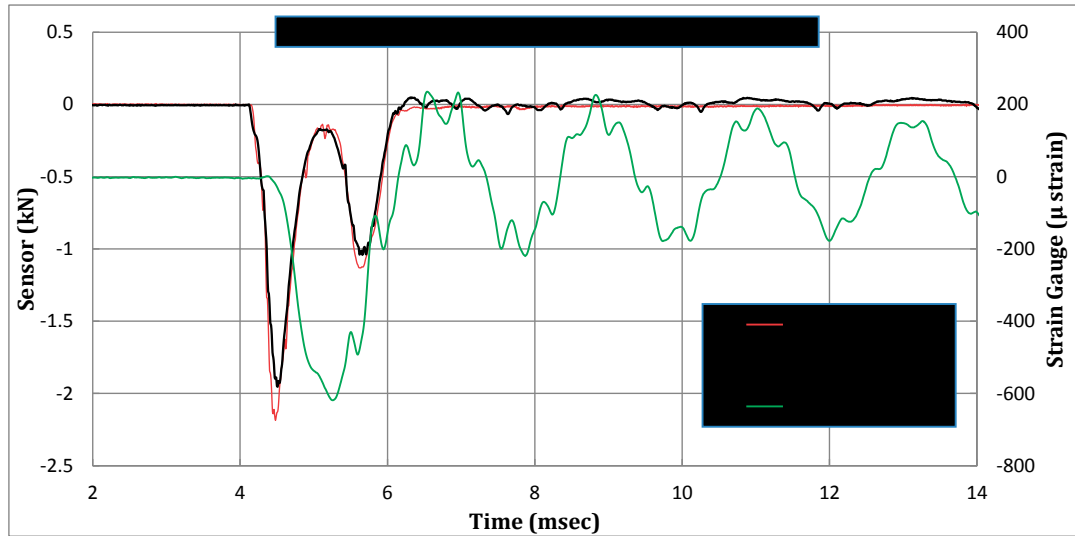


Fig. 3.33 Output waveform in the experiment of 400mm falling shaft

From the Fig.3.33, we realized the shock time is approximately 0.4msec both in the first and second strike, upper and lower sensor will be suffered the second strike when the first strike passed 1msec. In other words, the strike interval is shorter as compared with Fig.3.29.

Subsequently let's check the strain gauge output, the bending vibration is beginning to rise at the vicinity of the peak of the impulsive force's first strike. In this experiment because of the high rigidity of the shaft, the period has shortened to 2msec. After several previous experiments, we have confirmed our pad sensors are effective and precise. Therefore we need to take the sensors to the real situation to measure the impulsive force. We prepare to install the sensors on the baseball bat and measure the impulsive force while the baseball batting.

3.3 Conclusions

In this chapter, three kinds of prototype sensors which are sheet-type impact force sensor, pad sensor and fluctuating load detection plate are developed. Sheet-type sensor has a structure in which silicone rubber sheets are pasted on both surfaces of the piezoelectric film. The pad sensor features light-weighting and high-rigidity in thickness direction, therefore, it is verified that the thin pad sensor can be used to measure the greater extent high-speed impact compared to the conventional load cell. Since the fluctuating load detection plate possesses the metal plates, it can only be used in the plane, but it still can accept impact from hard object. The accuracy of these sensors are demonstrated based on the measurements of the waveform impulse and the momentum theory.

In the metal ball falling tests, through observing the waveform that the metal ball collides the load detection plate, the response performance of the load detection plate against the impact force has been verified.

In the drop test of longitudinally turning bar, steel shaft is a fall from a predetermined inclination angle, it was measured double-strike phenomenon that occurs in a very short period of time when the tip portion hits the resin round bar. And after the collision the shaft tip immediately bounced, bending vibration of the shaft is superimposed, so it is able to measure the waveform of double-strike phenomenon that shaft momentarily hit the resin round bar twice.

References

- [1] Fujimoto, Y., Shintaku, E., Pirker, G. and Tanaka, Y. (2003) Stress Intensity Factor Measurement of Two-Dimensional Cracks by the Use of Piezoelectric Sensor, *JSME Int. J.*, A46-4, 567-574.
- [2] Franc, J.P., Riondet, M, Karimi, A. and Chahine, G.L. (2001) Impact Load Measurements in an Erosive Cavitating Flow, *J. Fluids Eng, Trans. ASME*, 133/121301, 1-8.
- [3] Cherung, G. J. and Peng, S.L. (1994) Transient Multiple Impulsive Signal Analysis for Pneumatic Percussive Rivet Tools, *Mechanical Systems and Signal Processing*, 8-1, 31-44.
- [4] Whittle, M. W. (1999) Generation and Attenuation of Transient Impulsive Forces Beneath the Foot: a review *Gait and Posture*, 10-3, 264–275.
- [5] Matsushita, S., Matsui, K. and Sakata, T. (1996) Dynamic Response of Clamped Rectangular Plates Impulsed by a Steel Ball, *Trans. JSME*, C62-602, 226-232.
- [6] Trethewey, M.W. and Cafeo, J.A. (1992) Signal Processing Aspects of Structural Impact Testing, *Int. J. Analysis and Experimental Modal Analysis*, 7-2, 129-149.
- [7] Fujimoto, Y., Shintaku, E., Tanaka, Y. and Fujiyoshi, J. (2012) Pad Type Compressive Force Sensor Suitable for High-speed Impact Force Measurement, *Trans. JSME*, C78-791, 2438-2449.

Chapter 4 Applications of Pad Sensor Installed onto the Baseball Bat

In situations like the baseball bat struck by a ball, or the utility pole or a road sign pole crashed by a car, or the person's body hit by a falling pipe material, this kind of impact phenomenon associated with pipe materials is regularly seen. Because of the curved surface, the pipe's distribution of impact pressure differs from the plane. Bending rigidity, vibration characteristics, even deformation of the circular cross section affect the impact force. Since the sensor element that can be used for the curved surface is in the minority, if directly measuring the impact force on the pipe surface becomes possible, it is useful for the elucidation of the phenomenon.

In this study, pad sensor that can be used on bending out-of-plane is regarded as the sensor element, baseball bats and pipes in the roughly same size are regarded as the experimental subjects, the impact force which is generated by the ball colliding with the pipe is aimed to be measured, a pipe-surface-mounted sensor intent to be investigated. The previous research regarding the impact force of a baseball bat includes the following experiments: an experiment which measures the phenomenon of a shooting ball from a gas gun hitting a baseball bat [1]; an experiment in which a swing bat is fastened and hits the balls shot from a pitching machine [2]; and an experiment which measures the coefficient of restitution during the hitting period utilizing an equipment which can change the clamping method of a baseball bat [3]. In addition, there are examples in which to calculate the impact force or collision phenomena of the bat by numerical analysis [4] [5]. However, actually installed the sensor on the baseball bat, measuring the impact force while hitting back the pitched ball is not found.

This study is aimed to explore the requirements of pipe surface-mounted flat-panel sensor, which are the contact friction effect to the ball and the sensor and the means for its removal, how to ensure the impact load bearing capacity, and the installation method of the sensor onto the pipe. In addition, producing a prototype sensor, ball drop test and the weight drop test for detecting its performance, and the striking baseball test by mounting the sensor onto metal bat are all conducted.

4.1 Experiments Conditions and the Design of the Experiment Devices

The contact time when the hard ball hit the bat is about 1msec, and impact force at the time of the swipe it is said that more than 10kN. Therefore, the strength of the sensor should be able to withstand this level of high-speed large load. Fig.4.1 shows the pad sensor we used in this experiment; its size is 84x144mm. In order to make it easy to attach to the baseball bat of which surface is column, the sensor has been made in flat and thin.

The following sections describe how to get the pad sensor signal. The cable that pulls out from the sensor is connected to the voltage recorder directly; And the voltage which is proportional to the time derivative dW/dt (Loading speed) of the compressive load W is measured. In this study, we use a cable with circuit capacitance of $1\mu\text{F}$, and connect to high-speed voltage recorder (NECAvio-RA2300) which is set at the sampling rate $50\mu\text{sec}$.

After production completed, the thin pad which is sandwiched by two metal sheets carried out on a 9 steps of 2Hz block load of which the average is -30kN applied by the hydraulic servo testing machine, Fig.4.2 shows the waveforms of the sensor output and load testing machine, from the figure sensor output waveforms are in good agreement

with the testing machine load.



Fig. 4.1 Example of pad sensor

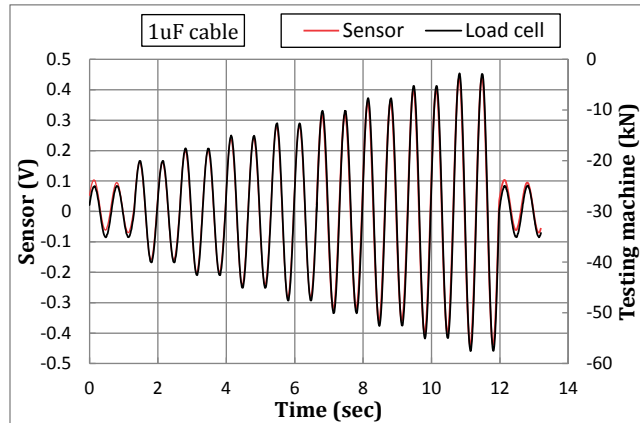


Fig. 4.2 Sensor output vs. load cell output under block load

4.2 Installation of the Sensor to the Surface of the Pipe

Before we install our sensor on the real baseball bat, we want to test it on a metal column, so we design this experiment. Fig.4.3 (a) shows the procedure to install the sensor onto the pipe. Since we can't adhere and peel off the sensor to the pipe surface, in this study we use an arc-shaped cover plate (0.5mm thick aluminum plate) to cover our sensor. Cover plate is made into a predetermined curvature by bending roller, then connect the ground wire with the pipe. The ground wire is aimed to remove drift caused by the static electricity of the collision body when collision body charged hit the sensor.

Fig.4.3 (b) shows the photo the fastening method in which how to fix the pipe sensor and the cover plate. In this study we try to use aluminum adhesive tape (0.13mm total thickness) to wrap around the pipe. Figure shows the thick aluminum pipe whose diameter

is 65mm fixed.

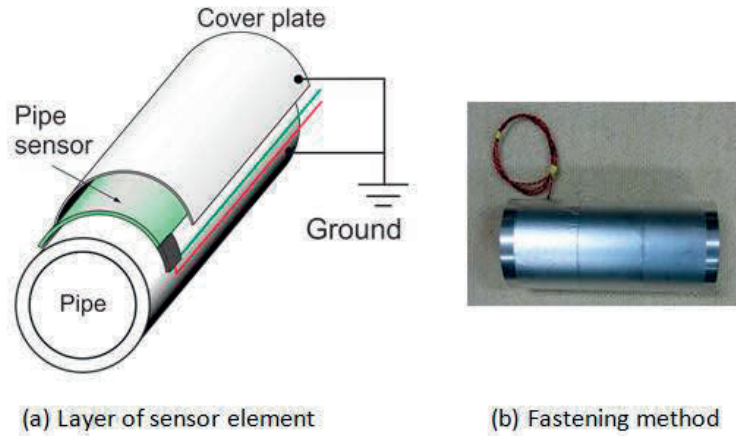


Fig. 4.3 Set of sensor to the pipe surface

4.3 Baseball Falling test on the Column Sensor

Fig.4.4 shows baseball falling experiments on the pipe wrapped in pad sensor. The pipe wrapped in sensor has been placed on two V-block, hard ball, soft ball and rubber ball these three kinds of ball is made a free-fall from 2m height respectively through the PVC pipe. The mass of hard ball is 0.149kg, softball is 0.192kg, rubber ball is 0.138kg. Sensor is connected to a high-speed voltage recorder (Omni ace RA2300) via a 1 μ F cable; output waveforms were recorded at the sampling rate in 50 μ sec.

Fig.4.5 shows some waveform examples of the impulsive force when the ball hits the column wrapped in sensor. The peak of hard ball impulsive force is about 1.8kN in about 1.65msec. The peak of soft ball impulsive force is about 1.35kN in about 2.4msec. In addition, the peak of rubber ball impulsive force is about 0.4kN in about 5.7msec.

It should be noted that the impact force of rubber ball are bent from a steep rise to a gradual slope in the course. Bending is considered that caused by the strain rate dependence of the polymeric material [6], in the case of rubber ball, it is considered that after the hollow ball is collided rubber elasticity immediately migrate to crush deformation, meanwhile the spring constant of ball changes. It also occurs in tennis or basketball, but does not occur in cases of balls of which central portion is tamped such as hard ball, golf ball and bowling ball.



Fig. 4.4 Ball falling test on the column sensor

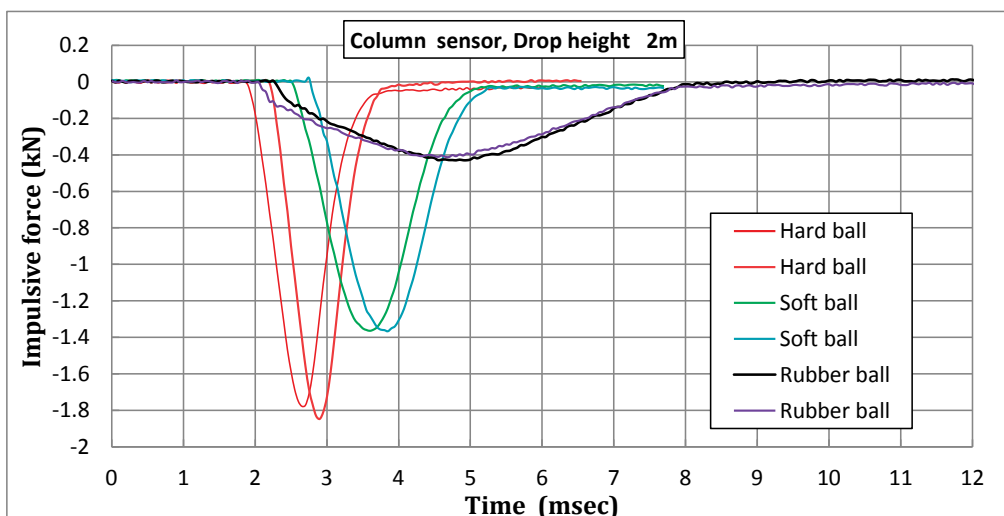


Fig. 4.5 Impulsive force by the falling of three kind of ball onto column sensor

Table 4.1 shows comparison between impulse which is determined by numerical integration of the area of the impulsive force waveform and changed momentum considering the bounce back of the ball before and after collision. As it is shown in the table, these two kinds of values are in good agreement. To sum it up, using a sensor wrapping around column, the waveform of baseball low-speed collision impulsive force can be measured well.

Table 4.1 Momentum and impulse at the baseball ball falling

	Mass m (kg)	V (m/sec)	e	$mV(1+e)$ (N·sec)	Impulse (N·sec)	Shock time (msec)
Hard ball	0.149	6.26	0.53	1.43	1.42	1.65
Soft ball	0.192	6.26	0.64	1.97	1.80	2.40
Rubber ball	0.138	6.26	0.81	1.56	1.50	5.70

e : Coefficient of restitution

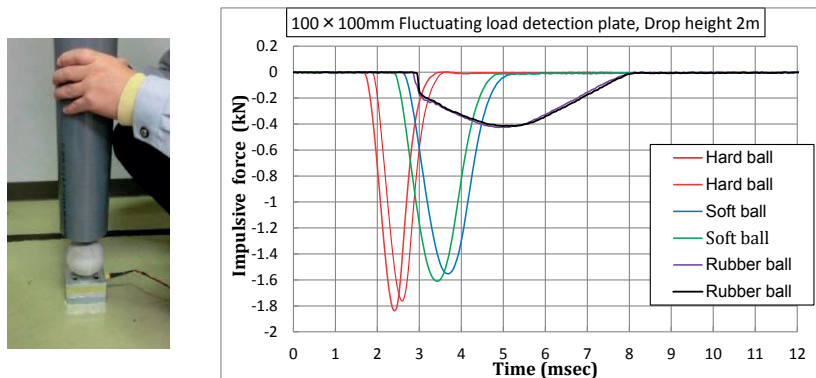


Fig. 4.6 Impulsive force by the falling of three kinds of baseball onto fluctuating load detection plate

In Fig.4.6, 3 kinds of balls are dropped from the height $h=2\text{m}$ through a PVC pipe onto a 100mm square of fluctuating load detection plate placed on the floor, two cases of impact force waveforms are shown. Although waveform in Fig.4.6 is similar to the waveform of the pipe sensor shown in Fig.4.5, the impact time of rubber ball is a little shorter than that of pipe sensor. In addition, the peak impact force of softball is larger about 10%. Although there are these differences, it is considered that it can measure the impact force waveform of low-speed collision of baseball ball by using the pipe sensor.

It should be noted that, since it is bent in rising part of waveform of rubber ball by load detection plate, the bent is thought to be due to the characteristics of the rubber ball.

4.4 Hitting Experiment of Baseball Bat with Pad Sensor

Fig.4.7 shows the aluminum metal bat for hardball (0.91kg mass, 0.83m length, 67mm outside diameter), and attaching the pipe sensor (sensor body, adhesive tape and aluminum cover plate) and a photo of the bat after wrapped in sensor. The sensor body mass is 0.028kg, cover plate is 0.029kg and adhesive tape is about 7g; the total weight is 0.0064kg, about 6.8% of the total mass of the bat. The sensor cable and ground wire are pulled out to the end of the bat, and wrapped in vinyl tape on the way, and the voltage recorder is connected via an approximately 10m long cables (1 μ F capacitance). And the right photo in Fig.4.7 shows that it is possible to swing the bat without the interference of the cable.



Fig.4.7 Baseball bat before and after the setting of pipe sensor

Fig.4.8 shows a state and its impact force waveform example of a batting tee with a hard ball. By an amateur students, the peak of the impact force is about 3 ~ 4kN. The contact time is 1.2 ~ 1.5msec. The contact time is a little shorter than about 1.65msec when hard ball drops on the pipe in figure 20. In addition, about 2Hz residual vibration occurs with small amplitude.

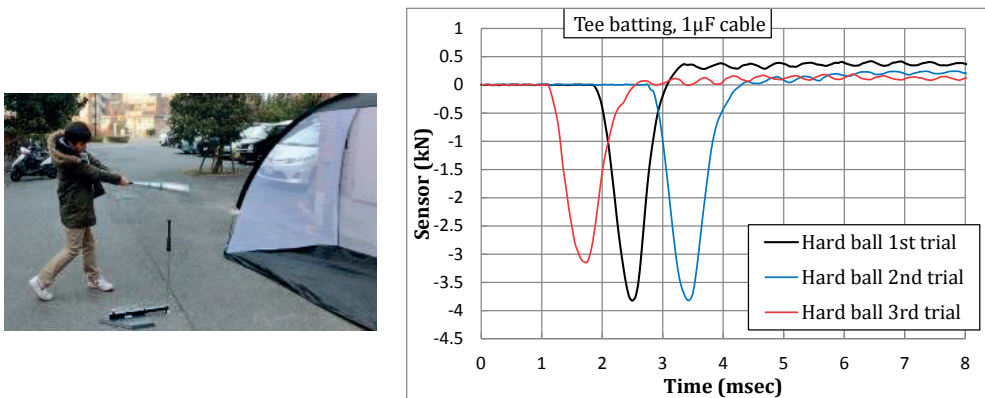


Fig. 4.8 Tee batting and the measured impulsive force waveform

Fig.4.9 shows we ask a student to help to do the experiment, one as pitcher, one as batter, the right figure shows the waveform of the impulsive force when the baseball hit the bat. Peak impulsive force of the hit is about 9kN, shock time is about 0.9msec. Compared with the baseball falling test, the shock time in hit experiment is a little shorter than 1.65msec; we consider that as impact speed is faster, the shock time become shorter is normal.

But in the bunting occasion, the peak of impulsive force become 3.5kN, shock time become about 1.2~1.5msec. In the bunting occasion there is a drawing bat behavior done by the batter, which is considered as the main reason of the waveform is approximately symmetrical.

By the way, the residual vibration of about 2kHz frequency has occurred in hit waveform of hardball. According to the measurement result of the strain gauge was

attached to the inner and outer surfaces of the circular ring of the bat detected by Tanaka et al. [1], the vibration is the main primary vibration of circular ring where the hit point is regarded as the vibration center, of which frequency is about 2kHz. On the other hand, about the natural frequency of the bending vibration in the longitudinal direction of the bat, primary mode is 200 ~ 230Hz, secondary mode is 700 ~ 800Hz, both are slower. From this fact, residual vibration is considered to have measured the flexural vibration of the ring.

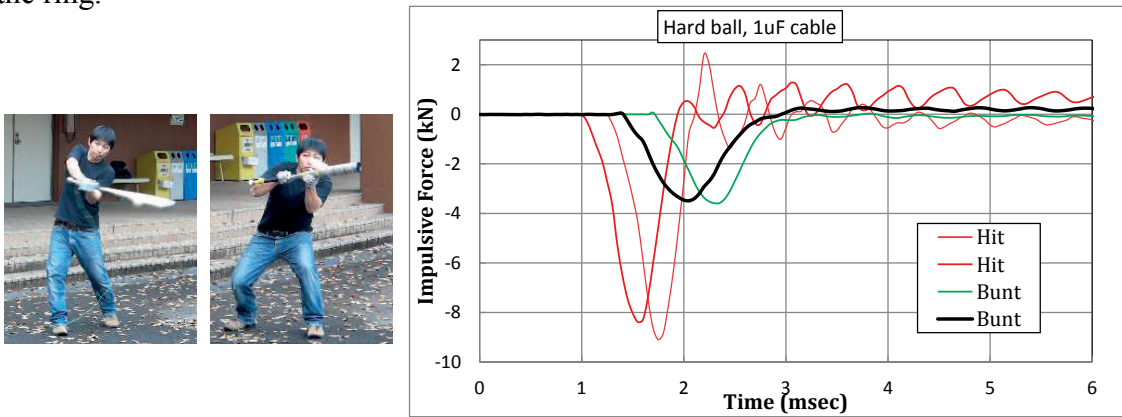


Fig. 4.9 Impulsive force of hit and bunt of hard ball

4.5 Conclusions

This study is carried out experimental studies on the pipe surface-mounted sensor for impact force measurement. The aim is to select a pipe whose dimensions is close to pipe baseball bat and to measure the impact force when hit and bunt the baseball. The detection element is a piezoelectric film, and a thin detachable pad sensor which is able to installed onto the pipe and don't require any processing is developed and is able to carry out the experiment, the performance and problems of sensor are revealed. The results obtained are as follows.

1. A proposed configuration of a thin pipe sensor that can be installed on the pipe surface with about load-bearing capacity of 10kN has been submitted.

2. The impact force waveforms which are obtained when hard ball, soft ball and rubber is dropped from 2m height on pipe sensor have been measured, the momentum change (Momentum) before and after collision and waveform impulse (Impulse) have been confirmed nearly match.

3. The impact force waveform when hard ball thrown by pitcher is hit or bunt has been measured by installing the pipe sensor on the metal bat.

4. In the method of fixing the sensor and the cover plate to the pipe using an aluminum adhesive tape, Variation of about $\pm 10\%$ occurs in the slope of output the sensor by fastening method. It is needed to improve the method of fixing the sensor in the future.

References

- [1] Tanaka, K., Masuda, T. and Kodama, H. (1992) High-Speed Impact of Baseball Bats and Balls (1st Report, Impact of Aluminum Alloy Bats and Balls), Transactions of the Japan Society of Mechanical Engineers. A 58(556), 2365-2369.
- [2] Shenoy, M.M., Smith, V.L. and Axtell, T.J. (2001) Performance Assessment of Wood, Metal and Composite Baseball Bats, Composite Structures, 52, 3–4, 397–404.
- [3] Kagawa, H., Yoneyama, T., Nasu, H., Igarashi, S., Kitagawa, Y., Takahashi, M. and Sato, K. (2011) Development of the Evaluating System on Hitting Performance and Choice of Clamping Methods for Baseball Bats, Transactions of The Japan Society of Mechanical Engineers, A 77(783), 4218-4227.
- [4] Kanda, Y. and Naruo, T. (2007) Simulation of Impact between Rubber-ball and Bat for Baseball (Mechanical Systems), Transactions of the Japan Society of Mechanical Engineers. C 73(729), 1307-1313.
- [5] Russell, A. D. (2006) Bending Modes, Damping, and the Sensation of Sting in Baseball Bats, Engineering of Sport, Proc. 6th Int. Sports Engineering Conference.
- [6] Hongo, T., Sato, H., Iwata, Y., Komatsuzaki, T. and Hongo, Y. (1999) Modeling and Analysis of Impact System Composed of Ball and Plane, Transactions of the Japan Society of Mechanical Engineers. C 65(634), 2287-2293.

Chapter 5 Flexible Sensor for the Impact Force Measurement in Flexible Interface

When a boxer punches the human body, both body surface and boxing glove deform in a complex shape. At present, the accurate measurement of impact force in such interface is said to be difficult. The reason is because the complex deformation and the complex force distribution are induced in the flexible interface and they affect the sensor output. Up to now, many kinds of tactile sensors such as resistance type, piezo-resistance type, capacitance type and light intensity type have been developed. Most of them are assuming to mount the sensor on the robot members. However, it has not been studied much about the influences of the deformation and the associated force distribution at the flexible interface on the accuracy of the sensor output. The reason of this is most of the tactile sensors are intended to use under a small force level and a small deformation level on the installation surface.

By the way, it has been reported that peak impact force of about 4 kN is generated when a strong boxer punches the face of crash test dummy. When the hitting target is sandbag, the interface of glove and sandbag will be deformed more greatly. A suitable sensor which can measure the impact force in such condition is not seen at present. The purpose of this study is to provide a sensor that can measure the impact force accurately at the interface of large deformation and large force.

In this study, firstly, difficulty of force measurement in flexible interface is discussed based on the experiments using a sheet type sensor (section 5.1). Then, some mechanical factors necessary to achieve the flexible sensor are discussed (section 5.2). These factors are the out-of-plane bending deformation of sensor, the shear force caused by rubbing on

sensor surface, the shear force generated by contact friction, and the transverse compression caused by the overhanging deformation of the flexible material.

In Section 5.3, as a sensor that can overcome the mechanical problems in flexible interface, a flexible sensor of distribution type is developed. In section 5.4, boxing punching tests are carried out using a prototype sensor by installing the sensor on the sponge rubber sheet which is placed on the load cell or the concrete wall. Further, the punching test is carried out by installing the sensor on a sandbag. In particular, the present study is focused to achieve a sensor structure that is hard to cause trouble under a big impact force like boxing punching.

5.1 Measurement of Force on Soft Material Surface by Using a Sheet-Type Sensor

5.1.1 Spherical Surface Pressing on the Flexible Material Surface

As a simple case, spherical pressing experiment of a sensor installed on the flexible material surface was carried out. Fig.5.1(a) shows a sheet type sensor made from piezoelectric film (PVDF) of which both surfaces are covered by silicon rubber sheets [8]. When compressive force F is applied as shown in Fig.5.1(b), the rubber sheets shrink in the thickness direction and also be extended in the horizontal direction by the Poisson's effect. Since the elastic modulus of PVDF is much larger than that of rubber sheet, the PVDF is stretched by the rubber elongation in the horizontal direction. Then, the output signal proportional to the compressive force F is generated in the sensor.

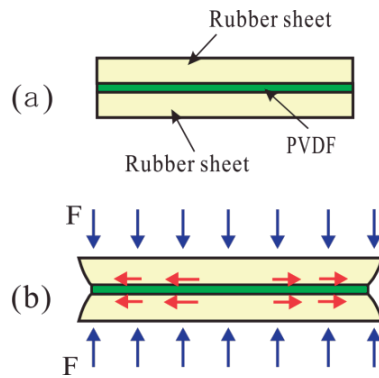


Fig. 5.1 Sensor cross-section and its detection principle of compressive force

Fig.5.2(a) shows a sheet type flexible sensor with slit notches around the sensor edge. A single sheet type sensor is not possible to follow the out-of-plane deformation. In order to make out-of-plane deformation possible, one way is to process the slit notches around the sensor edge. The slit notches are expected to get a similar result with “preventing wrinkles of thin paper to wrap an apple”.

Fig.5.2(b) is the sensor covered by doubly stretch cloth on both surfaces. A polyethylene sheet is sandwiched in between the doubly stretch cloth. When the sensor with slit notches is directly placed on the flexible-material and pressed by curved surface object, the output signal of the sensor is influenced by the contact friction between the sensor and the contact object. The stretch cloth and the polyethylene sheet play a role to reduce the influence of contact friction by slide effect.

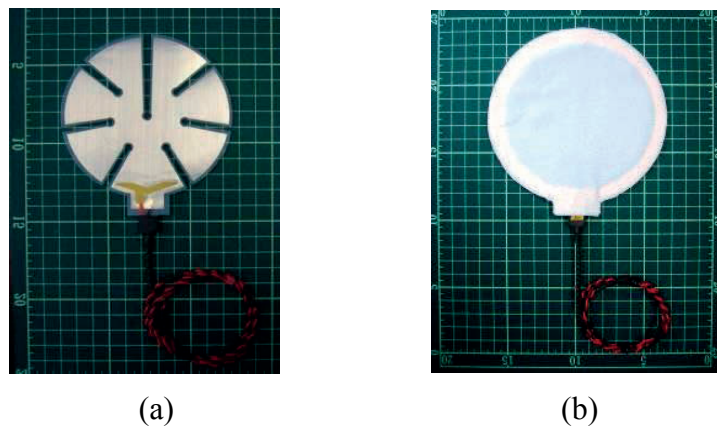


Fig. 5.2 Sheet type flexible sensor. (a) Main body of sensor with slits in outer edges. (b) Sensor covered by stretch cloth

Fig.5.3 shows the condition of compression test. Thick acryl plate was fixed on the top of a load cell. Sponge rubber plate with 40 mm thickness was placed on the acryl plate. The sensor was put on it and pressed by spherical body with 50, 100 or 150 mm diameter. The experiment was carried out by changing the compressive force.

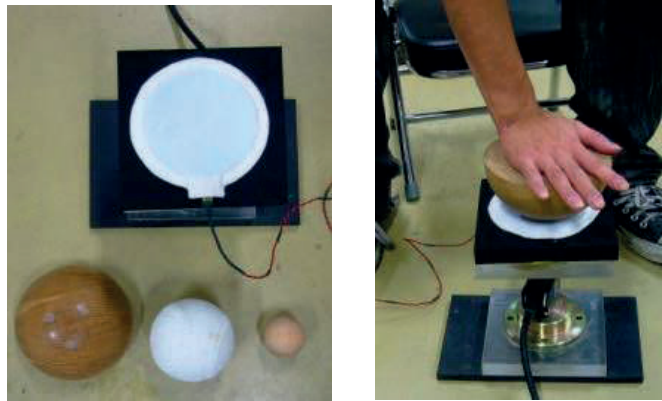


Fig. 5.3 Spherical press of the sensor on the sponge rubber

Fig.5.4 compares the relationship between the peak force of the load cell and the sensor output. A good linear relationship is seen in the figure. Despite the change in the diameter of spherical body, the output gradient does not change much. The dashed line in the figure shows the output gradient under the condition that the sensor is placed directly on the flat acryl plate. The sensor detects the normal force on the curved surface, but the load cell detects the vertical component. The difference in gradient of the two straight lines is considered to be related with the detection characteristics.

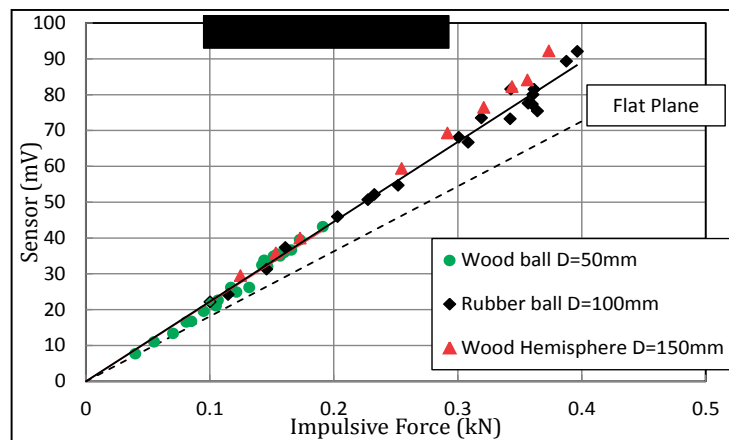


Fig. 5.4 Sensor output vs. load cell output. Dashed line is the output gradient of the sensor on flat plane surface.

5.1.2 Fist Pressing, Palm Pressing and Fist Punching on the Surface of Flexible Material

Next experiment was carried out under the condition that the contact interface deforms in a complex shape. Fig.5.5 shows the conditions of fist pressing, palm pressing and fist punching. The experiments were conducted by changing the compressive force. Fig.5.6 shows the relationship between the peak force of the load cell and the peak output of the sensor during compression. A quite large scatter of plots is seen in the figure.



Fig. 5.5 Fist press, palm press and fist punch of the sensor placed on the sponge rubber plate

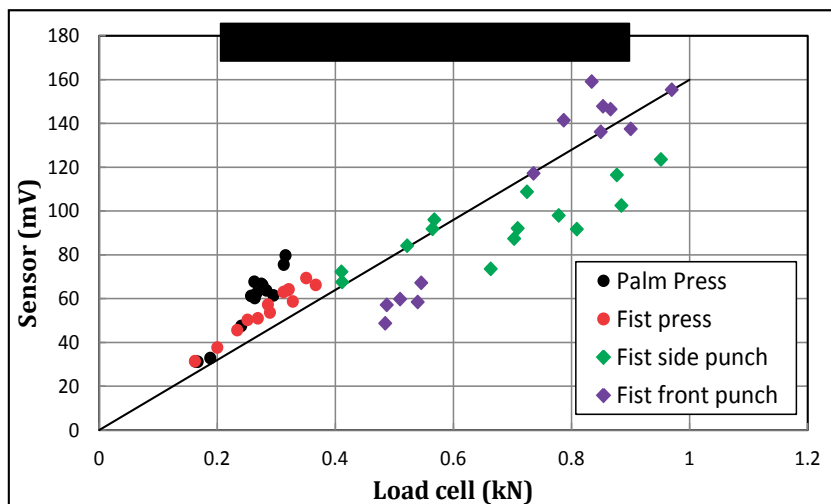


Fig. 5.6 Relationship between the output peak of sensor and the peak force of load cell

In the experiment of Section 5.1.2, the loading side was a hard material with simple contact surface and the receiving side was a flexible material. On the other hand, the contact surface of fist or palm is more complex and it changes in every trial. Further, rubbing force and inclined force are also working. The cause of the scatter of the output gradient can be considered as the influences of complex force distribution and the excessive out-of-plane deformation occurring in the sensor. This result means that a single sheet-type sensor is not suitable to achieve the measurement of impact force on the flexible material surface.

Fig.5.7 classifies the condition of impact force measurement into four levels, in view of the difficulties of measurement. Fig.5.7(a) is the condition that a hard object with simple contact geometry collides. Fig.5.7(b) is the condition that a soft object with simple contact geometry collides. In accordance with the deformation of soft object, in this condition, unexpected shear forces (rubbing force and contact friction) work at the interface. Fig.5.7(c) is the condition that a hard object with complex contact geometry collides. In this case, the out-of-plane bending deformation of the sensor and the distributions of shear forces at the interface become more complex. Fig.5.7(d) is the condition that a soft object with complex contact geometry collides. In this case, stress distribution and deformation becomes most complicated. Boxing punching on sandbag surface is close to the condition of Fig.5.7(d).

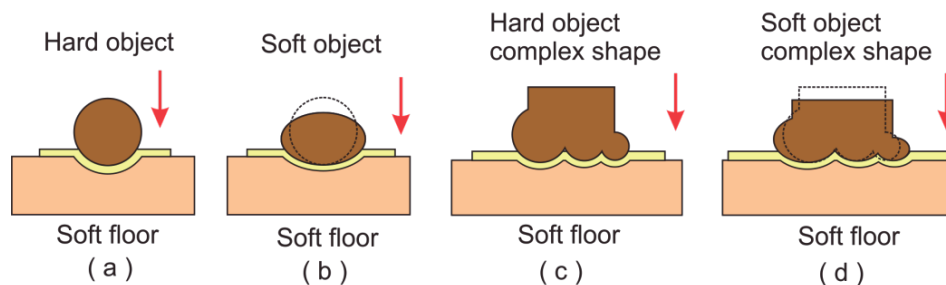


Fig. 5.7 Difficulty of force measurement at flexible interface is classified into four levels depending on the shape of the impact object. (a) Hard object with simple contact geometry, (b) Soft object with simple contact geometry, (c) Hard object with complex contact geometry, (d) Soft object with complex contact geometry

5.2 Mechanical Issues in Impact Force Measurement on Flexible Material Surface

The objective of this research is to develop a sensor which can be used even when both objects of loading side and load receiving side are soft and the contact geometry is complicated. After repeating several experiments, the authors realized that the discussions about the error signals are necessary for the flexible sensor. They will be described in the following.

5.2.1 Influence of Out-of-Plane Bending Deformation of the Sensor Element

Fig.5.8 shows a sensor element used in the flexible sensor. A pair of silicon rubber sheet is adhered on the both surfaces of piezoelectric film (PVDF). The bending neutral axis comes to the center of PVDF thickness, theoretically, due to the vertically symmetric structure. Therefore, the sensor output should not occur almost by bending deformation. However, in practice, by variation in the thickness of the adhesive layer and etc., the neutral axis is shifted slightly from the center of PVDF thickness [9]. Thus result in the occurrence of tensile or compressive strain in PVDF (Fig.5.8(b)). If a resin sheet like a flexible substrate is adhered on one side surface of the silicon rubber, the bending neutral axis is further shifted, and results in greater strain (Fig.5.8(c)). It is extremely difficult to control the strain of PVDF caused by bending deformation.

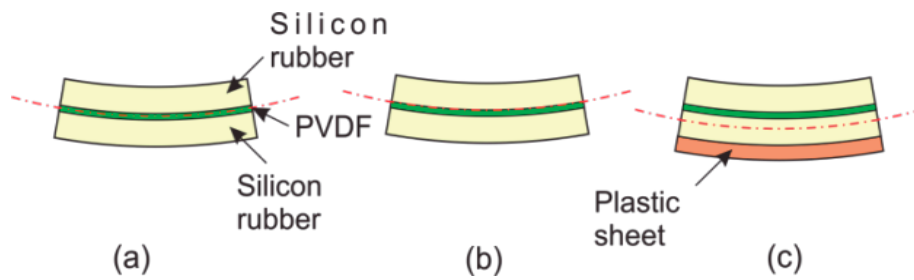


Fig. 5.8 Error signal caused by the out-of-plane bending deformation of sensor element. (b) and (c) represent the shift of the neutral axis by bending deformation

5.2.2 Influence of Rubbing Force on the Sensor Surface (Shear Force Caused by Rubbing)

Fig.5.9 shows a schematic view of a sensor element placed on the floor, on which a compressive force F on the left side and a rubbing force S on the right side are acting. The vertical reaction force R_F occurs below the F , and the shear force R_S against S occurs caused by the friction between floor and sensor element. As the result, tensile strain is produced in the region between the points F and S (shown by red arrow). The rubbing force S sometimes is generated as the horizontal component of inclined force which is applied to the sensor surface.

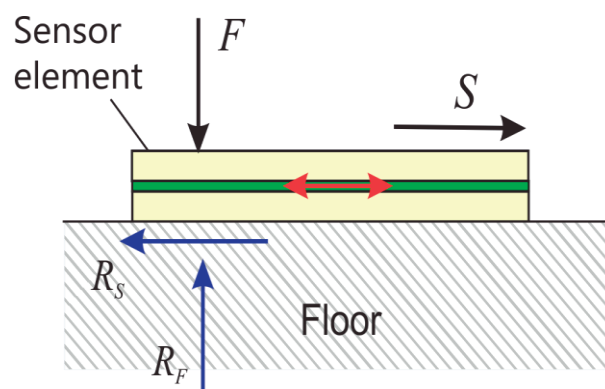


Fig. 5.9 Example of the tensile strain (red arrow) generated in the sensor element caused by rubbing force. F is compressive force, S is rubbing force and R_F and R_S are the corresponding reaction forces

5.2.3 Influence of Contact Friction on the Sensor Surface (Shear Force Caused by the Poisson's Effect)

Fig.5.10(a) shows a sensor element sandwiched in between the metal plates. Since the elastic modulus of silicon rubber is smaller than those of PVDF and aluminum plate, the silicon rubber deforms into barrel-shape when compressive force F acts.

Fig.5.10(b) shows a state in which a pair of sponge rubber sheet is sandwiched between the silicon rubber and aluminum plate additionally and applied a compressive force F . Since the elastic modulus of sponge rubber is further smaller than that of silicon rubber, the sponge rubber deforms into bigger barrel-shape. Even if the same F is applied, the silicon rubber is stretched more in this condition. This means that the sensor output is affected by the Young's modulus of the contact material as well as its thickness.

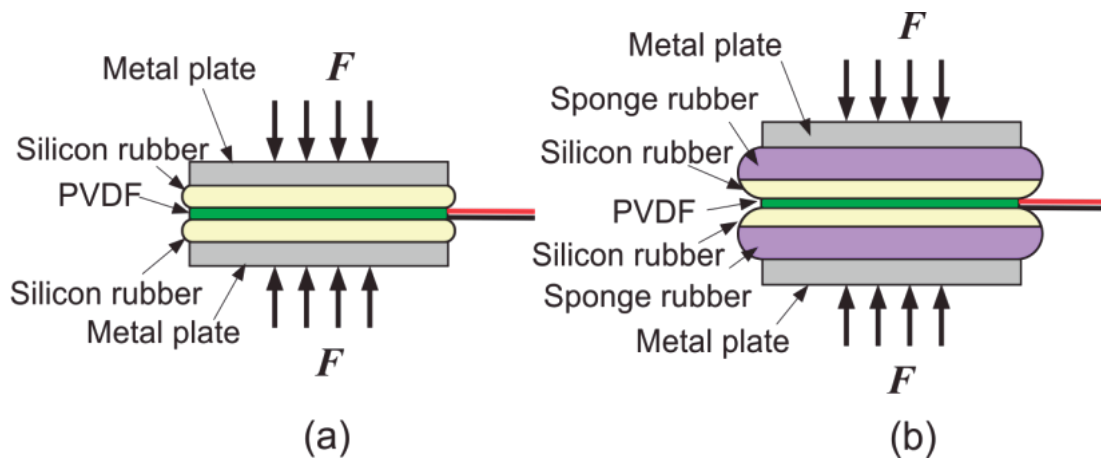


Fig. 5.10 Error signal caused by the difference of contact friction

As an example, Fig.5.11 shows the magnitude of sensor output in accordance with the change of contact material. The output is adjusted as 1.0 when the sensor element is sandwiched directly between the aluminum plates. A circular sensor element with 50 mm

diameter is used. The silicon rubber on both sides of PVDF is 1 mm thickness. Sponge rubber sheet ($T = 5$ mm, 10 mm thick) or natural rubber sheet ($T = 1$ mm) or cork plate ($T = 2$ mm) was sandwiched between the sensor element and the aluminum plate. As the contact material becomes softer, the sensor output increases as shown in the figure. In the case of thick sponge rubber ($T = 10$ mm), the magnitude becomes several times compared with the case of the aluminum plate.

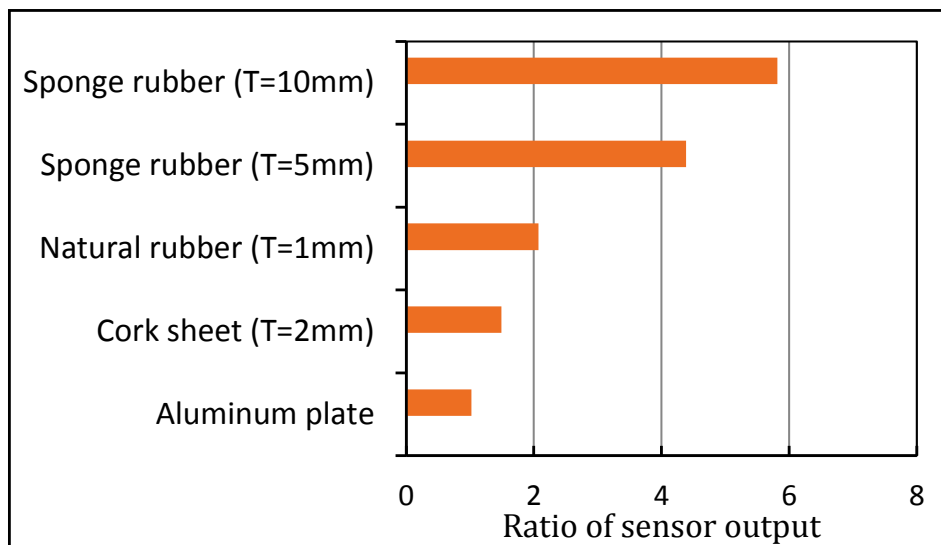


Fig. 5.11 Variability of sensor signal caused by the difference of contact material

5.2.4 Influence of Lateral Compression Caused by the Overhanging Deformation of Flexible Material

Fig.5.12 shows the state that a soft material in large size enough to cover the sensor element collides with the element. When the force F acts on the sensor surface, impact force (solid curve) in compressive direction is produced as shown in Fig.5.12(a) at first. However, by the succeeding deformation of soft material, a part exceeding the area of the sensor element may press the element from the lateral direction. By the transverse

compressive force from the surrounding, the sensor generates a signal in opposite direction as shown by dashed curve of Fig.5.12(b). As a result, the sensor signal becomes the sum of solid and dashed curve as shown in Fig.5.12(c).

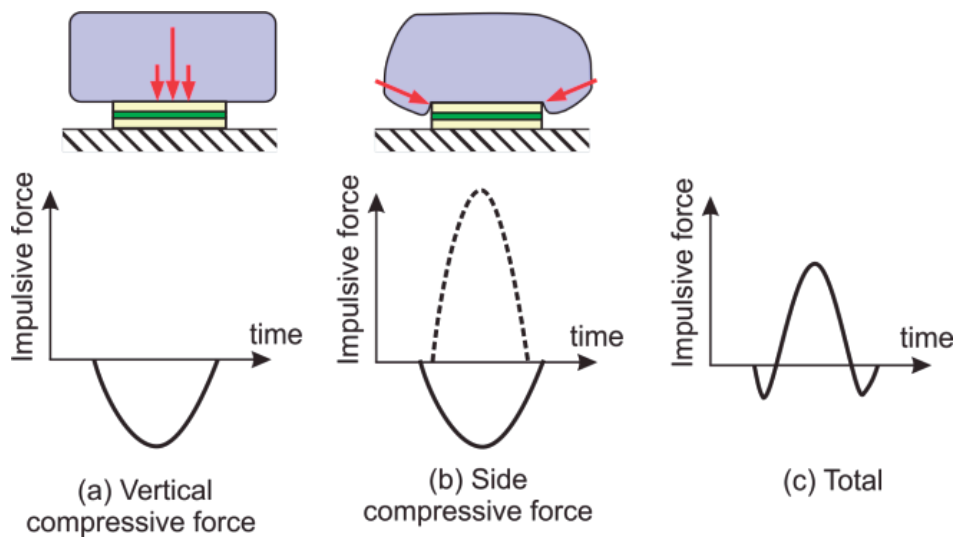


Fig. 5.12 Lateral compression phenomenon caused by the overhanging deformation of flexible material

Fig.5.13 shows an example of such waveforms by the free drop test of soccer ball. A circular sensor element with 50 mm diameter was placed on the load cell, and the ball was fallen onto the sensor. Fig.5.13 compares the sensor output (red curve) and the load cell output (black curve). When bottom of the ball collide the center of sensor, the sensor output is generated on the negative side. After that, it turns into the opposite side in the halfway, since the overhanging part of deformed ball presses the sensor laterally. Therefore, the sensor waveform becomes quite different from the load cell waveform. Such lateral compression occurs as well when the sensor bottom is in buried condition in soft material.

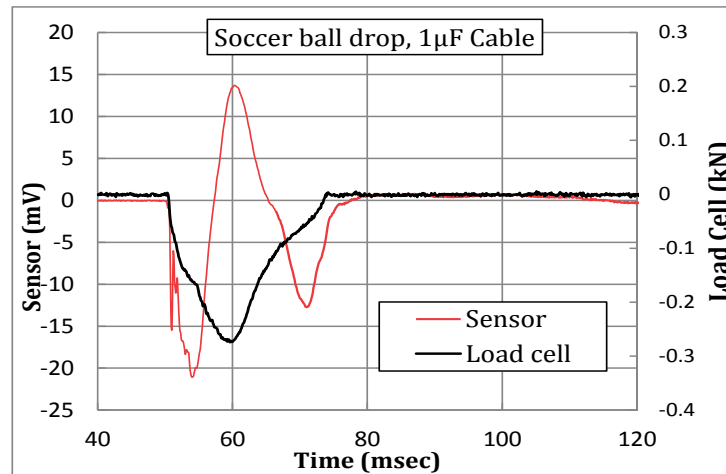


Fig. 5.13 Impact force waveform in which vertical and lateral compression is mixed

5.3 Flexible Sensor Made from Plural Sensor Elements Arranged in a Matrix

In order to eliminate the above influences, in this study, we develop a sensor element of rigid plate type. The sensor elements are distributed in a matrix, and the seam portion of each sensor element is connected flexibly in order to ensure the flexibility. Further, a new manner to acquire the sensor signal without using electrical wiring is employed.

5.3.1 Prototype of sensor element

Fig.5.14 shows the sensor element with 30mm square and the twenty elements made for this research. At first, silicon rubber sheet with 1mm thickness was adhered on both surfaces of PVDF. Next, a circular hole was drilled in the center of the silicon rubber, and the hole was filled with conductive rubber. The conductive rubber was designed to contact the electrode of PVDF. Furthermore, aluminum plate was adhered on the silicon rubber

on each side. The upside and downside electrode of PVDF are connected with the upper and lower aluminum plate respectively via conductive rubber. In order to assure the electric contact between the PVDF and the aluminum plate, the conductive rubber was pressed by screw. The reason of using 5mm thick aluminum plate is that metal plate with certain thickness is necessary in order to prevent the bending deformation.

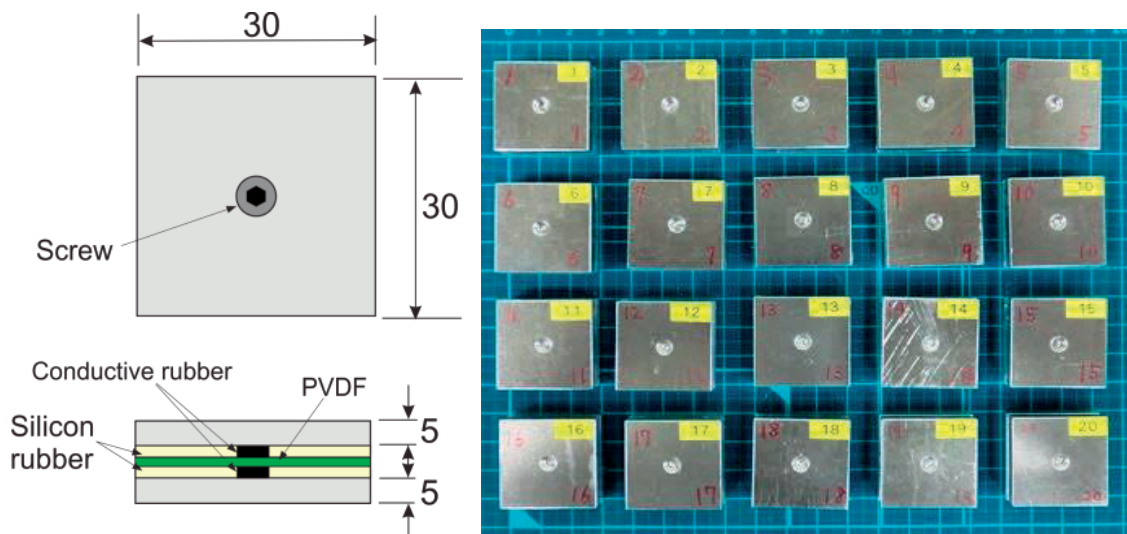


Fig. 5.14 Configuration of the prototype sensor elements

Each sensor element was placed on load cell and punched by hand hammer (with felt cap) several times. Fig.5.15 shows examples of the impact force waveforms. Solid curve is the sensor output and dashed curve is the load cell output. Eventually, sixteen elements among them were selected and used for the flexible sensor.

Fig.5.16 shows the output gradient of the chosen sensor elements. The horizontal axis is the peak impact force obtained by load cell and the vertical axis is the peak output of the sensor element. As shown in the figure, load-bearing capacity of a single sensor element is more than 1.5 kN. If the impact force is distributed to several sensor elements, then the load bearing capacity is more than 10 kN.

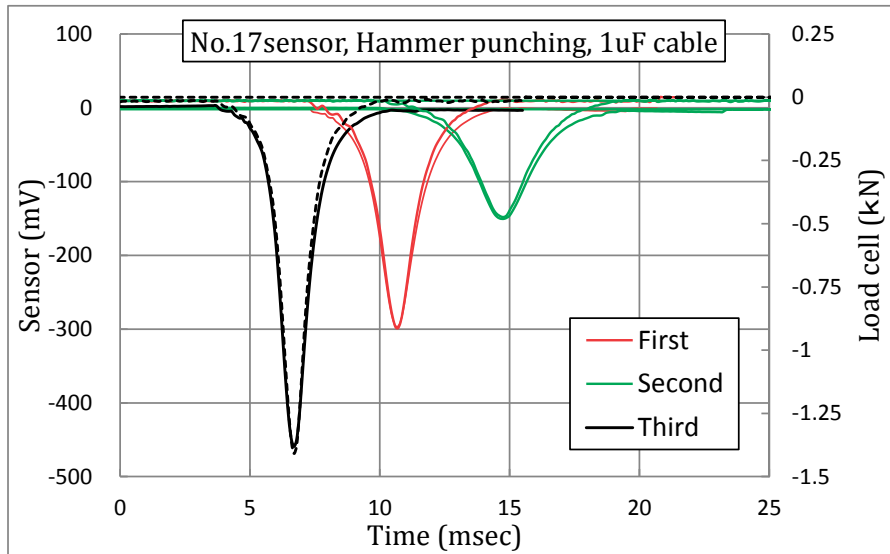


Fig. 5.15 Example of impact force waveform of sensor element (solid curve) and load cell (dashed curve)

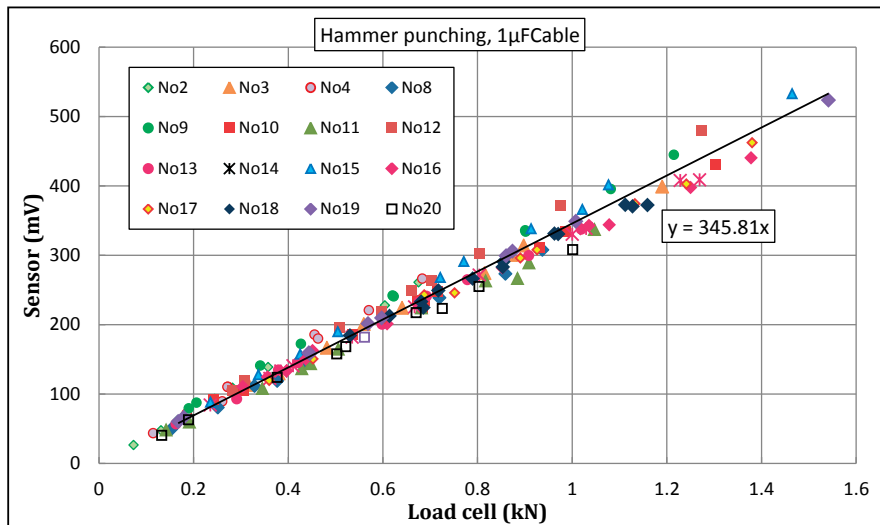


Fig. 5.16 Relationship between sensor output and load cell output obtained by the hammer punching test

5.3.2 Prototype of flexible impact force sensor

Fig.5.17(a) shows a flexible sensor in which sixteen sensor elements are arranged in a 4×4 matrix. The sensor is covered with artificial leather. Its surrounding and the vertical and horizontal column are finished by sewing. The total size is about 230 mm

square. Fig.5.17(b) shows the sensor inserted into conductive cloth bag for static shielding. Green cable is the ground wire. Piezoelectric sensors are prone to be influenced by static electricity [9] [10]. In order to prevent the signal drift by static electricity, it is preferable to use in the state of electrostatic shielding. Fig.5.17(c) shows the state in holding by bending the sensor. Even though the sensor element itself is a rigid body, the connecting portions of the sensor elements can keep the flexibility.

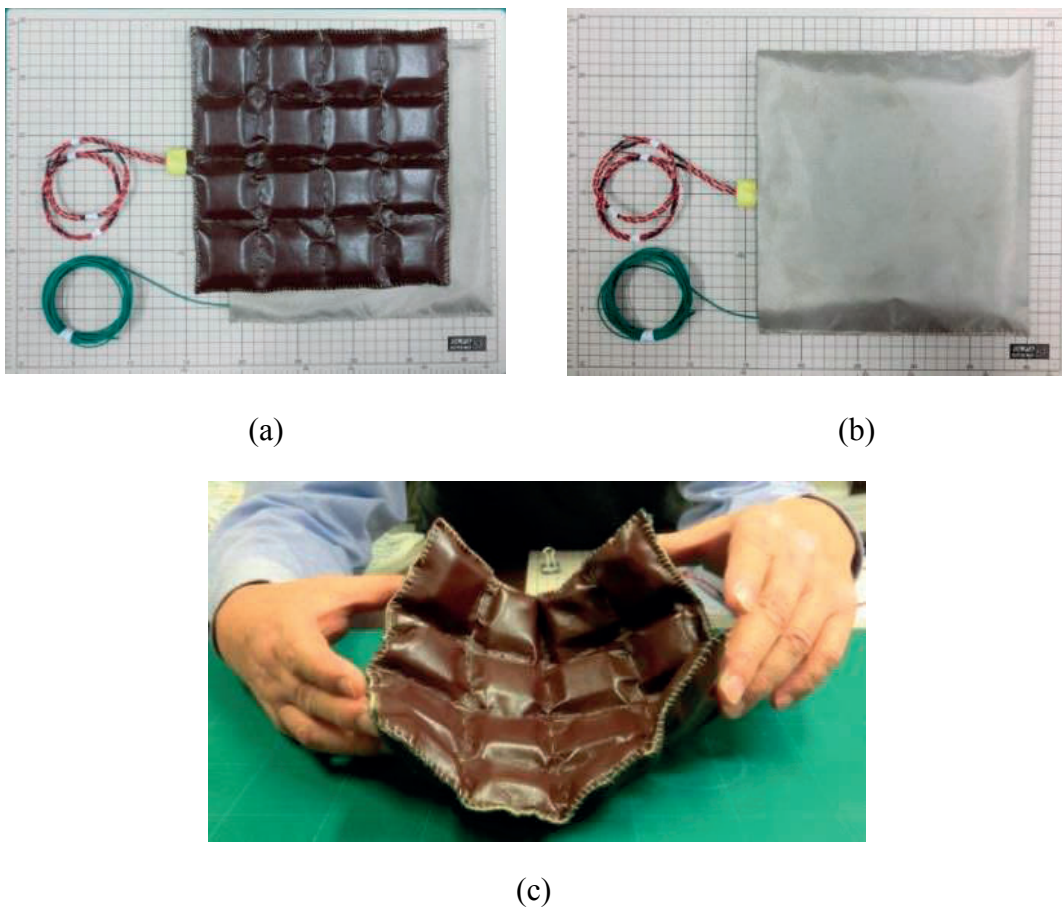


Fig. 5.17 Prototype sensor. (a) Flexible sensor consisting of 4x4 sensor elements. (b) Conductive cloth bag. (c) Hold the sensor bend

Fig.5.18 shows the cross section view of the flexible sensor. The upper aluminum plates of all sensor elements are in contact with the upper conductive cloth. Further, the lower aluminum plates of all sensor elements are in contact with the lower conductive

cloth. In order to prevent short-circuiting of the upper and lower conductive cloth, bilayer deer skin is sandwiched in the thickness center of the sensor as the insulation sheet. After sewing the intermediate portion of the sensor element and element, each sensor element is in a state put into a pocket.

The electrical wires are connected to the lower and upper conductive cloth respectively. In other words, the output signal of the sensor element is obtained from the conductive cloth via upper and lower aluminum plate. Because there is no electrical wiring to connect each sensor element, there is no risk of electric disconnection.

It is obvious that the flexibility of the sensor increases as the increase of the number of sensor elements distributed. If the sensor element is assumed as “a plate placed on the elastic floor”, the bending moment reduces along with the sensor dimension becomes smaller. Therefore, it is possible to reduce the sensor thickness as the size of sensor element is small.

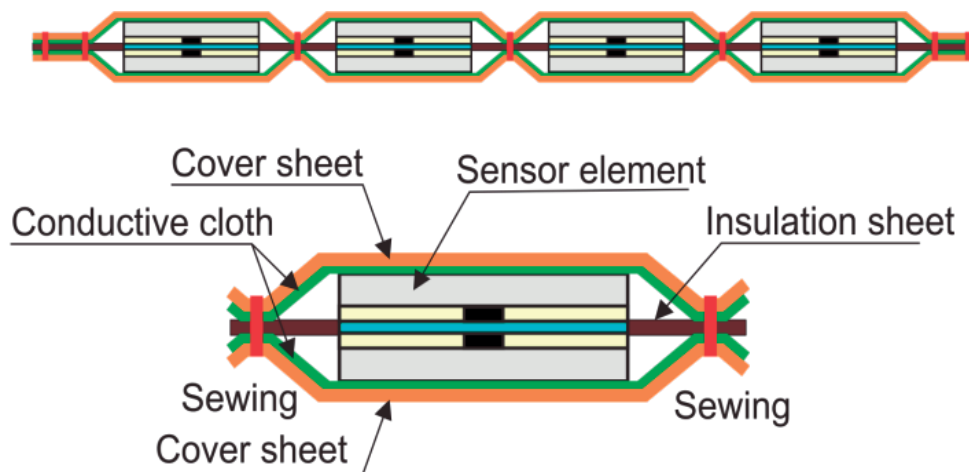
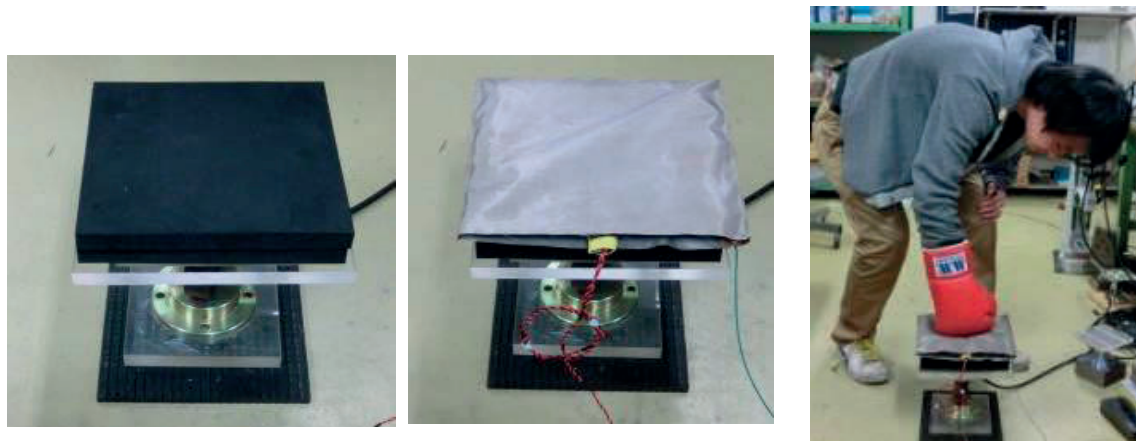


Fig. 5.18 Schematic view of sensor cross-section. Cover sheet is artificial leather. Insulation sheet is bilayer deer skin

5.4 Experiment

5.4.1 Comparison of Sensor Output and Load Cell Output

Fig.5.19 shows the photos of boxing punching test. First, thick acryl plate was fixed on the top of a load cell with 10 kN capacity. Sponge rubber sheet with 40 mm thickness was placed on it. Then, the flexible sensor inserted in the conductive cloth bag was placed on the sponge rubber and a student punched it by boxing glove. Since the sponge rubber is pretty thick, the central portion of the sensor is deformed concave by the punching. Also, similar experiment was conducted under the condition that the flexible sensor was placed directly on the acryl plate.



(a) (b) (c)
Fig. 5.19 Impact test of flexible sensor on the load cell. (a) Sponge rubber ($t=40\text{mm}$) put on the load cell. (b) Sensor placed on the sponge rubber. (c) Punching test by boxing glove

Fig.5.20 shows an example of impact force waveform measured in the above punching test. Solid and dashed curves indicate the experiments on the sponge rubber and the acryl plate respectively. The red curve is sensor output and the black curve is load cell

output. The impact force waveform of the sensor is in good agreement with that of load cell.

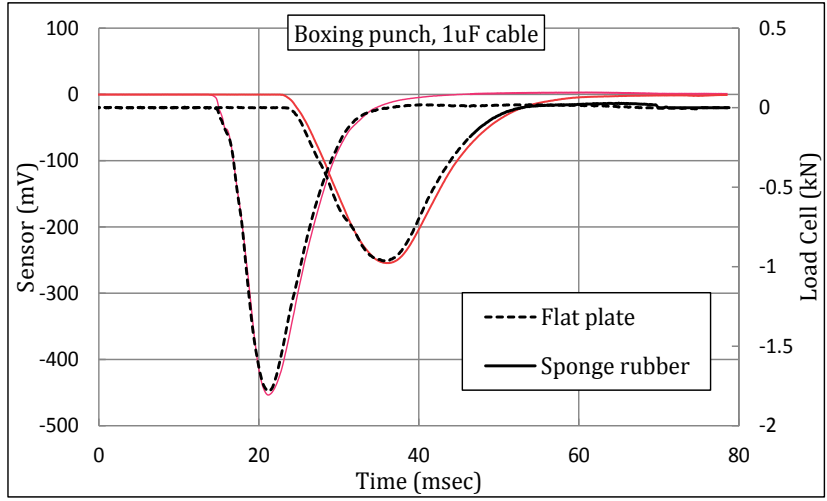


Fig. 5.20 Impact force waveforms of the sensor and the load cell. Red curve is sensor, black curve is load cell

Fig.5.21 shows the relationship between output peak of the sensor and output peak of the load cell. Regardless of the presence or absence of sponge rubber, the sensor output shows almost same gradient. This means that the sensor can measure the impact force in the flexible interface.

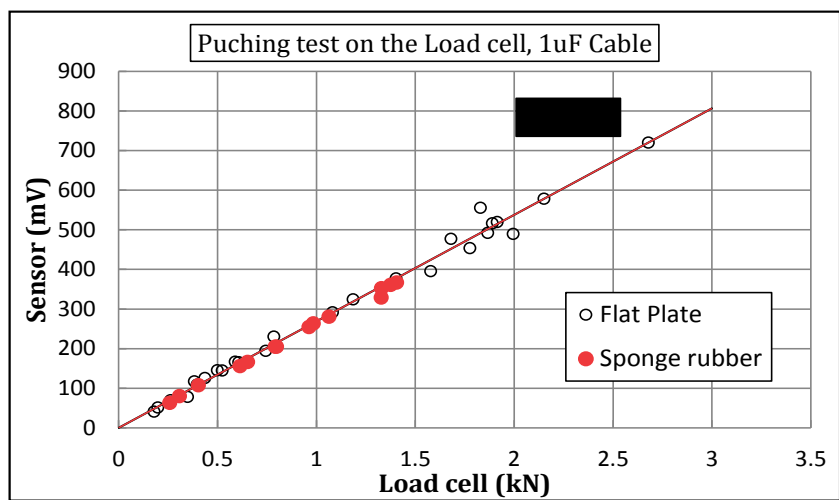


Fig. 5.21 Comparison of the peak output between sensor and load cell

Fig.5.22 shows sponge sheet with 40 mm thickness overlaid on the sponge rubber. The total thickness of the bilayer is 80 mm. The sensor was placed on the sponge sheet and punched by boxing glove. In the figure, two examples of the impact force waveform are compared with that of the load cell output. As the sponge is so soft, the sensor was greatly deformed in a concave shape. There is somewhat difference in the waveform of sensor and load cell.

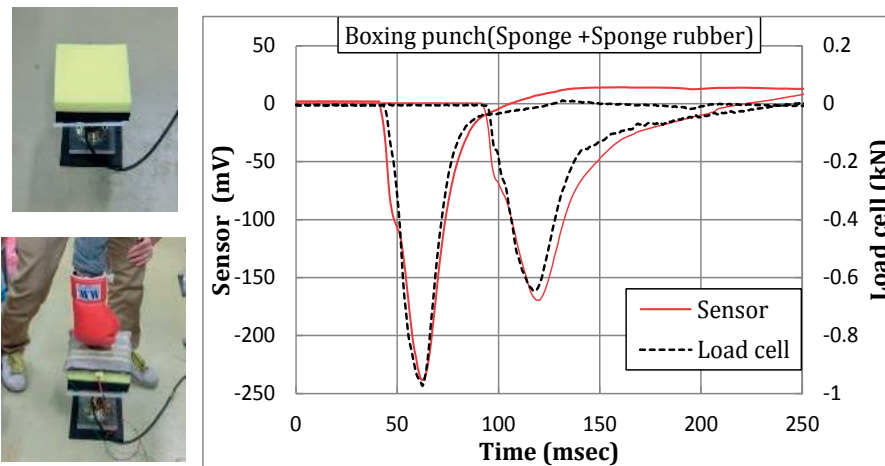


Fig. 5.22 Impact force waveform of sensor and load cell. Sponge is overlaid on top of the sponge rubber

Fig.5.23 shows the sensor placed in bent condition on the wood semicircular column with diameter 150 mm. Some positions of the sensor were fixed with gum tape. Then, the sensor was punched by boxing glove. The relationship between the load cell output and the sensor output are indicated by black diamond. The red circle in the figure is the output gradient of the experiment shown in Fig.5.22. These two gradients are substantially coincident. Moreover, this output gradient is in good agreement with that in Fig.5.21.

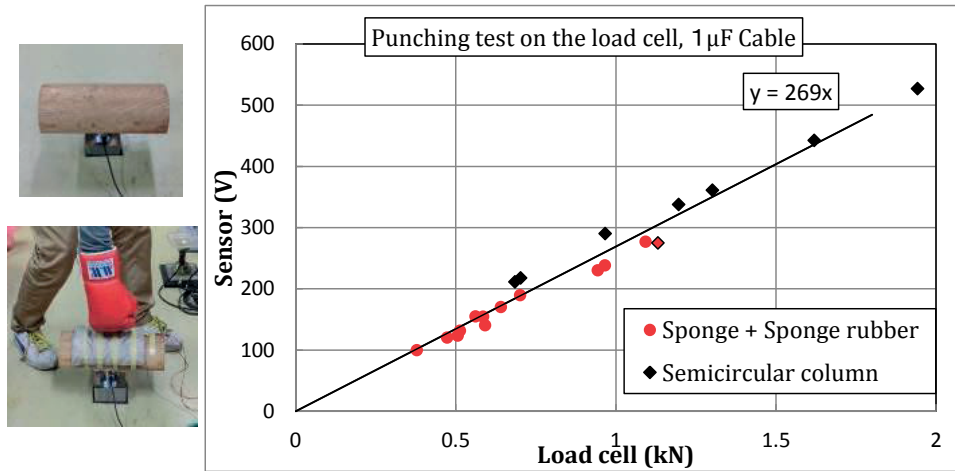


Fig. 5.23 Relationship between sensor output and load cell output. Black diamond: semicircular column. Red circle: sponge & sponge rubber sheet

5.4.2 Punching Test of the Sensor Installed on Concrete Wall

Fig.5.24 shows the punching test by boxing glove on concrete wall. Firstly, sponge rubber sheet (40mm thickness) was pasted on the concrete wall. The sensor was placed on the sponge rubber sheet and the several parts are fixed on the wall with gum tape. Four impact force waveforms weakly punched by student ‘U’ and two waveforms strongly punched by student ‘F’ are shown in the figure. The peak impact force by the strong punching is around 2kN. The contact time is about 30~40msec.

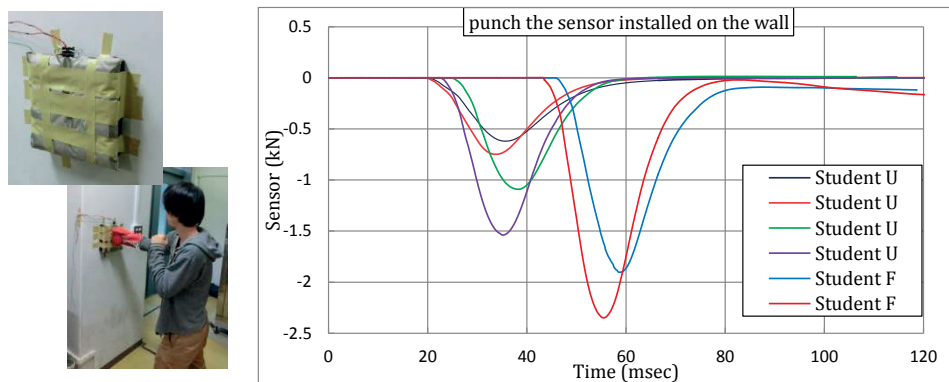


Fig. 5.24 Boxing punching of the sensor installed on the 40mm thick sponge rubber pasted on concrete wall

5.4.3 Punching Test of the Sensor Installed on Sandbag

Fig.5.25 shows the experiment of boxing punching. Sensor was placed on the surface of a sandbag (soft sandbag) of gymnasium and fixed with gum tape. Compared with the punching on the concrete wall, the sandbag is softer and a concave deformation is induced on sandbag surface by punching.

Fig.5.26 shows the impact force waveforms. The peak impact force ranges 0.7kN and 0.9kN. The contact time is about 70msec and this is longer than that on the wall punching. In the figure, it is seen that the gradient of impact force becomes gentle from the middle of unloading. This reason is considered as follows. The sandbag swings rearward by the punching. Therefore, the forward speed of the glove persists for a while even after passing the peak load. Since the pull-back of the glove is delayed, the contact between glove and sandbag is continued for a while. The difference of the gradient of unloading segment is clear when compared to the waveform of wall punching in Fig.5.24.

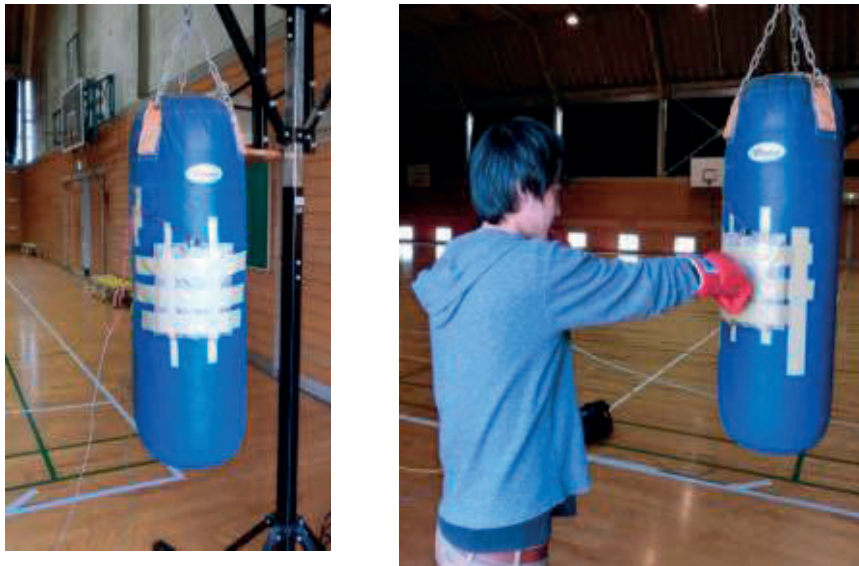


Fig. 5.25 Boxing punching of the sensor installed on the sandbag

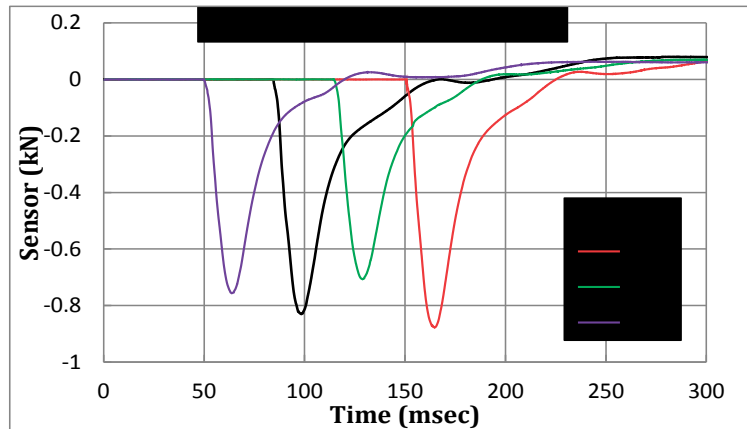


Fig. 5.26 Impact force waveform of the sensor installed on the hard sandbag surface and punched by boxing glove

5.5 Improvement of the Sensor Flexibility

Sensor elements described above is 30 mm square and 12 mm thickness. To improve the flexibility of the sensor, it is necessary to increase the distribution density by reducing size and thickness of the sensor element. Fig.5.27(a) shows slightly small sized sensor elements with 25 mm square and 8 mm thickness. Fig.5.27(b) is a flexible sensor made from the six elements.

Fig.5.28(a) shows the sensor fixed to the instep of soccer shoes with cords and rubber bands. Fig.5.28(b) shows the impact force waveforms of instep kick of soccer ball. The strength of the kick is the extent to path to nearby players. The peak impact force is about 1 kN and the impact time is about 12 - 15 msec. This contact time is close to the value shown in the reference [11].

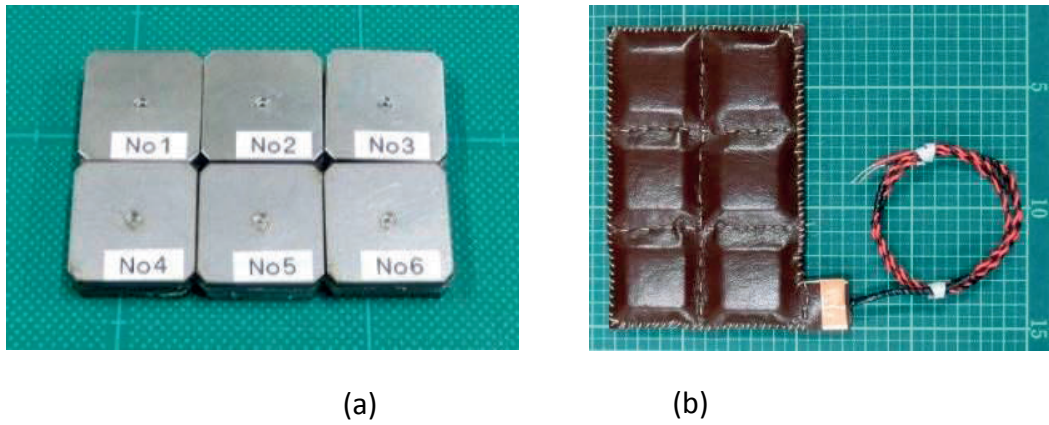


Fig. 5.27 (a) Sensor elements of 25mm square and 8mm thickness. (b) Flexible sensor made from six sensor elements

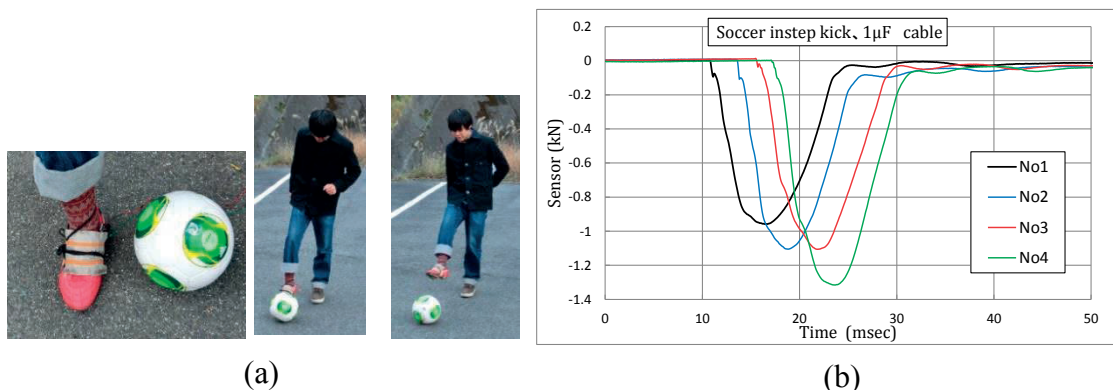


Fig. 5.28 (a) Set up of the sensor on soccer shoe. (b) Impact force waveforms of instep kick of soccer ball

From the experience, it seems possible to miniaturize the element size to 15 mm square and 5 mm thickness. When the element becomes smaller than that, however, reconsideration of the manufacturing process is necessary. In spite of the rough distribution density of the sensor elements, the sandbag sensor was not much discomfort at the time of use. On the other hand, in the soccer shoe sensor, the sensor weight and the lack of flexibility were felt uncomfortable. “Flexibility” and “light weight” are thought to be more important for the sensors installed on human body side.

5.6 Conclusions

This section is aimed to develop a flexible sensor which can be used in the measurement of impact force in flexible interface. The boxing punching is chosen as the measurement object. The results obtained are as follows.

1) A flexible sensor in which sixteen sensor elements are arranged in a 4×4 matrix is developed. Each sensor element is a rigid plate structure. The sensor elements are arranged at regular intervals. Both entire surfaces of the sensor elements are covered with artificial leather, and its surrounding and the vertical and horizontal columns are finished by sewing. Flexibility of the sensor is achieved by the flexible leather connections between adjacent sensor elements;

2) Sum of the output signal of each sensor element is collected through the conductive cloth. Since there is no electrical wiring inside the sensor, the sensor structure is hard to break by the impact force which is realized;

3) Boxing punching experiments were carried out by installing the sensor on concrete wall and sandbag. The flexible sensor showed a good performance in the experiments;

4) The proposed sensor is inadequate distribution number of sensor elements, but the proposed sensor includes mechanisms to achieve a flexible sensor with high accuracy. By increasing the distribution density of the sensor element, it can approach to the practical sensor.

Flexibility, thinness, lightness, toughness and accuracy are the keys of flexible impact force sensor. Overcoming of these problems is essential for the realization of the sensor that can be installed on human body or robot.

References

- [1] Ishikawa, M. and Shimojo, M. (1982) A Method for Measuring the Center Position of a Two Dimensional Distributed Load Using Pressure-Conductive Rubber. *Transactions of the Society of Instrument and Control Engineers*, 18, 730-735.
- [2] Mei, T., Li, W.J., Ge, Y., Chen, Y., Ni, L. and Chan, M.H. (2000) An Integrated MEMS Three-Dimensional Tactile Sensor with Large Force Range. *Sensors and Actuators*, 80, 155-162.
- [3] Lee, H.K., Chang, S.I. and Yoon, E. (2006) A Flexible Polymer Tactile Sensor: Fabrication and Modular Expandability for Large Area Deployment. *Journal of Micro Electromechanical Systems*, 15, 1681-1686.
- [4] Donati, M., Vitiello, N., De Rossi, S.M.M., Lenzi, T., Crea, S., Persichetti, A., Giovacchini, F., Koopman, B., Porobnik, J., Munih, M. and Carrozza, M.C. (2013) A Flexible Technology for the Distributed Measurement of Interaction Pressure. *Sensors*, 13, 1021-1045.
- [5] Lee, M.H. and Nicholls, H.R. (1999) Review Article Tactile sensing for Mechatronics-A State of the Art Survey. *Mechatronics*, 9, 1-31.
- [6] Lumelsky, V.J., Shur, M.S. and Wagner, S. (2001) Sensitive Skin. *IEEE Sensors Journal*, 1, 41-51.
- [7] Walilko, T.J., Viano, D.C. and Bir, C.A. (2005) Biomechanics of the Head for Olympic Boxer Punches to the Face. *British Journal of Sports Medicine*, 39, 710-719.
- [8] Fujimoto, Y. and Setyanto, A.T. (2007) Sheet Type Impact Force Sensor by the Use of Piezoelectric Film. *Transactions of the Japan Society of Mechanical Engineers, Series C*, 73, 184-191.
- [9] Fujimoto, Y., Shintaku, E., Tanaka, Y. and Fujiyoshi, J. (2012) Pad Type Compressive Force Sensor Suitable for High-Speed Impact Force Measurement. *Transactions of the Japan Society of Mechanical Engineers, Series C*, 78, 2438-2449.
- [10] Fujimoto, Y., Liu, C., Uesugi, T., Tanaka, Y. and Shintaku, E. (2013) Pipe Surface Sensor for Impulsive Force Measurement. *Transactions of the Japan Society of Mechanical Engineers, Series C*, 79, 113-123.
- [11] Shinkai, H., Nunome, H., Ikegami, Y. and Isokawa, M. (2008) Ball-Foot Interaction in Impact Phase of Instep Soccer Kick. In: Reilly, T. and Korkusuz, F., Eds., *Science and Football VI, The Proceedings of the 6th World Congress on Science and Football*, Routledge, Abingdon, 41-46.

Chapter 6 Thorn Shape and Double-Strike Phenomenon Seen in the Impact Force Waveform of Soft Materials

In impact tests of soft materials such as rubber, clay, or soft plastic, we sometimes observe a thorn shape in the rising segment of the impulsive force waveform. Several thorn-shape waveforms can be seen in the impact test results of previous research studies [1–3]. However, the physical meaning of the thorn shape has not been discussed much.

Recently, we have developed an impact force sensor that can measure a high-speed impact force waveform accurately [4, 5], and we have performed impact tests on several soft materials using the sensor. While repeating the experiments, the authors realized that the thorn-shape waveform can be clearly measured under the condition of a flat frontal impact. Also, the authors pointed out the possibility that the thorn-shape waveform is related to the strain rate dependence of the material and the double-strike phenomenon [6].

In this study, free drop impact tests are performed on several soft materials using compact drop test equipment. The thorn-shape waveforms are observed from a bird's-eye view. Further, the occurrence mechanism of the thorn-shape waveform is discussed from the viewpoint of viscosity discontinuity and the double-strike phenomenon.

6.1 Thorn Shape and Double-Strike Phenomenon Seen in the Impact Force Waveform of Soft Materials

Fig.6.1(a) shows a soft material subjected to a flat frontal impact. The impact object is a free drop hammer. Fig.6.1(b) shows typical thorn-shape waveforms of the impact force. The features of the thorn-shape waveform are a steep slope on the rising segment (which is θ) and a thorn-shape waveform similar to the yield point of low-carbon steel. After that, at a certain point, it becomes a gentler slope (which is α) and generates a second mountain-shape waveform. The rising segment of the thorn is usually close to a straight line.

Fig.6.1(c) summarizes the occurrence mechanism of thorn-shape waveforms obtained by the following experimental observation. The impact force waveform of soft materials is the mixture of two types of waveforms. The first (thorn-shape) waveform shows a large viscosity resistance (red curve), and the second (mountain-shape) waveform shows a small viscosity resistance (dashed black curve). This resistance change occurs suddenly at the thorn peak; that is, a viscosity discontinuity (viscosity transient) is induced at the thorn peak. The compressive stress at the thorn peak is the trigger of the softening. The soft material surface is struck twice by the relative movement of collision objects. The reason why the slope α becomes smaller than the initial slope θ is because a viscosity discontinuity is induced by the first strike.

Fig.6.2 shows three types of thorn-shape waveforms measured in the following experiments:

Type I: In the case where the soft material is crushed into pieces by the first impact, only a thorn-shape waveform appears, and the second mountain-shape waveform does not appear.

Type II: This type of waveform appears in most of the soft materials. The slope θ and thorn peak are influenced by the material, impact velocity, material thickness, etc. In this waveform, a certain compressive force still remains after the first impact. This means that the hammer bottom and soft material surface remain in contact during unloading.

Type III: This type of waveform is observed in the thick soft material. The hammer bottom and the soft material surface have a non-contact condition for a moment after the first impact.

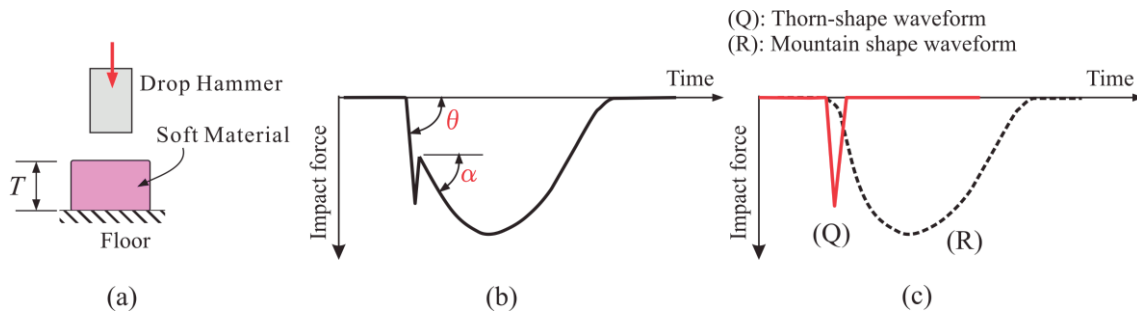


Fig. 6.1 Impact force waveform of soft material. (a) Flat frontal impact by free drop hammer and plate-like soft material. (b) Typical impact force waveform of soft material including thorn. (c) Two types of waveforms contained in the impact force waveform of soft material.

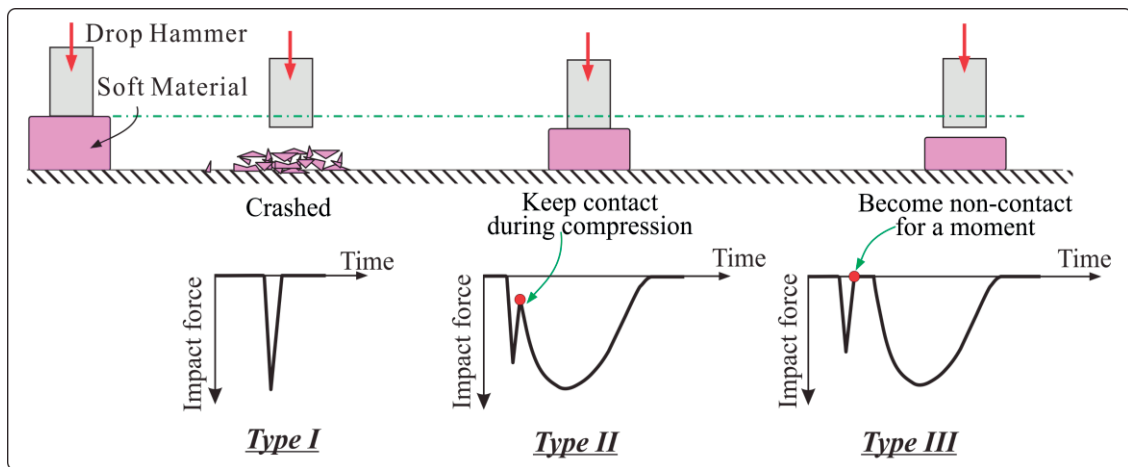


Fig. 6.2 Three types of thorn-shape waveforms observed in the impact force of soft material.

6.2 Condition of Flat Frontal Impact and Compact Drop Test Equipment

Through a number of experiments, we found that the thorn-shape waveform can be measured clearly under the condition of a flat frontal impact. In Fig.6.3, the impact object is a solid material with a flat contact surface. The soft material that receives the impact force is a plate-like material with a uniform thickness without surface irregularities. The impact object strikes the soft material in the normal direction. The thorn-shape waveform can be steadily measured in the above condition. When the bottom surface of the impact object is curved (Fig.6.3(b)), when the impact object is tilted (Fig.6.3 (c)), or when the upper surface of the soft material is curved (Fig.6.3(d)), the thorn becomes unclear. Here, “unclear” does not mean that the thorn will not occur; it is unclear in that the contact area gradually expands from the local area, and the phenomenon is diluted

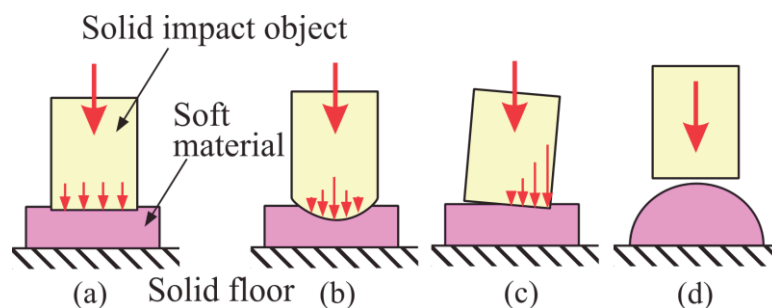


Fig. 6.3 (a) Flat frontal impact condition that the thorn appears clearly. (b), (c), (d) are the conditions where the thorn becomes indistinct.

Fig.6.4 shows the free drop test equipment used in this study. The device is braced by vertical columns on the left and right of the bottom plate. The top of the side column is connected with a metal plate. The drop hammer is made of an aluminum circular disk

plate and a stainless cylinder (mass of 1.9 kg). The contact surface of the hammer bottom is a disk plate with a diameter of $D=60$ mm. The upper sensor is an orbicular pad sensor and is attached near the drop hammer bottom. The lower sensor is a pad sensor of 100 mm square and is attached to the frame bottom. Both sensors are made from piezoelectric film. A high-speed voltage recorder with a sampling rate of 20–200 kHz is used for recording the sensor output. The output of the upper sensor is modified by 8% to account for the mass of the disk plate. Based on rigorous tests using a servo-controlled testing machine and a high-rigidity load cell, it was confirmed that both sensors can measure the impact force very accurately when the contact time is in the range between 0.1 msec and 2 sec. The drop height h is the height from the upper surface of the soft material to the bottom surface of the drop hammer. The impact velocity is $V_0=1.4$ m/sec when $h=0.1$ m, $V_0=1.98$ m/sec when $h=0.2$ m and $V_0=2.73$ m/sec when $h=0.38$ m.

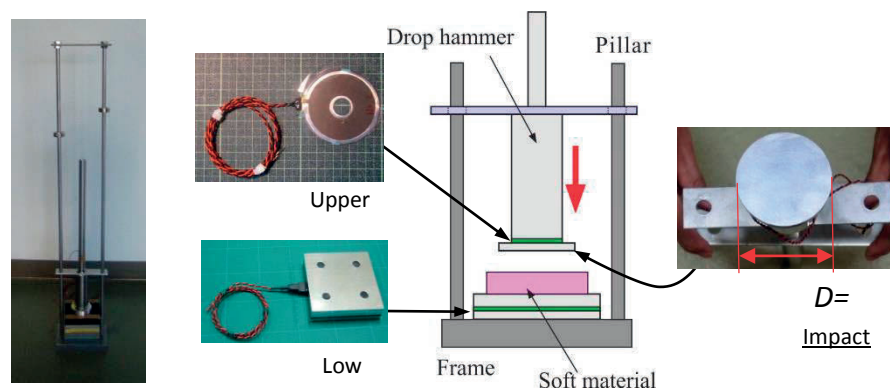


Fig. 6.4 Drop test equipment and the upper and lower sensors used in the device.

Fig.6.5 shows the importance of the flat frontal impact. Fig.6.5(a) shows wood blocks (triangular prism, semicircular column, and hemisphere) that are fixed to the bottom of the free drop hammer. The soft material is a nitrile rubber plate (NBR) with a 30 mm thickness. The drop height is $h=380$ mm. Fig.6.5(b) shows the measured impact force waveforms. The waveform under the flat frontal impact condition (without a wood block) is also shown in the figure. The thorn-shape waveform appears clearly under the

flat frontal impact. However, when the block corner or a curved surface locally strikes the rubber, the thorn-shape waveform is not obvious.

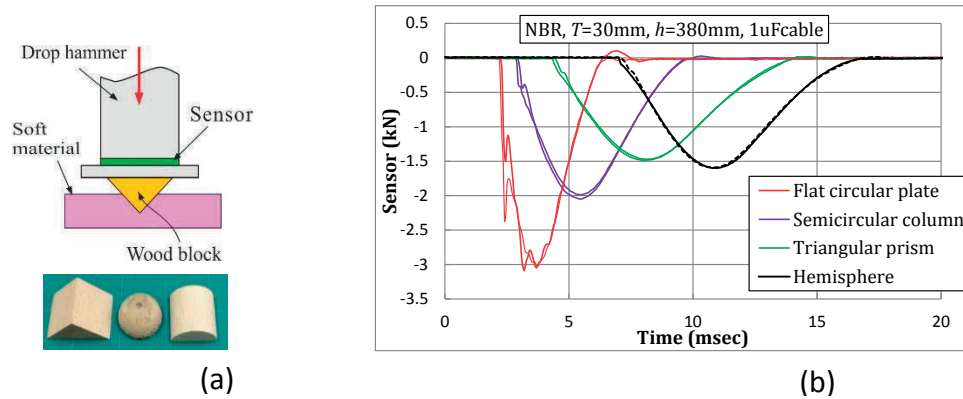


Fig. 6.5 Influence of contact shape on impact force waveform: (a) wood blocks attached to the drop hammer bottom; (b) comparison of the waveform of the flat frontal impact and those of other impact conditions.

6.3 Experimental results

6.3.1 Impact Force of Agar Jelly under Flat Frontal Impact (*Type I* waveform)

Fig.6.6 shows two examples of impact force waveforms for an agar jelly with a 30 mm thickness. The height of the drop hammer is $h=380$ mm. The initial strain rate at the collision is $\dot{\epsilon}_0 = V_0 / T = 91 \text{ sec}^{-1}$, where V_0 is the hammer speed at the collision, and T is the soft material thickness. When the drop hammer collides, the agar jelly is crushed and scattered as juice. Therefore, the thorn-shape waveform (*Type I* waveform) appears only in the upper sensor output. The thorn is close to an isosceles triangle, and its contact time is short at 0.5 msec. The impulse of the thorn part is quite small compared with the total momentum of the drop hammer (5.19 N·sec). The impact force seen in the lower sensor

output is delayed. This may be caused by the crush effect. Because the jelly was crushed at the thorn peak, the impact force is reduced to zero. About 15 msec later, the hammer bottom strikes the lower sensor strongly without losing much of its falling velocity.

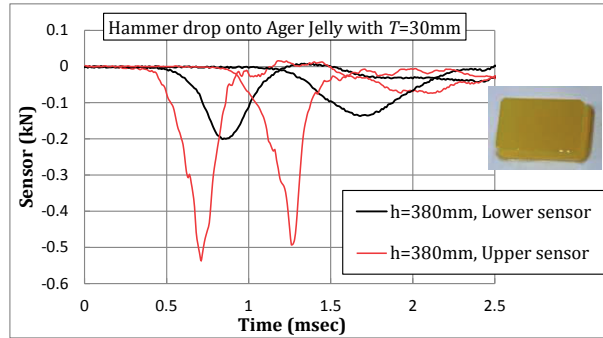


Fig. 6.6 Impact force waveform induced by the hammer drop onto agar jelly.

6.3.2 Impact Force of Konjac under Flat Frontal Impact (*Type III* Waveform)

Fig.6.7 shows the impact force waveforms and an enlarged view of a konjac plate with a 40 mm thickness. The drop height is $h=100$ mm ($\dot{\epsilon}_0 = V_0 / T = 35 \text{ sec}^{-1}$) and 380 mm ($\dot{\epsilon}_0 = 68 \text{ sec}^{-1}$). The konjac plate is compressed greatly by the impact but not crushed. In the figure, the time interval between the thorn-shape waveform and the succeeding mountain-shape waveform is wide, and the double-strike phenomenon is obvious (*Type III* waveform). In the magnified figure, the thorn is close to an isosceles triangle, and its contact time is short at 0.8 msec. Also, a small thorn can be seen in the lower sensor output. The impulse of the thorn part is quite small compared with the succeeding mountain-shape waveform. This means that most of the falling velocity is lost at the second mountain-shape waveform. Usually, the thorn shapes of the upper and lower sensor outputs are close when the material thickness is smaller.

6.3.3 Impact Force of Gel Sheet under Flat Frontal Impact (*Type II* waveform)

Fig.6.8 (a) shows the impact force waveforms of a gel sheet (product name: α gel) with a 20 mm thickness. Fig.6.8 (b) is an enlarged view of the thorn part. The drop height is $h=380$ mm ($\dot{\epsilon}_0 = V_0 / T = 136 \text{ sec}^{-1}$). The thorn-shape waveform can be seen clearly in both the upper and lower sensor outputs (*Type II* waveform). In the enlarged view, we can observe that the slope θ of the rising segment is larger than the slope α of the segment past the thorn. The impulse of the thorn part is quite small compared with the succeeding mountain-shape waveform.

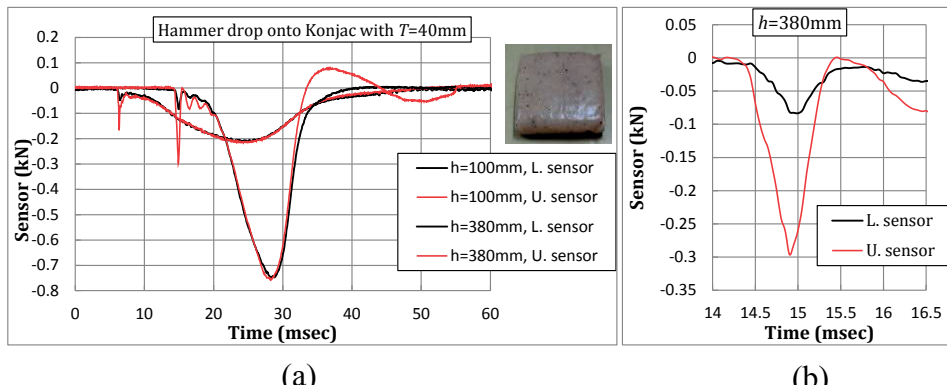


Fig. 6.7 (a) Impact force waveforms induced by hammer drop onto konjac with a 40mm thickness; (b) enlarged figure of thorn part for the case of $h=380$ mm.

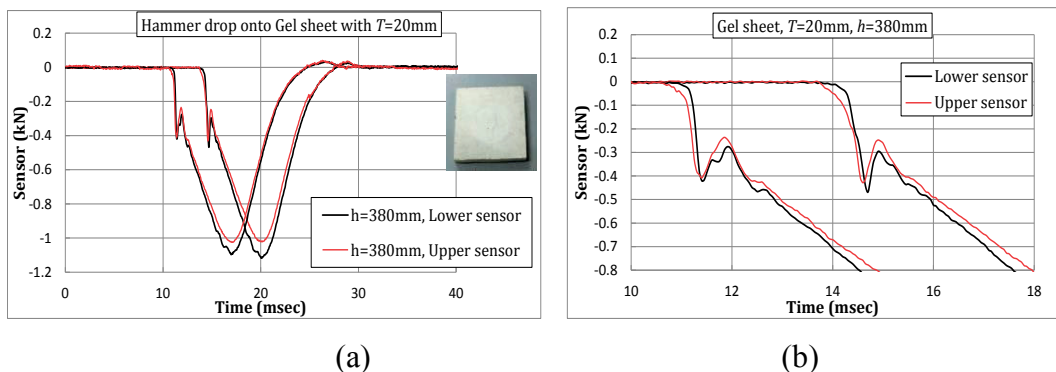
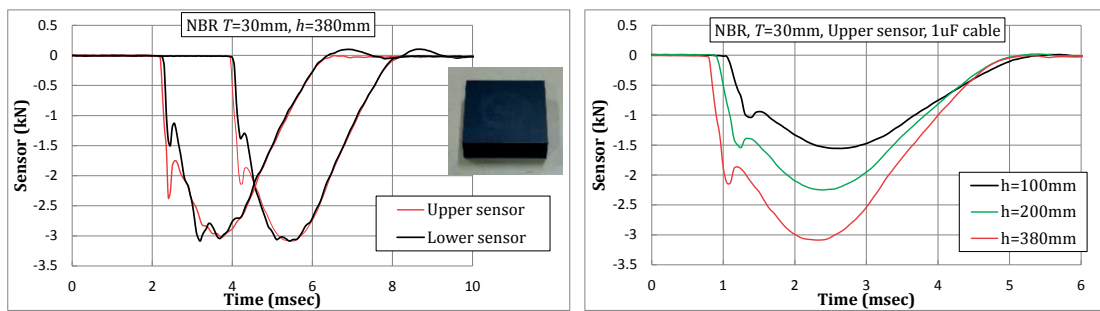


Fig. 6.8 (a) Impact force waveform induced by the hammer drop onto a gel sheet with a 20mm thickness; (b) enlarged figure of the thorn part.

6.3.4 Impact Force of Nitrile Rubber (NBR) Plate under Flat Frontal Impact (*Type II* waveform)

Fig.6.9 (a) is the impact force of an NBR plate with $T=30$ mm (rubber hardness of 50). The drop height is $h=380$ mm ($\dot{\epsilon}_0 = 91 \text{ sec}^{-1}$). The upper sensor output shows a relatively large thorn, and the lower sensor output shows a smaller thorn. The slopes θ of the upper and lower sensor outputs are almost the same. Fig.6.9 (b) compares the impact force waveforms of the upper sensor for drop heights of $h=100$, 200, and 380 mm. In the figure, when the impact velocity V_0 is faster, the slope θ of the rising segment and the height of the thorn peak are larger. This means that the slope θ and the height of the thorn peak are dependent on the impact velocity or strain rate.



(a) (b)
Fig. 6.9 Impulsive force induced by the hammer drop onto NBR with $T=30$ mm.

6.3.5 Impact Force of Oil Clay Plate under Flat Frontal Impact (*Type II* waveform)

Fig.6.10 shows the impact force waveform of an oil clay plate with a 50 mm thickness. The drop height is $h=100$ and 530 mm. A large thorn is seen by the upper sensor, and a small thorn is seen by the lower sensor. As the drop height increases (V_0 becomes faster), the slope θ becomes larger, and the thorn peak becomes taller. The thorns are more obvious than those of other materials. From the enlarged view, the thorn shape is close to

an isosceles triangle.

6.3.6 Impact Force of Low-Rebound Urethane Foam under Flat Frontal Impact (*Type II* waveform)

Fig.6.11 shows the impact force waveform of low-rebound urethane foam with a 40 mm thickness. The drop height is $h=380$ mm. In this case, the bottom diameter of the drop hammer is 60 and 75 mm. In the figure, the steep slope of the rising segment is bent approximately 90 degrees at a certain force level. Also, a small thorn can be seen at the bent corner. Since low-rebound urethane foam is a high-viscosity material, the material shows a strong viscous resistance (hardening) until reaching a certain compressive stress.

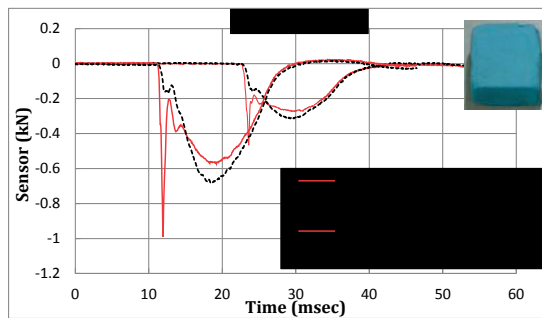


Fig. 6.10 Impact force induced by the hammer drop onto oil clay with a 50mm thickness.

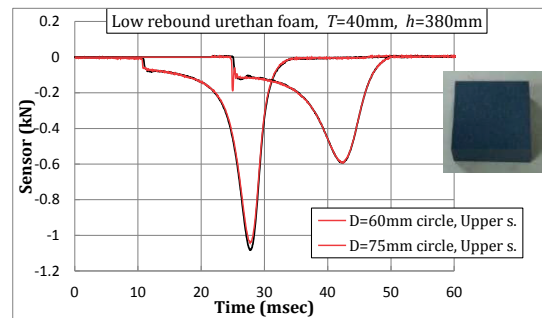


Fig. 6.11 Impact force induced by the hammer drop onto low-rebound urethane foam.

6.3.7 Impact Force of Ham and Edible Meat under Flat Frontal Impact (*Type II* waveform)

Fig.6.12 shows the impact force waveforms of sliced ham ($T=21$ mm), pork ham steak ($T=19$ mm), pork ($T=25$ mm), and konjac ($T=20$ mm). The drop heights are all $h=380$ mm. The solid curve represents the upper sensor output, and the dashed curve represents the lower sensor output. We can see the steep slope θ in the ascending segment and the thorns in both the upper and lower sensor outputs.

Table 6.1 compares the falling momentum of the drop hammer and the impulse of the impact force waveform. The impulse is calculated by numerically integrating the area of the waveform. The impulse is about 10% larger than the falling momentum.

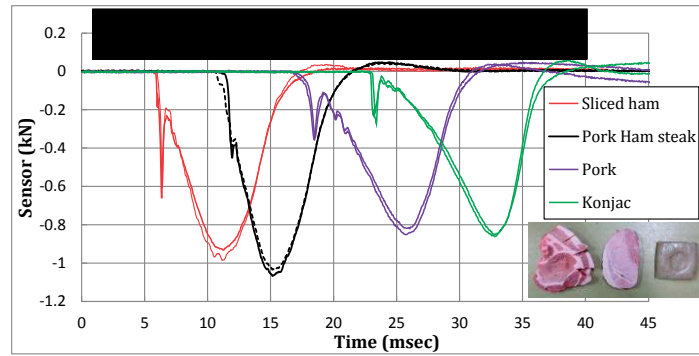


Fig. 6.12 Impact force induced by the hammer drop onto sliced ham, pork ham steak, pork and konjac.

Table 6.1 Momentum and impulse of impact force induced by the hammer drop.

Mass of drop weight m (kg)	Falling height h (m)	Momentum mV (N·sec)	Material	Thickness T (mm)	Impulse (N·sec)
					Lower sensor
1.9	0.38	5.19	Sliced ham	21	5.92
			Pork ham steak	19	5.58
			Pork	25	5.58
			Konjac	20	5.28

6.4 Measurement of Triple-Strike Waveform

Thin aluminum circular plates with a diameter of 25 mm and different thicknesses of $d=0.5, 1.0, 2.0, 3.0,$ and 5.0 mm are prepared. Each plate is attached to the bottom of the drop hammer with adhesive tape, as shown in Fig.6.13 (a). Then, the hammer is dropped from $h=380$ mm onto the NBR plate with a 30 mm thickness. The hammer bottom collides in two stages. The contact area at the first impact is a circle with a 25 mm diameter, and the second is a ring-shape area with a diameter range from 25 to 60 mm.

Fig.6.13 (b) shows the impact waveforms for all of the cases. The solid curves correspond to the upper sensor, and the dashed curves correspond to the lower sensor. We can see two thorn-shape waveforms and one mountain-shape waveform when d is 3 mm or less. The first thorn is due to the impact by the small circular plate. The second thorn is due to the impact by the ring-shape area. The bending point between the first and second thorns indicates the start of contact of the ring-shape area (shown by the blue arrow in the case of $d=2$ mm).

In the typical double-strike phenomenon, the second strike makes a mountain-shape waveform. Therefore, the authors think that the second thorn such as that shown in Fig.6.13 (b) will occur only if the drop hammer strikes the virgin surface of the soft material.

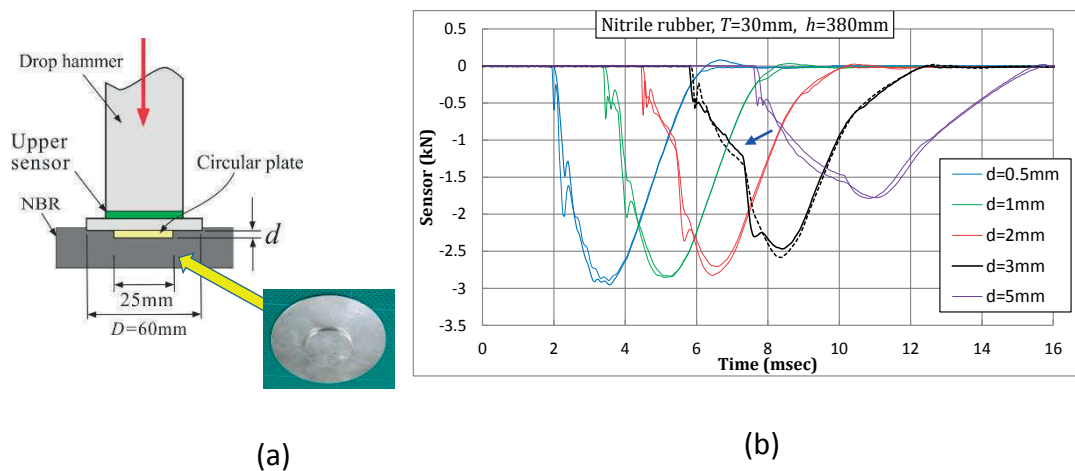


Fig. 6.13 Measurement of triple-strike waveform of impact force: (a) aluminum circular plate is attached to the bottom of the drop hammer; (b) impact force induced by the hammer drop onto NBR with a 30mm thickness.

6.5 Mechanism of Thorn-Shape Waveform and Double-Strike Phenomenon

6.5.1 Contact Time of Thorn-Shape Waveform

Table 2 shows the contact time t_c of the thorn-shape waveform (approximated by an isosceles triangle) and $\dot{\epsilon}_0$ for some soft materials. The value of t_c ranges between 0.4 msec and 1.0 msec. Fig.6.14 shows the impact force waveform of a thick aluminum plate punched by a plastic hand hammer (PVC head). Its t_c is 0.74 msec, and this value is close to those of soft materials. The material hardness is the main factor that governs t_c . Therefore, this result means that the soft materials reached almost the same hardness as the plastic hammer head at the thorn.

Table 6.2 Contact time of thorn-shapewaefom for soft materials.

Soft material	Contact time t_c (msec)	$d\epsilon_0/dt = V_0/T$ (sec^{-1})
Ager Jelly	0.5	91
Gel Sheet	0.8	136
Konjac	0.8	68
Oil Clay	0.4	273
Oil Clay	1.0	136
NBR	0.5	91
Low rebound Urethane Foan	0.7	68

$h=380\text{mm}$

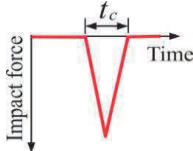
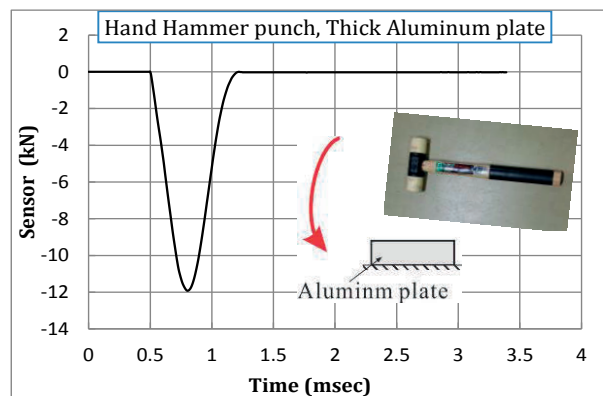



Fig. 6.14 Impact force of aluminum plate punched by plastic hand hammer.

6.5.2 Thickness Effect of Soft Material

Fig.6.15 shows the impact force waveforms of oil clay plates with $T=10, 20,$ and 50 mm. The solid curve is the upper sensor output, and the dashed curve is the lower sensor output. The drop heights are all $h=380$ mm (impact velocity is $V_0 = 2.73$ m/sec). The strain rate at contact is $\dot{\epsilon}_0 = V_0/T = 273 \text{ sec}^{-1}, 137 \text{ sec}^{-1},$ and 54.6 sec^{-1} , respectively. In the figure, it is clear that the slope θ and the peak force of the thorn are influenced by the strain rate. The second mountain-shape waveform is also influenced by the strain rate.

The authors also performed experiments on cork sheet, sponge sheet, sponge rubber, paper clay, tofu, relatively smooth areas of human skin, and some hollow balls. Among them, all of the materials except the cork sheet showed a thorn-shape waveform.

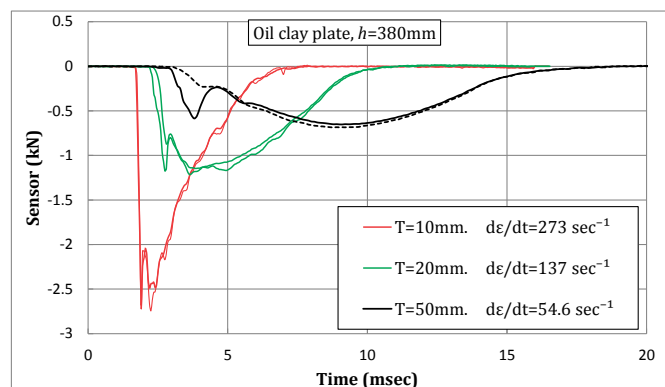


Fig. 6.15 Thickness effect of oil clay plate on the impact force waveform. Drop heights are all $h=380$ mm. Solid curve is upper sensor, and dashed curve is lower sensor.

6.5.3 Mechanism of Thorn-Shape Waveform

Fig.6.16 shows the authors' understanding of the occurrence mechanism for the thorn-shape waveform based on the above experimental observations.

In the rising segment P1–P2 of Fig.6.16, the viscosity resistance is excessively large, and the waveform shows a steep slope θ .

At the thorn peak P2, the viscosity resistance changes suddenly (viscosity transient). The large viscous resistance is broken by the thorn peak force and is softened to a certain extent.

When the viscosity resistance becomes small, the soft material is relaxed for a moment, and unloading occurs in the region P2–P3. When the softened material starts compressive deformation, the relative downward velocity between the hammer and the soft material surface decreases for a moment. This is the cause of unloading.

However, the hammer speed catches up to the soft material surface at the point P3 and strikes it again. The second mountain-shape waveform shows a gentler slope α in the region P3–P4 because the viscosity resistance becomes small. The soft material shows a small viscosity resistance in the region P3–P5.

Based on the understanding of the above, the authors showed that the impact force waveform consisting of a thorn and mountain shape waveform can be simulated by using a simple dynamics model (SLS model) [7].

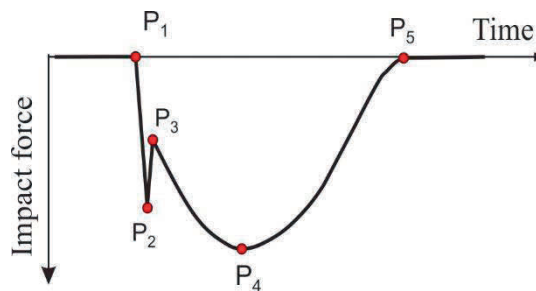


Fig. 6.16 Mechanism of impact force waveform for soft materials based on the experimental observations.

Fig.6.17 shows a schematic expression of the relationship between the viscosity resistance and the strain rate. The authors think that two types of viscosity resistance appear in the impact force of soft materials. One is the excessively large viscosity

resistance (red curve) that appears in the first stage. The other is the small viscosity resistance (black dashed curve) that appears in the second stage. This viscosity transient (green dashed arrow) occurs at the thorn peak.

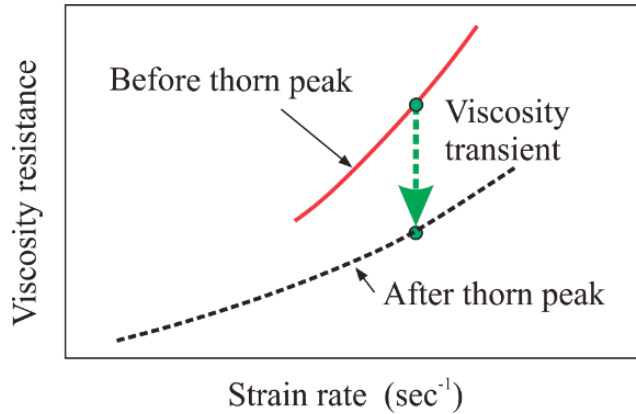


Fig. 6.17 Viscosity transient vs. strain rate relationship.

In some colloidal suspensions, the viscosity transient is known as “viscosity discontinuity” [8, 9]. Our experimental results indicate that the viscosity discontinuity may also occur in most soft materials.

It is known that the stress-strain curve of some soft materials under high strain rate is not a monotonically increasing function. It shows stress relaxation after the elastic peak [10]. This relaxation may be related to the viscosity discontinuity.

In running sports, it is known that a thorn-shape waveform called an “initial spike” can be observed [11]. When the heel strikes the ground first, it rebounds rapidly because the heel is hard. As a result, the heel generates a thorn-like waveform. Along with the movement of the center of gravity of the human body, the forefoot striking generates the second mountain-shape waveform. This is also understood as the double-strike phenomenon consisting of the first hard heel strike and the second soft forefoot strike.

6.6 Conclusions

Using compact drop test equipment, this study experimentally observed the impact force waveforms for several kinds of soft materials. The results obtained here are as follows:

1. Thorn-shape waveform of soft material appears clearly under the condition of a flat frontal impact. If either surface of the drop hammer or the soft material is curved, the thorn-shape waveform becomes un-clear.
2. Most of the soft materials (except cork sheet) such as sponge, sponge rubber, nitrile rubber, oil clay, paper clay, low-rebound urethane foam, ham, pork, and konjac showed a thorn-shape waveform under a flat frontal impact.
3. The thorn-shape waveform is close to an isosceles triangle. The rising slope θ and the height of the thorn peak are related to the strain rate dependence.
4. The thorn-shape waveform and succeeding mountain-shape waveform are induced by the double-strike phenomenon.
5. Viscosity discontinuity before and after the thorn waveform is thought to be the cause of the impact force waveform in soft materials.

References

- [1] Zhao, H., Gary, G. and Klepaczko, J.P. (1997) On the Use of a Viscoelastic Split Hopkinson Pressure Bar, *International Journal of Impact Engineering*, 19, 319-330.
- [2] Song, B., Chen, W.W., Ge, Y. and Weerasooriya, T. (2007) Radial Inertia Effects in Kolsky Bar Testing of Extra-Soft Specimens, *Experimental Mechanics*, 67, 659-670.
- [3] Kwon, J. and Subhash, G. (2010) Compressive Strain Rate Sensitivity of Ballistic Gelatin, *Journal of Biomechanics*, 43, 420-425.

- [4] Fujimoto, Y., Shintaku, E., Tanaka, Y. and Fujiyoshi, J. (2012) Pad Type Compressive Force Sensor Suitable for High-Speed Impact Force Measurement, Transactions of the Japan Society of Mechanical Engineers, Series C, 78, 2438-2449. (in Japanese)
- [5] Fujimoto, Y., Liu, C., Uesugi, T., Tanaka, Y. and Shintaku, E. (2013) Pipe Surface Sensor for Impulsive Force Measurement, Transactions of the Japan Society of Mechanical Engineers, Series C, 79, 113-123. (in Japanese)
- [6] Fujimoto, Y., Liu, C., Tanaka, Y. and Shintaku, E. (2013) Measurement of Double-Strike Phenomenon of Impulsive Force Using Fluctuating Load Detection Plate, The Japanese Society for Experimental Mechanics, 13, 112-120. (in Japanese)
- [7] Liu, C., Tanaka, Y. and Fujimoto, Y. (2015) Viscosity Transient Phenomenon during Drop Impact Testing and Its Simple Dynamics Model, World Journal of Mechanics, 5, 33-41.
- [8] Hoffman, R.L. (1972) Discontinuous and Dilatant Viscosity Behavior in Concentrated Suspensions. I. Observation of a Flow Instability, Transactions of the Society of Rheology, 16, 155-173.
- [9] Bender, J. and Wagner, N.J. (1996) Reversible Shear Thickening in Monodisperse And Bidisperse Colloidal Dispersions, Journal of Rheology, 40, 889-915.
- [10] Richeton, J., Ahzi, S., Vecchio, K.S., Jiang, F.C. and Adharapurapu, R.R. (2006) Influence of Temperature and Strain Rate on the Mechanical Behavior of Three Amorphous Polymers: Characterization and Modeling of the Compressive Yield Stress, International Journal of Solids and Structures, 43, 2318-2335.
- [11] Lieberman, D.E., Venkadesan, M., Werbel, W.A., Daoud, A.I., D'Andrea, S., Davis, I.S., Mang'eni, R.O. and Pitsi-ladis, Y. (2010) Foot Strike Patterns and Collision Forces in Habitually Barefoot Versus Shod Runners, Nature, 463, 531-535.

Chapter 7 Viscosity Transient Phenomenon During Drop Impact Testing and Its Simple Dynamics Model

The author developed an impact force sensor that can accurately measure a high-speed impact force waveform and applied the sensor to impact tests of several soft materials. Experiments were carried out using compact drop test equipment under a flat frontal impact condition [1-3].

In a flat frontal impact, a free-falling drop hammer with a flat bottom surface strikes a plate-like soft material in the normal direction. Synchronized impact forces are measured using two sensors installed on both the drop hammer side and the floor side. The examined soft materials are a sponge plate, a sponge rubber plate, a gel plate, a silicon rubber plate, a nitrile rubber plate, tofu, konjac, tofu, an oil clay plate, a low-rebound urethane foam plate, a cork plate, sliced ham, pork ham steak, and pork. With the exception of the cork plate, all of these materials exhibited a thorn-shaped waveform and a subsequent mountain-shaped waveform.

In the impact testing of soft materials, a thorn-shaped waveform (spike-like feature) has appeared in previous experiments [4-6]. Song et al. concluded that this feature is a result of the radial inertia effect [4]. However, the authors believe that this unique waveform is a result of the double-strike phenomenon caused by the viscosity transient phenomenon [3]. When a soft material receives an impact force, a large viscous resistance is induced at the beginning of the impact. The viscous resistance then decreases rapidly with time. Furthermore, the authors demonstrated that the feature of the impact force waveform can be qualitatively simulated by a standard linear solid (SLS) model [2]. In

the SLS model, the damping coefficient of a dashpot was treated as time dependent.

In the present study, the influences of strain rate and impact area on the thorn-shaped waveforms are discussed based on the SLS model and the experimental results. Furthermore, it is shown that the thorn-shaped waveform can be observed in impact tests of relatively smooth areas of human skin and of the free-falling hollow balls.

7.1 Impact Force Waveform of Soft Materials under Flat Frontal Impact

Fig.7.1(a) shows a typical impact force waveform of soft material under a flat frontal impact. Fig.7.1(b) summarizes the feature of thorn-shaped waveforms obtained by the experimental observations. The impact force waveform of soft materials is the mixture of two types of waveforms. The first (thorn-shaped) waveform shows a large viscosity resistance (red isosceles triangle Q), and the second (mountain-shaped) waveform shows a small viscosity resistance (dashed black curve R). This resistance change occurs suddenly at the thorn peak. In other words, a viscosity transient is induced at the thorn peak. The soft material surface is struck twice by the relative movement of the colliding objects.

The thorn-shaped waveform has a steep slope on the rising segment (which is θ), which usually approximates a straight line. The θ and the thorn peak become large as the strain rate increase. The second part of the waveform has a gentler slope (which is α) and is mountain shaped. The slope α becomes gentler than the initial slope θ because a viscosity discontinuity is induced by the first strike.

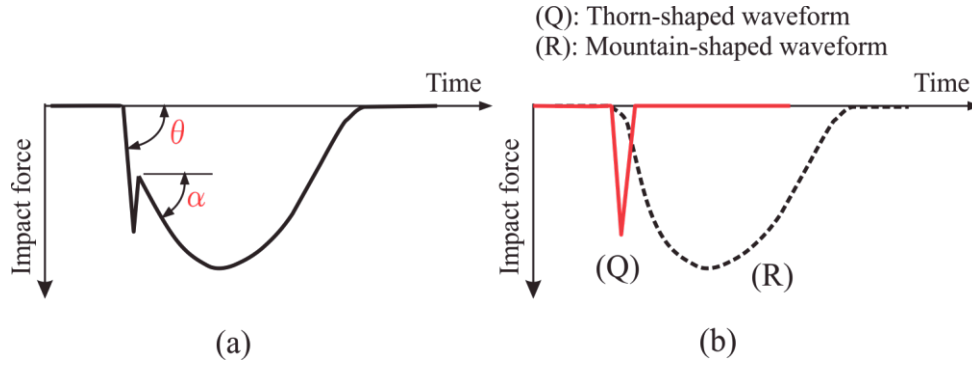


Fig. 7.1 (a) Typical impact force waveform of soft material under a flat frontal impact. (b) Two types of waveforms contained in the impact force waveform of soft material.

7.2 Simulation of Impact Force Waveform by the SLS Model

Fig.7.2 shows the condition under which the drop weight (mass: $m = 1.9 \text{ kg}$) collides with a plate-like soft material at speed V_0 . The thickness of the soft material is T . The soft material is modeled by the SLS model. The mass (drop weight) is not connected to the spring and dashpot. The SLS model adds an elastic spring k_1 to the Maxwell model (a viscous damper c and an elastic spring k_2) in parallel. The impact velocity V_0 is given to the mass as the initial condition. The differential equation of the SLS model is given as Eq (7.1), where x_2 is the displacement of the hammer position, and x_1 is the displacement of the dashpot. The initial strain rate is $\dot{\epsilon}_0 = V_0 / T \text{ (s}^{-1}\text{)}$. The Runge-Kutta method is used for solving the equation of motion. The time increment in the calculation is $5 \times 10^{-6} \text{ s}$.

$$\begin{cases} m\ddot{x}_2 + k_1x_2 + k_2(x_2 - x_1) = 0 \\ k_2(x_2 - x_1) = c\dot{x}_1 \end{cases} \quad (7.1)$$

The spring coefficients k_1 and k_2 are assumed to be constant throughout the collision. As mentioned above, we believe that the viscosity transient occurs during the early stage of the impact force. This influence is taken into consideration through the damping coefficient c of the dashpot, which is treated as a time-dependent value.

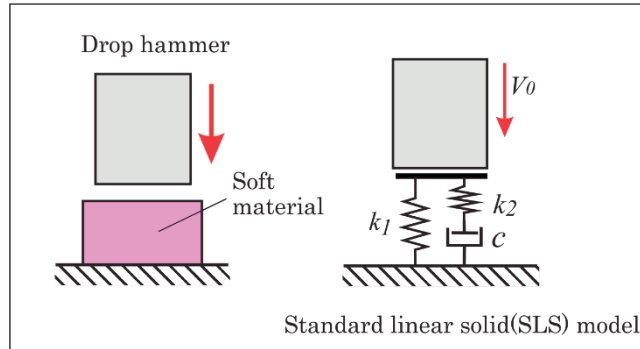


Fig. 7.2 SLS model for the simulation of impact force waveform of soft material.

7.3 Comparison of Experimental and Simulation Results

7.3.1 Influence of Impact Velocity on the Thorn-Shaped Waveform

Fig.7.3 compares the impact force waveforms of the upper sensor measured by compact drop test equipment. The soft material is a nitrile rubber (NBR) square plate with one side 100mm. The thickness is $T = 30$ mm (rubber hardness: 70). The drop height is $h = 100, 200,$ or 380 mm. The impact velocity is $V_0 = 1.4$ m/s when $h = 0.1$ m (strain rate: $\dot{\epsilon}_0 = V_0/T = 46$ s⁻¹), $V_0 = 1.98$ m/s when $h = 0.2$ m ($\dot{\epsilon}_0 = 66$ s⁻¹), and $V_0 = 2.73$ m/s when $h = 0.38$ m ($\dot{\epsilon}_0 = 91$ s⁻¹). A thorn shape is clearly observed in the rising segment of the waveform. In the experimental figure, when the drop height h becomes large, the slope θ of the rising segment becomes steeper and the height of the thorn peak becomes larger. The heights of thorn peak and mountain peak are roughly proportional with the impact velocity V_0 .

Fig.7.4 shows the impact force waveforms simulated by the SLS model for the three cases. Fig.7.5 shows the values of the assumed parameters in the SLS model. The spring coefficients are $k_1 = 1,000$ kN/m and $k_2 = 3,000$ kN/m. The damping coefficient c of the

dashpot is assumed to be a time-dependent value, which changes during the impact period. When $0 < t < 0.2$ ms, $c = 2,000$ kg/s. During the period $0.2 < t < 0.4$ ms, c decreases linearly from 2,000 kg/s to 300 kg/s. During the period $t > 0.4$ ms, $c = 300$ kg/s. The period $0.2 < t < 0.4$ ms is the period of the viscosity transient.

The simulation was conducted by varying k_1 , k_2 , and c in order to search for the condition in which the simulated waveform becomes close to the experimental waveform. In other words, k_1 , k_2 , and c are decided such that the thorn height, the subsequent mountain height, and the total impact period of the waveform match those of the experiments.

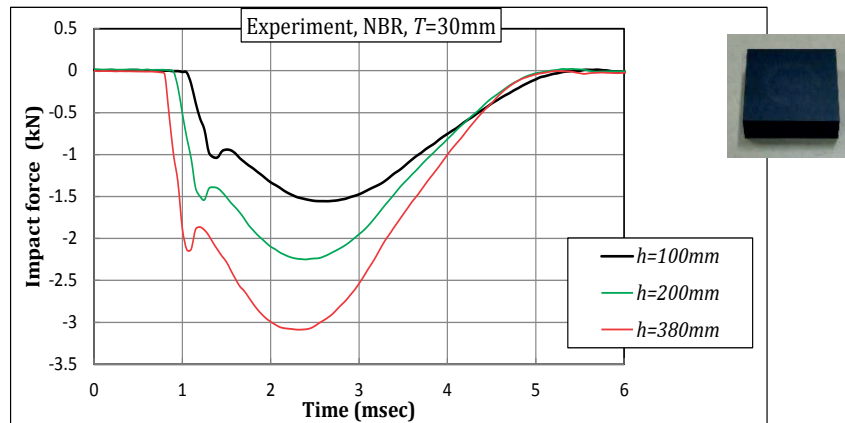


Fig. 7.3 Impact force induced by the weight drop onto NBR plate with $T = 30$ mm

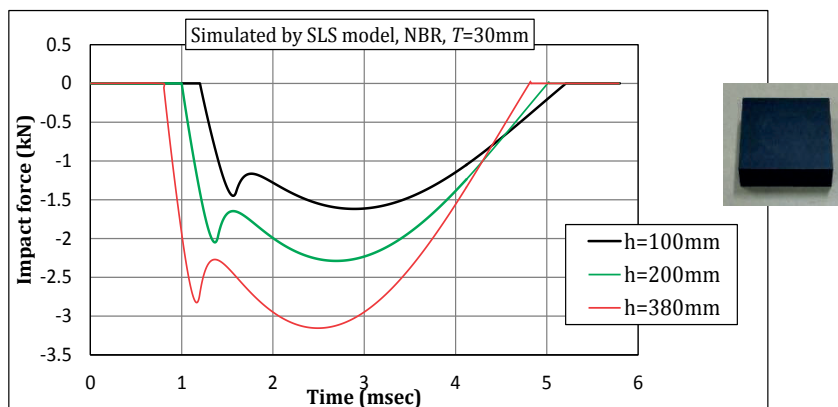


Fig. 7.4 Impact force waveform of NBR plate simulated by SLS model.

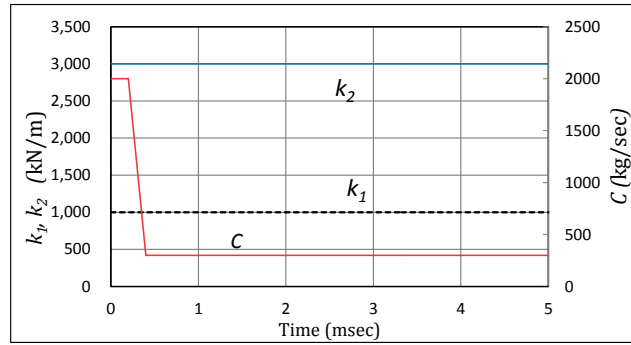


Fig. 7.5 Spring coefficients k_1 and k_2 and damping coefficient c assumed for the NBR plate with $T = 30$ mm.

A thorn-shaped waveform is clearly observed in the simulation. Note that, in the simulation, the slope θ of the thorn becomes steeper and the thorn height becomes larger according to the increase in the impact velocity V_0 (or strain rate $\dot{\epsilon}_0$). The total impact period is approximately the same as that of the experiments. The height of the thorn peak is roughly proportional to the impact velocity $V_0 (= h^{1/2})$ in both the experiments and the simulation. In other words, the shape of the thorn is related to the strain rate of the soft material.

In Fig.7.5, the impulse of the simulated waveform is larger than that of the experimental waveform. One reason for this difference is considered to be that the SLS model cannot exactly represent the coefficient of restitution of the drop hammer after the collision.

7.3.2 Influence of Impact Area on the Thorn-Shaped Waveform

Circular aluminum plates having a diameter of $D = 20, 30, 40,$ or 50 mm and a thickness of $d = 5$ to 8 mm was attached to the bottom of the drop hammer, as shown in Fig.7.6. The hammer was dropped from a height of $h = 380$ mm onto a 30 mm-thick NBR plate. The purpose of this experiment was to determine how the impact force waveform is influenced by the impact area. Since the circular plate is thick, the impact force acts

only on the circular plate and does not reach the bottom of the drop hammer.

Fig.7.7 shows the measured impact waveforms. Solid curves correspond to the upper sensor, and dashed curves correspond to the lower sensor. Since the diameter of the aluminum disk is small, the disk is buried deeply into the NBR. Therefore, according to the reduction of the impact area, the contact time of the waveform becomes long and the peak force becomes small. In addition, the thorn peak becomes lower as the impact area becomes smaller. This suggests that the thorn becomes unclear for the case in which the drop hammer has a spherical bottom surface.

Fig.7.8 shows the impact force waveforms simulated by the SLS model. The assumed k_1 , k_2 , and c are summarized in Table 7.1. The values of k_1 , k_2 , and c in Fig.7.6 are assumed for the case of $D = 60$ mm. Then, the values of k_1 , k_2 , and c are proportionally changed in accordance with the respective impact area.

In Fig.7.8, the thorn height decreases as the impact area becomes smaller. Moreover, the impact time increases as the impact area becomes smaller. In other words, the simulation results qualitatively represent the characteristics of the experimental results.

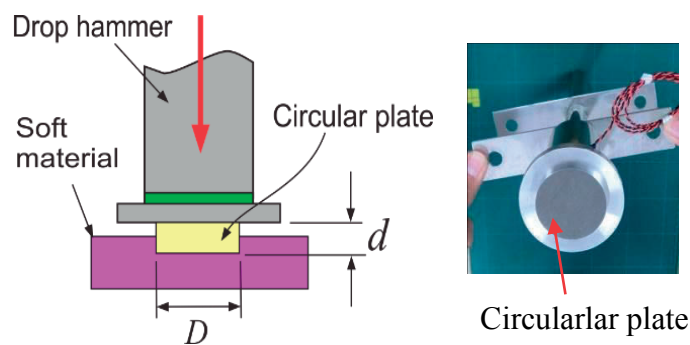


Fig. 7.6 Circular aluminum plate attached to the bottom of the drop weight.

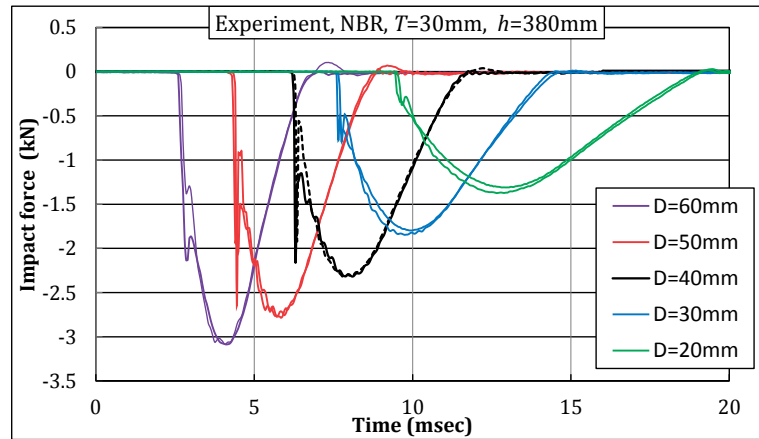


Fig. 7.7 Impact force induced by weight drop onto NBR plate with $T = 30$ mm.

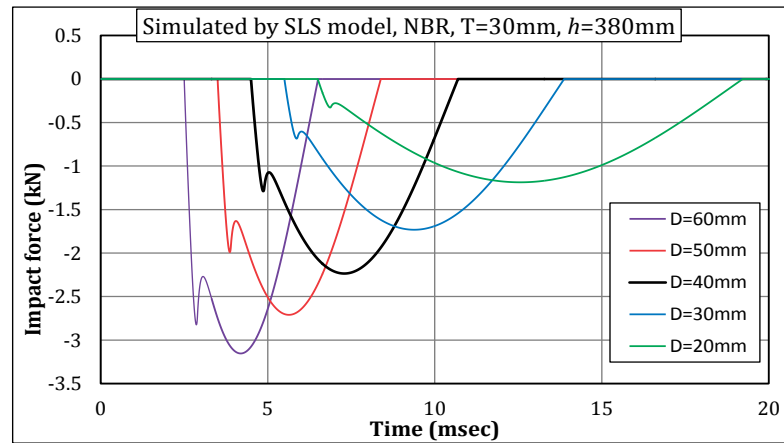


Fig. 7.8 Impact force waveforms of NBR plate simulated by SLS model.

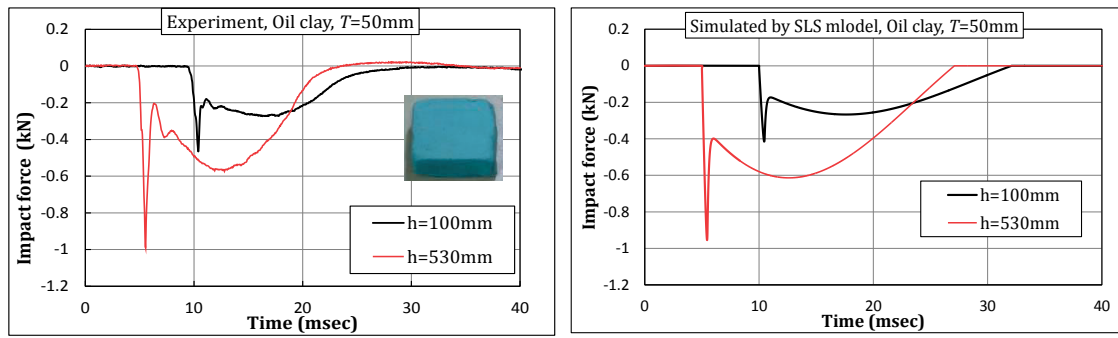
Table 7.1 Spring coefficients and damping coefficients of NBR assumed in the SLS model.

Diameter of AL plate D (mm)	Impact area A (mm ²)	Spring coefficient		Damping coefficient c (kg/sec)		
		k_1 (kN/m)	k_2 (kN/m)	$0 < t < 0.2$ msec	$0.2 < t < 0.4$ msec	$t > 0.4$ msec
60	2827	1000	3000	2000	Linearly decrease	300
50	1963	694	2083	1389	Linearly decrease	208
40	1257	444	1333	889	Linearly decrease	133
30	707	250	750	378	Linearly decrease	75
20	315	111	333	222	Linearly decrease	33

7.3.3 Case of An Oil Clay Plate under A Flat Frontal Impact

Fig.7.9(a) shows the impact force waveform (as measured by the upper sensor) of an oil clay plate with 100mm square. Its thickness is about $T = 50$ mm. The drop heights are $h = 100$ and 530 mm. A large thorn is observed. As the drop height increases (V_0 becomes higher), the slope θ becomes steeper and thorn peak becomes higher. The thorns are more obvious than those for other materials. As shown in the enlarged view, the shape of the thorn is similar to an isosceles triangle.

Fig.7.9(b) shows the waveforms simulated by the SLS model. Here, k_1 is assumed to be equal to 40 kN/m, and k_2 is assumed to be equal to 800 kN/m. The damping coefficient c of the dashpot is assumed to be a time-dependent value, which changes during the impact period.



(a)

(b)

Fig. 7.9 Impact force waveforms of oil clay plate measured experimentally and simulated by SLS model.

Table 7.2 shows the spring and damping coefficients of the oil clay. During the period of $0 < t < 0.2$ ms, $c = 1,500$ kg/s. During the period of $0.2 < t < 0.5$ ms, c decreases linearly from $1,500$ kg/s to 100 kg/s. During the period of $t > 0.5$ ms, $c = 100$ kg/s. The period $0.2 < t < 0.5$ ms is the period during which the viscosity transient occurs. The spring coefficients are $k_1 = 30$ kN/m and $k_2 = 800$ kN/m.

Table 7.2 Spring coefficients and damping coefficient of oil clay plate assumed in the SLS model.

	Spring coefficient		Damping coefficient c (kg/sec)		
	k_1 (kN/m)	k_2 (kN/m)	$0 < t < 0.2 \text{ msec}$	$0.2 < t < 0.5 \text{ msec}$	$t > 0.5 \text{ msec}$
Oil clay ($T=50\text{mm}$)	30	800	1500	Linearly decrease	100

7.4 Discussion

Fig.7.10 shows the two types of collision condition under a flat frontal impact. Condition 1 is the case that the soft material surface is larger than the area of drop hammer bottom. Condition 2 is the case that the soft material surface is smaller than the area of drop hammer bottom. All the previous our experiments were carried out under the Condition 1. In the Condition 1, the surrounding soft material near the edge of the drop weight bottom is momentarily deformed by the impact. This edge effect may be the cause of the thorn.

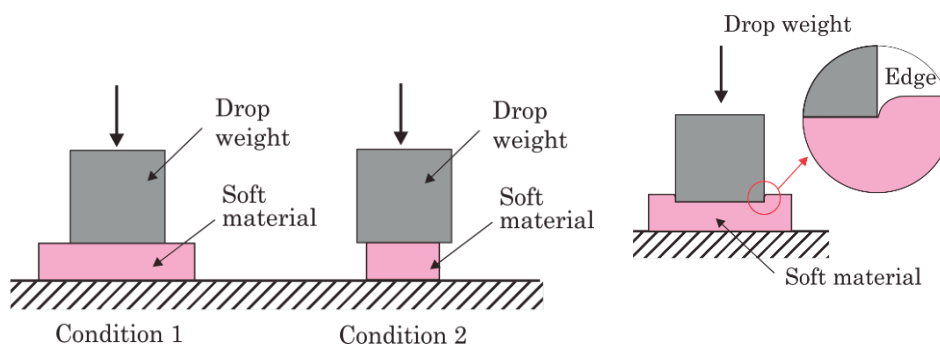


Fig. 7.10 Two types of collision conditions and edge effect seen in Condition 1

So, we conducted the experiment under the Condition 2. An NBR circle plate with

50mm diameter which is smaller than the area of drop hammer bottom is used for the experiment. The thickness of NBR is $T = 30$ mm and the drop height is $h = 100, 200,$ or 380 mm.

Fig.7.11 shows the impact force waveforms of the upper sensor measured by the compact drop test equipment. As is seen in the figure, a thorn-shaped waveform became smaller than that of Fig.7.3. However, the thorns are still observed in the rising segment of the waveform.

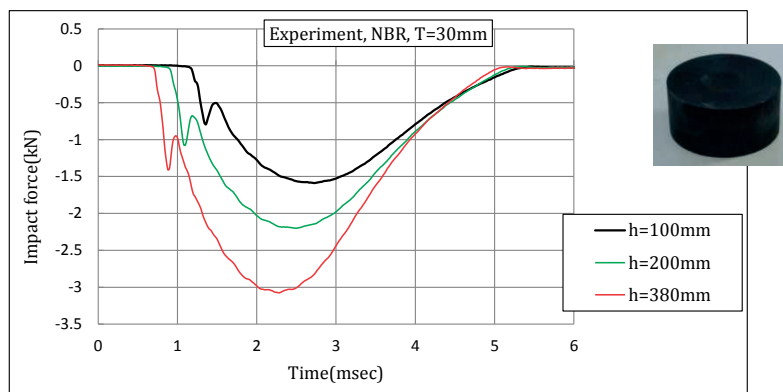


Fig. 7.11 Impact force induced by the weight drop onto NBR plate with $T = 30$ mm

Another experiment of Condition 2 was carried out using an oil clay circle plate with 50mm diameter. The thickness of oil clay is $T = 50$ mm and the drop height was $h = 100$ or 530 mm. Fig.7.12 shows the impact force waveforms. Although the height of the thorn became smaller, thorn-shaped waveform still occurred.

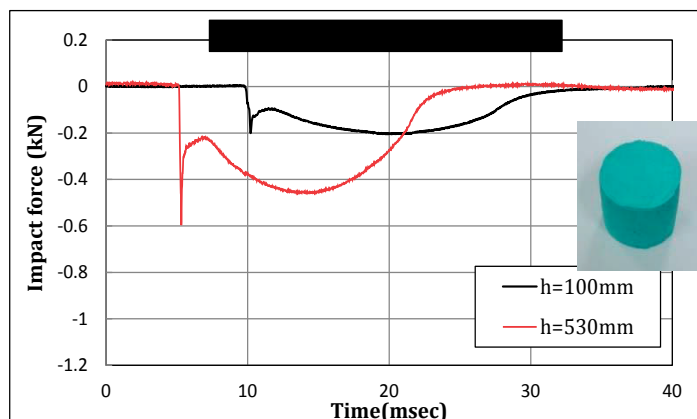


Fig. 7.12 Impact force induced by the weight drop onto oil clay plate with $T = 50$ mm

Why does this small thorn occur? The author thought that it may be a friction effect between the drop weight bottom and the soft material surface. Usually, soft material deforms into a barrel shape by the frictional forces induced in the upper and lower surface of the soft material. So, we conducted an experiment with paint machine oil to the upper and lower surfaces of NBR circle plate. However, the thorn-shaped waveform which did not change so much was appeared for all the cases.

7.5 Impact Force of Human Skin under a Flat Frontal Impact

The drop hammer was removed from the compact drop test equipment, and the hammer was held by hand, as shown in Fig.7.13. Then, the relatively smooth areas of forearm skin, calf skin, and thigh skin were struck by the hand-held hammer. Considering the above mentioned results, a thorn-shaped waveform should be observed on flat skin areas without bone directly underneath. Impact force waveforms with steep slopes θ in the rising segment and small thorns were observed in most cases.

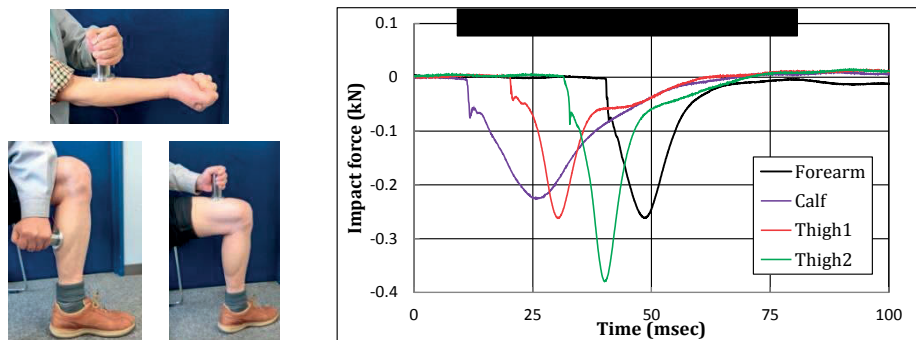


Fig. 7.13 Human skin was struck by a hand-held hammer. The measured impact force waveforms are shown on the right.

7.6 Impact Force of Free-Falling Hollow Balls

Fig.7.14 shows the impact force waveform of a superball (solid ball) with an excellent rebound property, as measured through free-fall drop tests from heights of 1.0 m and 2.0 m. No thorn appears in the waveform. Similarly, the impact forces of a hardball (used for baseball), a softball, a golf ball, and a bowling ball (solid balls) did not generate thorn-shaped waveforms due to the spherical surfaces of the balls.

Fig.7.15 shows the waveforms of a handball, a rubber ball, and a tennis ball (hollow balls) obtained through free-fall drop tests. Even though they have spherical surfaces, the hollow balls generate a steep slope θ and a small thorn. This is thought to be the reason that the contact area of a hollow ball is flattened at the moment of impact, and a condition similar to a flat frontal impact is achieved.

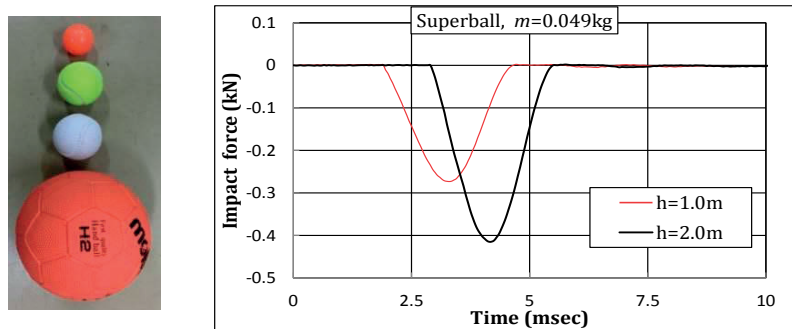


Fig. 7.14 Impact force induced by free-falling superball (solid ball).

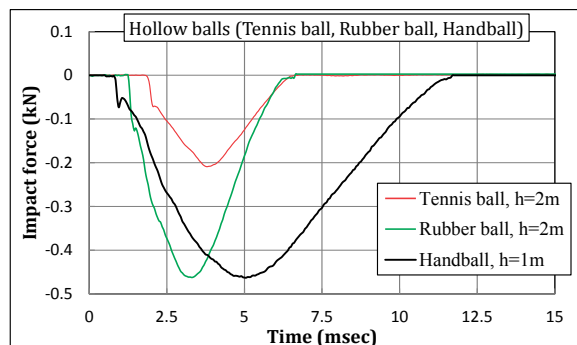


Fig. 7.15 Impact force induced by free-falling hollow balls.

7.7 Conclusions

The impact force waveforms of soft materials were examined based on a drop impact experiment and a dynamics model. Experiments were carried out using compact drop test equipment under the condition of a flat frontal impact. The standard linear solid model (SLS model), in which viscosity transient is considered, is used for the simulation of the impact force waveform. The results obtained here are as follows:

1. The impact force waveforms of soft material consist of a thorn-shaped waveform and a subsequent mountain-shaped waveform. The thorn-shaped waveform is influenced by the strain rate. The rising slope θ of the thorn becomes steeper as the strain rate increases. The height of the thorn peak becomes higher as the strain rate increases.

2. The SLS model can qualitatively simulate the characteristics of thorn-shaped waveforms.

3. Under the condition of a flat frontal impact, the thorn appears clearly according with the increase in the impact area. If either the surface of the drop hammer or the surface of the soft material is curved, the thorn-shaped waveform becomes unclear. These conditions can be reproduced in the simulation using the SLS model.

4. From the experimental observations, the authors think that viscosity transient is induced at the thorn peak. At the moment of impact, a large viscous resistance is induced near the surface of soft material, and the viscous resistance is rapidly reduced after generation of the thorn. However, the physical reason of the viscosity transient phenomenon is unclear.

References

- [1] Fujimoto, Y., Liu, C., Tanaka, Y. and Shintaku, E. (2013) Measurement of Double-Strike Phenomenon of Impulsive Force Using Fluctuating Load Detection Plate, The Japanese Society for Experimental Mechanics, 13, 112-120. (in Japanese)
- [2] Liu, C., Tanaka, Y. and Fujimoto, Y. (2015) Viscosity Transient Phenomenon during Drop Impact Testing and Its Simple Dynamics Model, World Journal of Mechanics, 5, 33-41.
- [3] Fujimoto, Y., Liu, C., Tanaka, Y., Shintaku, E. and Nakanishi, T. (2015) Thorn-shape Waveform and Double-Strike Phenomenon Seen in the Impact Force of Soft Material, World Journal of Mechanics, 5, 59-69.
- [4] Song, B., Ge, Y., Chen, W.W. and Weerasooriya, T. (2007) Radial Inertia Effects in Kolsky Bar Testing of Extra-Soft Specimens, Experimental Mechanics, 67, 659-670.
- [5] Kwon, J. and Subhash, G. (2010) Compressive Strain Rate Sensitivity of Ballistic Gelatin, Journal of Biomechanics, 43, 420-425.
- [6] Chen, W., Lu, F. and Winfree, N. (2002) High-strain-rate Compressive Behavior of a Rigid Polyurethane Foam with Various Densities, Experimental Mechanics, 42, 65-73.

Chapter 8 Conclusions and Future Scopes

8.1 Conclusions

In this dissertation, we describe the design and evaluation of several piezoelectric sensor using PVDF film as the sensing element. In general, the main purposes of the design are to find more flexible sensor and to be used in wide range of application and understanding the mechanical response of objects under impact loading conditions.

In this chapter 3, three kinds of prototype sensors which are sheet-type impact force sensor, pad sensor and fluctuating load detection plate are developed. Sheet-type sensor has a structure in which silicone rubber sheets are pasted on both surfaces of the piezoelectric film. The pad sensor features light-weighting and high-rigidity in thickness direction, therefore, it is verified that the thin pad sensor can be used to measure the greater extent high-speed impact compared to the conventional load cell. Since the fluctuating load detection plate possesses the metal plates, it can only be used in the plane, but it still can accept impact from hard object. The accuracy of these sensors are demonstrated based on the measurements of the waveform impulse and the momentum theory.

In the metal ball falling tests, through observing the waveform that the metal ball collides the load detection plate, the response performance of the load detection plate against the impact force has been verified.

In the drop test of longitudinally turning bar, steel shaft is a fall from a predetermined

inclination angle, it was measured double-strike phenomenon that occurs in a very short period of time when the tip portion hits the resin round bar. And after the collision the shaft tip immediately bounced, bending vibration of the shaft is superimposed, so it is able to measure the waveform of double-strike phenomenon that shaft momentarily hit the resin round bar twice.

In chapter 4, the study is carried out experimental studies on the pipe surface-mounted sensor for impact force measurement. The aim is to select a pipe whose dimensions is close to baseball bat and to measure the impact force when hit and bunt the baseball. The detection element is a piezoelectric film, and a thin detachable pad sensor which is able to installed onto the pipe and don't require any processing is developed and is able to carry out the experiment, the performance and problems of sensor are revealed. The results obtained are as follows.

1. A proposed configuration of a thin pipe sensor that can be installed on the pipe surface with about load-bearing capacity of 10kN has been submitted.

2. The impact force waveforms which are obtained when hard ball, soft ball and rubber is dropped from 2m height on pipe sensor have been measured, the momentum change (Momentum) before and after collision and waveform impulse (Impulse) have been confirmed nearly match.

3. The impact force waveform when hard ball thrown by pitcher is hit or bunt has been measured by installing the pipe sensor on the metal bat.

4. In the method of fixing the sensor and the cover plate to the pipe using an aluminum adhesive tape, Variation of about $\pm 10\%$ occurs in the slope of output the sensor by fastening method. It is needed to improve the method of fixing the sensor in the future.

In chapter 5, this section is aimed to develop a flexible sensor which can be used in

the measurement of impact force in flexible interface. The boxing punching is chosen as the measurement object.

1. A flexible sensor in which sixteen sensor elements are arranged in a 4×4 matrix is developed. Each sensor element is a rigid plate structure. The sensor elements are arranged at regular intervals. Both entire surfaces of the sensor elements are covered with artificial leather, and its surrounding and the vertical and horizontal columns are finished by sewing. Flexibility of the sensor is achieved by the flexible leather connections between adjacent sensor elements;

2. Sum of the output signal of each sensor element is collected through the conductive cloth. Since there is no electrical wiring inside the sensor, the sensor structure is hard to break by the impact force which is realized;

3. Boxing punching experiments were carried out by installing the sensor on concrete wall and sandbag. The flexible sensor showed a good performance in the experiments;

4. The proposed sensor is inadequate distribution number of sensor elements, but the proposed sensor includes mechanisms to achieve a flexible sensor with high accuracy. By increasing the distribution density of the sensor element, it can approach to the practical sensor.

In chapter 6, using compact drop test equipment, this study experimentally observed the impact force waveforms for several kinds of soft materials.

1. Thorn-shape waveform of soft material appears clearly under the condition of a flat frontal impact. If either surface of the drop hammer or the soft material is curved, the thorn-shape waveform becomes un-clear.

2. Most of the soft materials (except cork sheet) such as sponge, sponge rubber, nitrile rubber, oil clay, paper clay, low-rebound urethane foam, ham, pork, and konjac showed

a thorn-shape waveform under a flat frontal impact.

3. The thorn-shape waveform is close to an isosceles triangle. The rising slope θ and the height of the thorn peak are related to the strain rate dependence.

4. The thorn-shape waveform and succeeding mountain-shape waveform are induced by the double-strike phenomenon.

5. Viscosity discontinuity before and after the thorn waveform is thought to be the cause of the impact force waveform in soft materials.

In chapter 7, the impact force waveforms of soft materials were examined based on a drop impact experiment and a dynamics model. Experiments were carried out using compact drop test equipment under the condition of a flat frontal impact. The standard linear solid model (SLS model), in which viscosity transient is considered, is used for the simulation of the impact force waveform.

1. The impact force waveforms of soft material consist of a thorn-shaped waveform and a subsequent mountain-shaped waveform. The thorn-shaped waveform is influenced by the strain rate. The rising slope θ of the thorn becomes steeper as the strain rate increases. The height of the thorn peak becomes higher as the strain rate increases.

2. The SLS model can qualitatively simulate the characteristics of thorn-shaped waveforms.

3. Under the condition of a flat frontal impact, the thorn appears clearly according with the increase in the impact area. If either the surface of the drop hammer or the surface of the soft material is curved, the thorn-shaped waveform becomes unclear. These conditions can be reproduced in the simulation using the SLS model.

4. From the experimental observations, the authors think that viscosity transient is

induced at the thorn peak. At the moment of impact, a large viscous resistance is induced near the surface of soft material, and the viscous resistance is rapidly reduced after generation of the thorn. However, the physical reason of the viscosity transient phenomenon is unclear.

8.2 Future scopes

In the scope of sensor design, especially in measuring the dynamics loads using the composition of PVDF film, a wide range of applications and new designs are still need pay more attentions. Flexibility, thinness, lightness, toughness and accuracy are the keys of flexible impact force sensor. Overcoming of these problems is essential for the realization of the sensor that can be installed on human body or robot. In relation with the design result described in this dissertation, some new sensor designs are still can be developed with some considerations as follows:

1. In the case of matrix arrangement sensor, at this stage it has not been achieved that each sensor element can be wired in a separate line so that the impulsive force in an area can be analyzed through obtain the signals of every regional distribution. The wiring way and the receiving mode that could read multiple sources simultaneously need to be developed in the following study.

2. A more sophisticated dynamics model is necessary in order to describe the details of the impact force waveform of the respective soft material. The densification mechanism of the material, the double-strike phenomenon, etc., should be considered in the model for the quantitative simulation.

ACKNOWLEDGMENTS

I would like to express my sincerest appreciation to my research and academic supervisor Prof. Yukio Fujimoto, for his invaluable guidance, encouragement, patience and continuous support through my study in Hiroshima University. He has taught me how to become a researcher from a student. I hope there is on day I could become a researcher as good as him. I am grateful to Associate Prof. Eiji Shintaku for his guidance and help with my research. I want to thank Assistant Prof. Yoshikazu Tanaka for his help and care with my study.

I would like to give my special thanks to Dr. Huang Fei for his help with my application and continuous care and support with my study and life. I would like to thank my student tutors Mr. Xiaoguang Ning and Mr. Daisuke Ishimoto for their selfless care and help in the days when I just got Japan, and their continuous support and friendship during my days in Hiroshima University. Also I want to thank all students in the System Safety Laboratory for their support in my experimental work and invaluable friendships.

I would like to present my heartfelt appreciation to my parents for their continuous support. With their care, I had never felt I was away from home and I know I'm always loved.

I very much acknowledge the help of the staffs in the offices of the department of engineering systems and the graduate school of engineering.

Finally, I would like to give my appreciation to all my friends. I'm such a lucky man to have you in my life.